

ALMA MATER STUDIORUM · UNIVERSITÀ DI BOLOGNA

---

Scuola di Scienze  
Corso di Laurea Magistrale in Fisica

**TOMOGRAPHIC 3D RECONSTRUCTION  
THROUGH LINEAR INVERSION FOR BREAST  
MICROWAVE IMAGING**

**Relatore:**  
**Prof. NICO LANCONELLI**

**Presentata da:**  
**LORENZO MUSCA**

**Correlatori:**  
**PhD. MASSIMILIANO GRANDI**  
**PhD. SIMONE MASETTI**

**Sessione III**  
**Anno Accademico 2014/2015**

*«L'immagine originaria di una buona opera d'arte non è una figura reale, viva, quantunque questa possa esserne l'occasione determinante. L'immagine originaria non è carne e sangue, è spirituale. E' immagine che ha la sua dimora nell'anima dell'artista. Anche in me, Narciso, vivono di queste immagini, che spero di rappresentare e di mostrarti un giorno.»*

Herman Hesse – Narciso e Boccadoro

# Sommario

Nella tesi presente affrontiamo il problema dell'individuazione e localizzazione di un target sferico, omogeneo, sufficientemente piccolo e con proprietà elettriche caratteristiche, posto all'interno di un volume di forma cilindrica; questo modello viene utilizzato per rappresentare, in modo semplificato, il seno femminile contenente un tumore solido.

Utilizziamo la tecnica del Microwave Imaging (MWI) per ispezionare il dominio di indagine, ovvero otteniamo informazioni sulla posizione dell'oggetto interno tramite irradiazione del fantoccio del seno con onde elettromagnetiche nell'intervallo di frequenze delle microonde: la formazione dell'immagine viene quindi effettuata dopo aver risolto numericamente il problema dello scattering inverso del campo elettromagnetico, facendoci ottenere l'informazione desiderata.

Ad oggi, il MWI è l'unica tecnica potenzialmente in grado di fornire la distribuzione delle proprietà dielettriche del tessuto indagato ed è in generale un metodo non-invasivo per il soggetto. Tuttavia, a causa degli alti costi computazionali richiesti per effettuare la risoluzione numerica del problema di scattering inverso, la ricerca attuale è fortemente orientata verso lo sviluppo di tecniche tomografiche bidimensionali, in quanto hanno dei requisiti computazionali molto più bassi rispetto alla controparte 3D. Uno degli scopi principali di questo progetto è di estendere propriamente l'attuale algoritmo di inversione lineare dalla ricostruzione planare a quella volumica; i risultati che vengono ottenuti, nelle stesse condizioni e per lo stesso setup sperimentale, vengono riportati per entrambi i diversi approcci.

Il confronto preliminare e l'analisi delle performance degli algoritmi di ricostruzione viene eseguito attraverso simulazioni numeriche effettuate in un ambiente software: un antenna dipolare viene utilizzata per illuminare il modello virtuale del seno da diverse posizioni e, per ciascuna di esse, il rispettivo valore del campo elettrico scatterato viene registrato. Questo particolare tipo di setup è meglio conosciuto come configurazione monostatica. I dati ottenuti vengono quindi utilizzati per poter ricostruire il dominio di indagine, insieme alla posizione dello scatteratore, sotto forma di immagine chiamata pseudospettro. Durante questo processo il tumore viene modellizzato con una sfera dielettrica di piccolo raggio e, ai fini dello scattering elettromagnetico, viene trattato come una sorgente puntiforme.

Per ottenere un miglioramento delle performance delle ricostruzioni, la fase di acquisizione viene effettuata per un certo numero di frequenze diverse: i diversi pseudospettri sono ricostruiti a partire da dati ottenuti a singola frequenza e vengono quindi combinati in modo incoerente tramite l'algoritmo Multiple Signal Classification (MUSIC). Utilizziamo un approccio multi-frequenza per testare le performance dell'algoritmo di inversione lineare 3D mentre variamo la posizione della sorgente all'interno del fantoccio e per diverse posizioni del piano dell'antenna. I risultati delle analisi a partire dalle immagini ricostruite vengono quindi riportati.

Infine, eseguiamo la ricostruzione tridimensionale a partire da dati acquisiti sperimentali-

mente con il sistema di acquisizione presente al laboratorio di imaging a microonde del DIFA, dell'Università di Bologna, per un prototipo di fantoccio del seno recentemente realizzato; gli pseudospettri e le analisi delle performance dei metodi di ricostruzione per il modello reale sono riportati.



# Abstract

In the present thesis we address the problem of detecting and localizing a homogeneous, sufficiently small spherical target with characteristic electrical properties inside a volume of cylindrical shape; this representation is employed to model, in its simplest form, a female breast containing a solid tumor.

We make use of Microwave Imaging (MWI) technique to inspect the investigation domain, that is, we collect information on the position of the buried scatterer by irradiating the breast phantom with electromagnetic waves in the microwave frequency range: image formation is then achieved after numerically solving the inverse scattering problem for electromagnetic field, giving us the desired information.

At the present time, MWI is the only technique able to potentially provide the distribution of dielectric permittivity for the inspected tissue and it is generally a non-invasive method for the subject. Nevertheless, due to the high computational costs involved in the numerical solution of the inverse scattering problem, current research in the MWI field is mainly oriented towards the development of bidimensional tomographic techniques, which require much less computational effort than their 3D counterpart. One of the main works of this project is to properly extend the existing linear inversion algorithm from planar slice to volume reconstruction; results obtained, under the same conditions and experimental setup, are reported for the two different approaches.

Preliminary comparison and performance analysis of the reconstruction algorithms is performed via numerical simulations in a software-created environment: a dipole antenna is used for illuminating the virtual breast phantom from different positions and, for each position, the corresponding scattered field value is registered. This particular setup is best known as monostatic configuration. Collected data are then exploited in order to reconstruct the investigation domain, along with the scatterer position, in the form of image called pseudospectrum. During this process the tumor is modeled as a dielectric sphere of small radius and, for electromagnetic scattering purposes, it's treated as a point-like source.

To improve the performance of reconstruction technique, we repeat the acquisition phase for a number of frequencies in a given range: the different pseudospectra, reconstructed from single frequency data, are incoherently combined with Multiple Signal Classification (MUSIC) method which returns an overall enhanced image.

We exploit multi-frequency approach to test the performance of 3D linear inversion reconstruction algorithm while varying the source position inside the phantom and the height of antenna plane. Analysis results and reconstructed images are then reported.

Finally, we perform 3D reconstruction from experimental data gathered with the acquisition system in the microwave laboratory at DIFA, University of Bologna for a recently developed breast-phantom prototype; obtained pseudospectrum and performance analysis for the real model are reported.

# Contents

<b>1</b>	<b>Motivation in Breast Cancer Screening</b>	<b>1</b>
1.1	General Overview of Breast Screening Techniques . . . . .	2
1.1.1	Mammography . . . . .	5
1.1.2	Breast MRI . . . . .	8
1.1.3	Breast Ultrasound . . . . .	9
1.2	Introduction to Microwave Imaging . . . . .	11
1.2.1	Breast Tissues Electrical Properties . . . . .	12
1.2.2	Dielectric Spectrum and Tissue Models . . . . .	15
<b>2</b>	<b>Reconstruction Algorithm</b>	<b>19</b>
2.1	Electromagnetic Scattering Problem . . . . .	19
2.2	Scattering as an Inverse Problem . . . . .	21
2.2.1	Non-Linear Methods . . . . .	22
2.2.2	Linear Methods . . . . .	23
2.3	TR-MUSIC . . . . .	26
2.3.1	TR Formulation in Multistatic Antenna Configuration . . . . .	26
2.3.2	Multiple Signal Classification . . . . .	28
2.3.3	TR-MUSIC in Monostatic Antenna Configuration . . . . .	29
2.3.4	Background Green's Functions . . . . .	31
2.3.5	Multi-Frequency Imaging . . . . .	32
2.4	Reconstruction Supplementary Processes . . . . .	33
2.4.1	Signal Filtering and Clutter Cancellation . . . . .	34
2.4.2	Preliminary Assesment of Domain Properties . . . . .	35
2.5	Numerical Assessment and Evaluation of Reconstruction Results . . . . .	39
2.5.1	Spatial Metrics . . . . .	39
2.5.2	Contrast Metrics . . . . .	42
2.5.3	Uncertainty of Estimated Values . . . . .	43
<b>3</b>	<b>Image Reconstruction and Source Detection</b>	<b>44</b>
3.1	Synthetic Data Collection . . . . .	45
3.1.1	Finite-Element-Method . . . . .	45

3.1.2	Virtual Breast Phantom System . . . . .	46
3.2	Multi-Elevation Reconstruction . . . . .	50
3.2.1	Mono-Elevation Reconstruction . . . . .	50
3.2.2	Multi-Elevation MUSIC Algorithm Evaluation . . . . .	54
3.2.3	3D Scatterer Detection in Heterogeneous Media . . . . .	69
<b>4</b>	<b>Experimental Measurements</b>	<b>76</b>
4.1	Experimental Setup . . . . .	77
4.1.1	Breast Phantom Prototype . . . . .	77
4.1.2	Dipole Antenna Transceiver . . . . .	79
4.1.3	Vector Network Analyzer . . . . .	79
4.2	Operational Conditions . . . . .	82
4.2.1	Frequency Selection Working Interface . . . . .	83
4.3	Homogeneous Breast Phantom Reconstruction . . . . .	85
4.4	Heterogeneous Breast Phantom Reconstruction . . . . .	90
4.4.1	Insert in the External Position . . . . .	91
4.4.2	Insert in the Internal Position . . . . .	95
<b>5</b>	<b>Conclusions</b>	<b>99</b>

# List of Abbreviations

ACR	American College of Radiology
AD	Absolute Displacement
AR	Average Resolution
CMI	Confocal Microwave Imaging
CT	Computed Tomography
DAS	Delay And Sum
DMAS	Delay Multiply And Sum
DBIM	Distorted Born Iterative Method
DFG	Dyadic Green's Function
DORT	Decomposition of the Time-Reversal Operator
EFIE	Electric Field Integral Equations
FEM	Finite Element Method
FF	Far-Field
FFDM	Full Field Digital Mammography
FT	Fourier Transform
FTDT	Finite Difference Time Domain
FWHM	Full Width at Half Maximum
GA	Genetic Algorithm

IDAS	Improved Delay And Sum
I-MUSIC	Interferometric MUSIC
IF	Intermediate-Field
MIST	Microwave Imaging via Space-Time
MOM	Method of Moments
MRI	Magnetic Resonance Imaging
MUSIC	MUltiple Signal Classification
MT	Microwave Tomography
MWI	Microwave Imaging
NF	Near-Field
PCA	Principal Component Analysis
PET	Positron Emission Tomography
PSF	Point Spread Function
ROI	Region Of Interest
RLS	Recursive Least Squares
SA	Simulated Annealing
SAR	Specific Absorption Rate
SCR	Signal to Clutter Ratio
SMR	Signal to Clutter Mean Ratio
SVD	Singular Value Decomposition

US	UltraSonography
UWB	Ultra WideBand
VNA	Vector Network Analyzer
WB-MUSIC	Wide-Band MUSIC

# Chapter 1

## Motivation in Breast Cancer Screening

At the present time, breast cancer is the tumor with highest incidence factor for female population [1]. Its impact is of the order of the hundreds of thousands of deaths in the world each year (Fig.2): populations of all countries are involved, independently from the modernization and welfare standards.

While the exact causes are not known, there exist a group of established risk factors[2], mainly of genetic and environmental type, for which some women may be more predisposed than others in being affected by the disease; leading a healthy lifestyle is very important as it helps in first place to reduce the risk factors associated to breast cancer and other illnesses[3].

On the prevention side, still, the most important aspect is to be able to detect a developing tumor while it's in the early stage of growth: early breast cancers are usually easier to treat, may need less treatment and are more likely to be cured. Women who are diagnosed with breast cancer at the earliest possible stage and receive prompt treatment have a 90% chance of surviving for at least 5 years (Fig.1) after diagnosis [4].

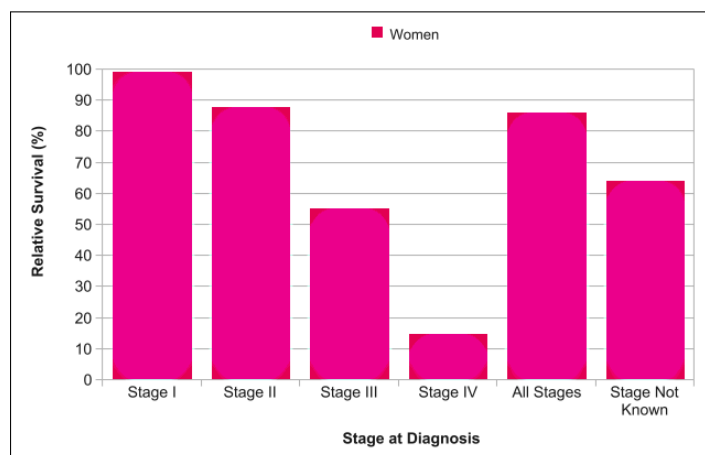


Fig.1: *Breast Cancer (C50), Five-Year Relative Survival by Stage.*

We can see the benefits of a regular breast screening plan as it augments the chance of early tumor detection, thus improving the treatment efficiency and reducing the mortality rate by a significant amount. When high quality mammographic screening is offered at regular intervals to 40- to 74- year-old women, over 50% of the invasive cancers will be detected in the size range of 1–14 mm, fewer than 20% will be axillary node positive, and only about 20% will be poorly differentiated[5].

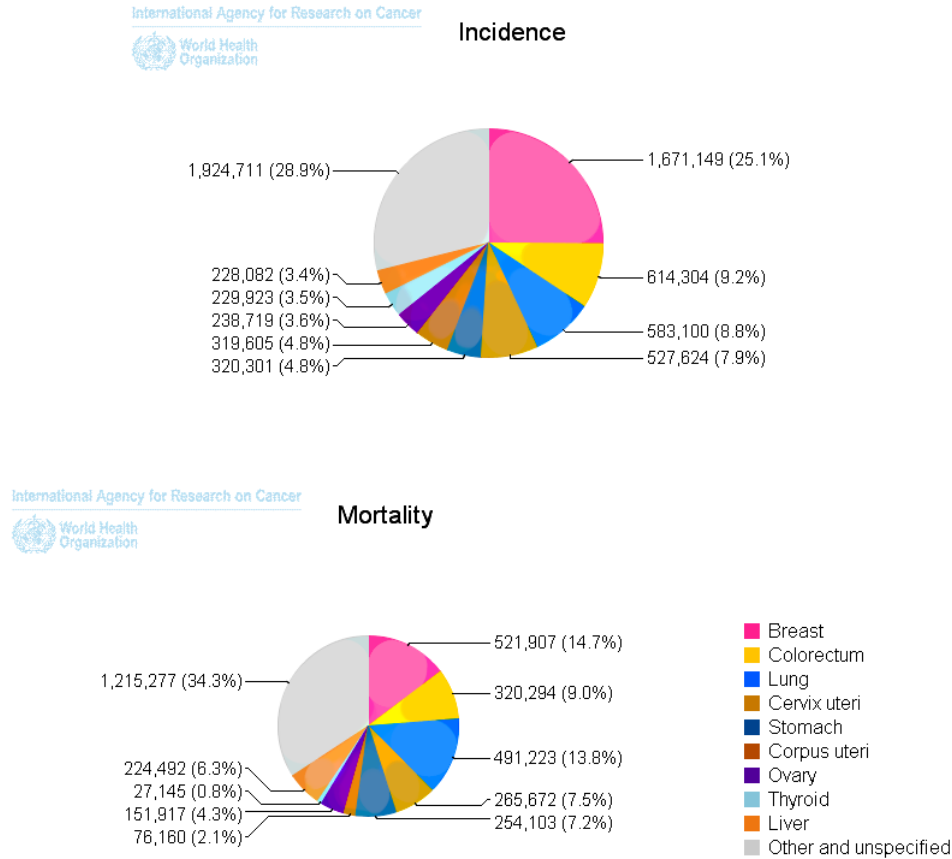


Fig.2: *Estimated Age-Standardised cancer incidence and mortality Rate (ASR) for women*<sup>1</sup>.

## 1.1 General Overview of Breast Screening Techniques

Breast cancer screening is defined as “the evaluation of a population of asymptomatic women, who have no overt signs or symptoms of breast cancer, in an effort to detect

<sup>1</sup>[http://globocan.iarc.fr/Pages/fact\\_sheets\\_population.aspx](http://globocan.iarc.fr/Pages/fact_sheets_population.aspx)



unsuspected disease earlier in its growth”[7].

Currently, the golden standard in screening methods is the X-ray digital mammography[8], which uses low-dose X-rays to return an image (mammogram) of the investigated breast to further check the presence of a tumor. Other kind of tests include the clinical breast exam, where a doctor or nurse uses his or her hands to feel for lumps or other changes in the breasts and underarms, and the breast self-exam, equivalent to the clinical test but performed by the patient directly on herself. These tests can complement but not entirely substitute mammography screening, since they do not suffice in detecting an early stage cancer and thus reduce breast cancer mortality[9]. On the other hand, mammography has its own limitations, starting from a significant rate of failure in cancer detection (false negatives), ranging from 4/100 to 34/100 [11]; mammogram exploits ionizing radiation which is, in general, harmful<sup>2</sup> and can even increase the chance for a disease to occur[10]; X-ray imaging methods require the breast to be compressed<sup>3</sup>, which is uncomfortable and often painful for the patient. These well-recognized limitations led to an increased interest in the research and development of new imaging techniques.

One alternative to mammography is given by MRI, whose high sensitivity is contrasted by high operational costs and low specificity, reason why it is used only for exceptional, high risk cases and not in standard screening protocols[32]. Ultrasound imaging technique has also been used, showing a false negative rate of 17/100[14]. Positron Emission Mammography has shown higher detectability than PET/CT and comparable or better sensitivity than MRI, which makes it a viable choice where MRI cannot be used[19].

Combining the different imaging modes with the classical clinical tests has been investigated and, depending on the used combination methods, variable sensitivity and specificity can be reached, still without enhancing the overall accuracy<sup>4</sup> and net patient safety[14]; it has been shown that supplemental screening with US for women with dense breasts has a high false-positive rate and substantially increases the number of unnecessary biopsies, with little to no gain in quality-adjusted life years[15]; several factors are known to reduce patient acceptance of breast MR imaging, including claustrophobia and the requirement for intravenous contrast material[16].

A class of emerging techniques, the Microwave Tomography, is funded on the purpose of electromagnetic waves in the microwave frequency range, and it exploits the electric contrast naturally present between the lesion and healthy tissue for image formation. Microwave breast imaging is particularly attractive, both from a patient and technical point of view, being it a non-ionizing radiation which also avoids breast compression procedure, is capable of small tumors detection, has fast image acquisition times, potentially presents both high sensitivity (detects most tumors in the breast) and specificity (detects only cancerous tissue) and is far less expensive when compared to MRI

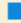

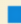
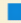

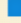
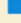

---

<sup>2</sup>There is no threshold of radiation dose under which the absence of any cancer risk is proven.

<sup>3</sup>This ensures enhanced imaging quality and a lower absorbed dose for the patient[12].

<sup>4</sup>So far, no single imaging method has both high sensitivity and high specificity for breast cancer[6].

equipment and nuclear medicine installations[17]; microwave imaging (MWI) is not expected to pose a health risk for patient<sup>5</sup>. Other novel screening techniques employing electromagnetic waves in different frequency range exist (Fig.3) and include, among others, electric impedance tomography, diffuse optical tomography, microwave radiometry, biopotential[18] and biomagnetic imaging.

Technology	Description	FDA approved*	Used routinely	Used infrequently	Clinical data suggests a role	Pre-clinical suggests a role	Data not available yet
Film-screen mammography	The standard X-ray technique.		Screening & diagnosis				
Full-field digital mammography	Digital version of X-ray technique.			Screening & diagnosis			
Ultrasound	Forms images by reflection of megahertz frequency sound waves.		Diagnosis		Screening		
Magnetic resonance imaging (MRI)	Forms images using radio emissions from nuclear spins.			Diagnosis	Screening		
Scintimammography	Senses tumors from gamma-ray emission of radioactive pharmaceuticals.				Diagnosis	Screening	
Thermography	Seeks tumors by infrared signature.				Diagnosis	Screening	
Electrical impedance imaging	Maps the breast's impedance with low-voltage signal.				Diagnosis	Screening	
Optical imaging	Localizes tumors by measuring scattered near-infrared light.				Diagnosis	Screening	
Electrical potential measurement	Identifies tumors by measuring potentials at array of detectors on skin.				Diagnosis	Screening	
Positron emission tomography	Forms images using emission from annihilation of positrons from radioactive pharmaceuticals.					Screening & diagnosis	
Novel ultrasound techniques	Include compound imaging, which improves resolution using sound waves from several angles; 3-D and Doppler imaging.					Screening & diagnosis	
Elastography	Uses ultrasound or MRI to infer the mechanical properties of tissue.					Screening & diagnosis	
Magnetic resonance spectroscopy	Analyzes tissue's chemical makeup using radio emissions from nuclear spins.					Screening & diagnosis	
Thermoacoustic computed tomography	Generates short sound pulses within breast using RF energy and constructs a 3-D image from them.						Screening & diagnosis
Microwave imaging	Views breast using scattered microwaves.						Screening & diagnosis
Hall-effect imaging	Picks up sonic vibrations of charged particles exposed to a magnetic field.						Screening & diagnosis
Magneto-mammography	Senses magnetic contrast agents collected in tumors.						Screening & diagnosis

\*Approved for primary or adjunctive use in breast imaging.

Source: U.S. Institute of Medicine

Fig.3: *Technologies for breast cancer screening.*

<sup>5</sup>Microwave breast cancer detection systems are estimated to operate with power levels at least one order of magnitude below those of cellular telephones, thus satisfying the maximum SAR over human body safety standard[17].

### 1.1.1 Mammography

Digital mammography, also called full-field digital mammography (FFDM), is the standard breast-imaging technique that exploits low-energy X-rays (usually around 30 keV), with a dose of about 0.7 mSv, and is used both as a diagnostic and screening tool (Fig.4). In this process, the observed contrast in the resulting image is provided by different absorption rate of tissues, although more recent approaches are based on the phase shifting effect, for the phase contrast has proven to return a substantially enhanced image contrast over the absorption contrast[20].

The use of mammography as a screening tool for the detection of early breast cancer in otherwise healthy women without symptoms is controversial[21]: Keen and Keen indicated that repeated mammography starting at age 50 saves about 1.8 lives over 15 years for every 1000 women screened[22], but this result has to be compared against the presence of errors in diagnosis, overtreatment and radiation exposure<sup>6</sup>; other authors[24] have concluded that it is not clear whether screening does more good than harm<sup>7</sup>.

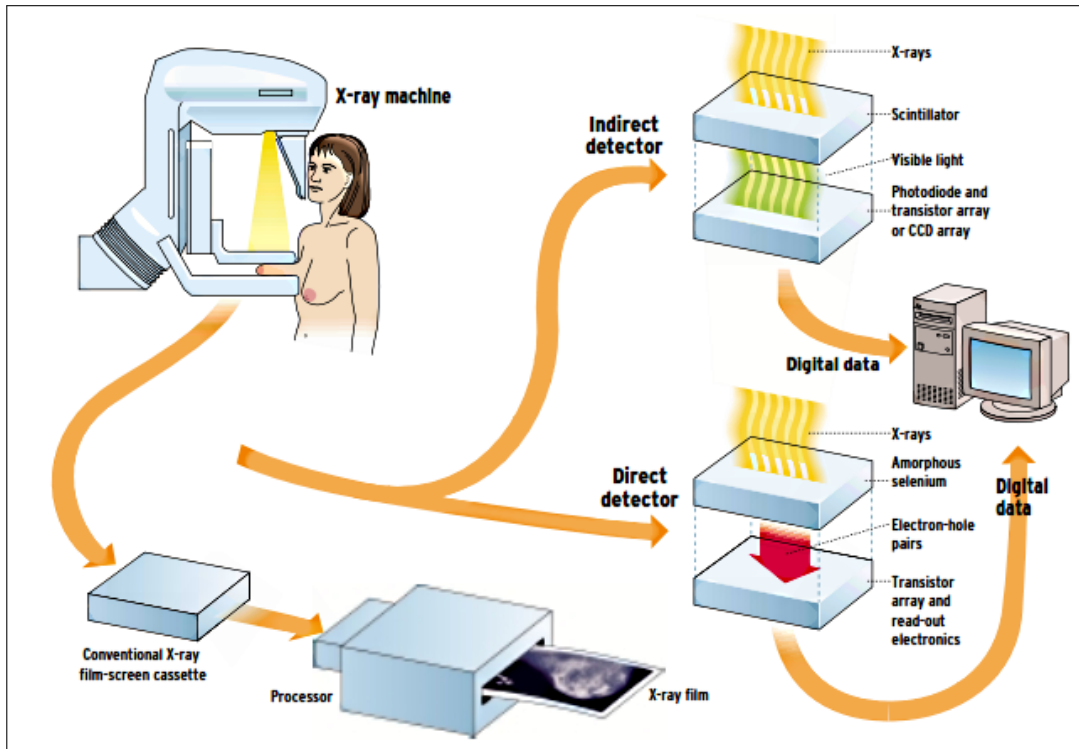


Fig.4: *Mammogram acquisition scheme.*

<sup>6</sup>The same authors also calculated that the absolute death risk from breast cancer, without screening, is about 1% over 15 years.

<sup>7</sup>“For every 2000 women invited for screening throughout 10 years, one will have her life prolonged and 10 healthy women [...] will be treated unnecessarily. Furthermore, more than 200 women will experience important psychological distress for many months because of false positive findings.”

The Canadian Task Force on Preventive Health Care (2012) and the European Cancer Observatory (2011) widely recommend mammography every 2–3 years to women between 50 and 69 in an attempt to reduce mortality (Fig.5) due to breast cancer[23]. Still, it's important to note that many women who have a breast cancer detected by mammography before the appearance of a lump do not, in practice, gain any real benefit from the mammogram: only between 3% and 13% of tumors detected by screening mammography are estimated to fall into the category of breast cancers whose treatment outcome is augmented by early detection[25], thus saving the patient life. The other categories, accounting for 87% to 97% of total mammogram detections, include in fact breast tumors that can be easily treated at later detection, aggressive cancers which are not curable despite earliest stage detection and the group of slow-growing or receding ones whose detection will actually result in overdiagnosis and overtreatment.

The best quality evidence does not demonstrate a reduction in mortality generally or a reduction in mortality from all types of cancer from screening mammography[24].

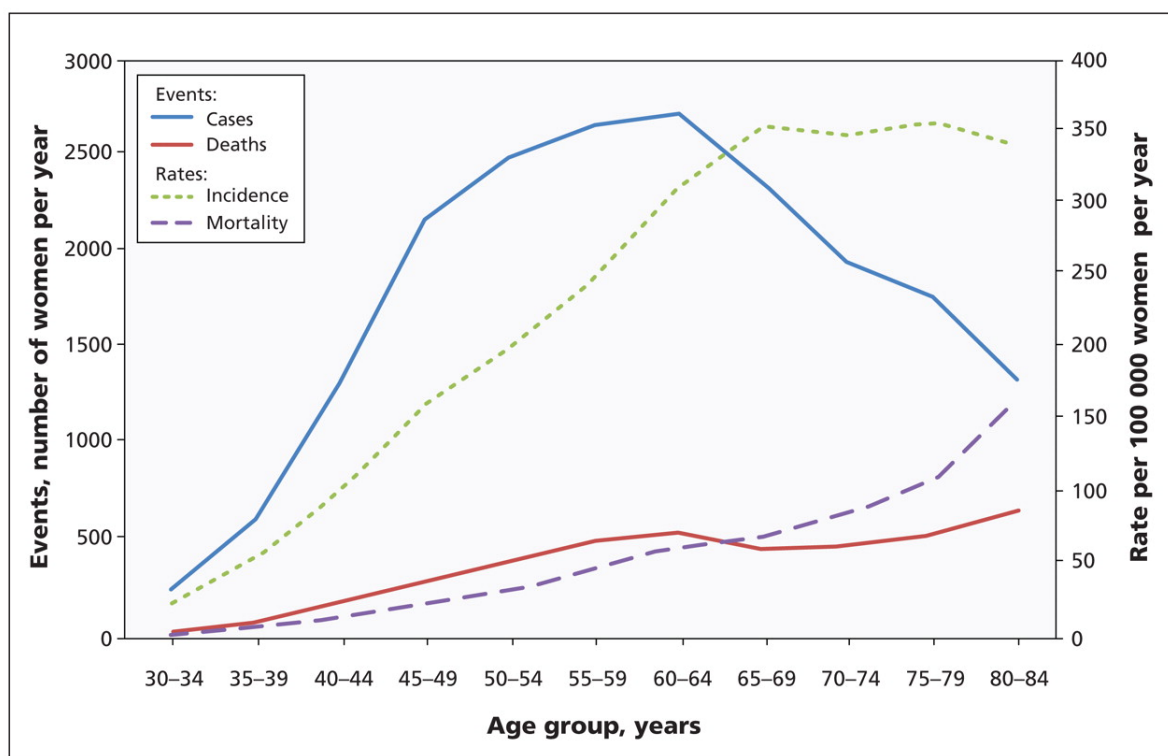


Fig.5: *Incidence of breast cancer and associated mortality among Canadian women in 2007.*

By examining a large population in an attempt to find the small number most likely to have a serious condition, sufficient sensitivity is demanded in order to detect a useful proportion of cancers, after which a more invasive testing is usually started. Still, the cost

of higher sensitivity is directly translated into a major number of patients that would be tagged as suspicious while not actually carrying the disease (Fig.6): new techniques are needed in order to eliminate the existing tradeoff between false positives ratio and high sensitivity[26](true positive rate), since false-positive mammograms lead to more expensive, unneeded follow-up screening programs which affect the patient, both physically and emotionally.

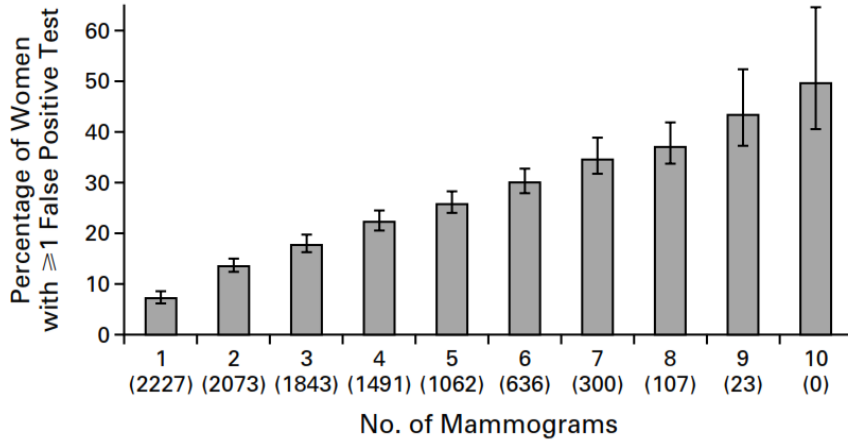


Fig.6: *A woman's estimated risk of having at least one false positive screening mammogram, according to the total number of screening mammograms performed<sup>8</sup>.*

The main tradeoff between harms and benefits for mammography is due to overdiagnosis process, defined by mammographic screenings detecting cancers that would not have come to clinical attention in the woman's lifetime if not for the screening itself; studies show that for every breast cancer death prevented by mammography, about three overdiagnosed cases will be identified and treated[28]. The excess mortality that arises from investigation and treatment of breast cancer remains minimal and, generally, outweighed by the overall benefits of mammography[28] but it exists and still needs to be reduced. The major risk of screening, along with the always present radiation exposure, is given by the rate of missed tumors, called false negatives ratio, and it's the reason why research in higher sensitivity techniques is so active. Mammography is around 10% less sensitive in women under 50 than in women aged 50-59, due to breast tissues being more dense in younger women[27].

At the present day it's difficult to obtain an accurate estimate of the false negative rate because its analysis does rely on the performing of mastectomy which, obviously, cannot be done on every patient subject to screening; current estimates depend on close follow-up of a large number of patients for many years, which is rarely achievable in practice

<sup>8</sup>The numbers in parentheses indicate the number of women with at least that many mammograms; error bars indicate 95% confidence intervals.

because many women do not actually return for regular mammography. Recent work has also been done on auto-detection for false negative mammograms, in an attempt to avoid the invasive surgical biopsy when the predicted risk of malignancy is low[29]. For women at increased risk of breast cancer, other imaging technologies are available and may contribute to the earlier detection of breast cancer. These treatments are particularly addressed to women under the age of 40 years since mammography is less sensitive in this case.

### 1.1.2 Breast MRI

MRI is a noninvasive medical test which exploits magnetic fields to produce detailed cross-sectional images of tissue structures and provides very good soft-tissue contrast. The contrast between breast tissues mainly depends on the mobility and magnetic environment of the hydrogen atoms in water and fat, contributing to the measured signal, which determines the brightness of tissues in the image.

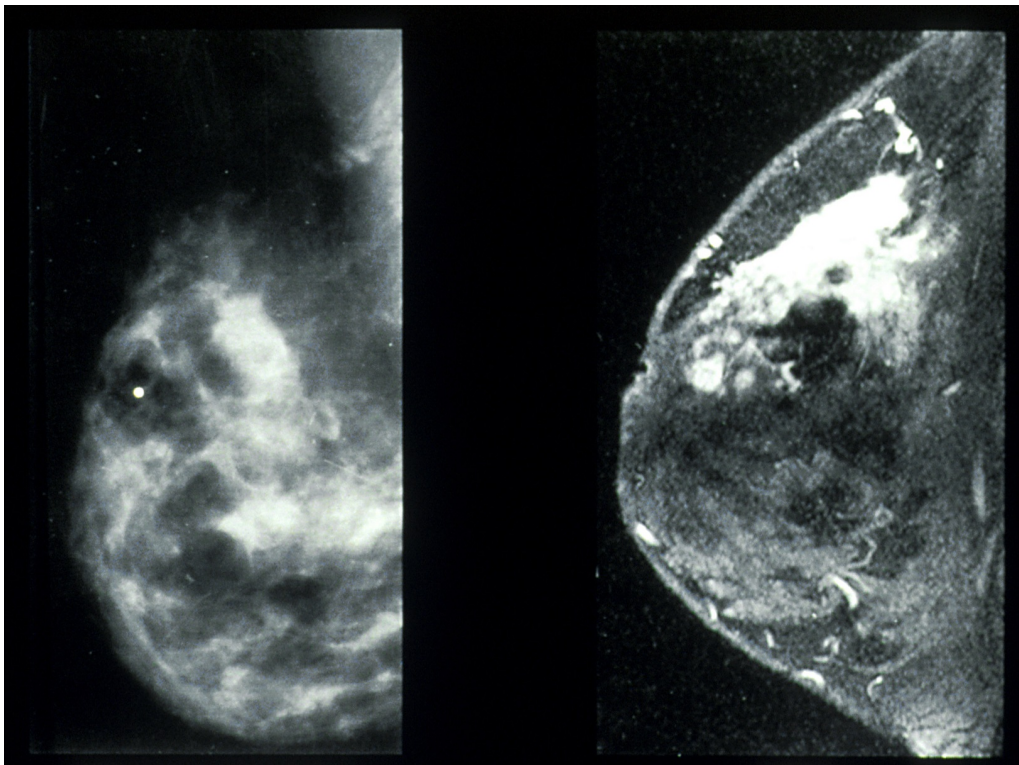


Fig.7: *Mammography (left) and MRI (right). MRI enhanced image was used to confirm diagnosis of a palpable cancer. The corresponding abnormality has been indicated with a white dot in the left mammogram, which failed in the detection<sup>9</sup>.*

---

<sup>9</sup>Mitchell D. Schnall, M.D., Ph.D. University Of Pennsylvania; image created in February, 1994.

The resulting MRI images for breast show predominantly parenchyma, fat and lesions – if any. To enhance contrast and provide reliable detection of breast tumor, a paramagnetic gadolinium-based contrast agent is injected intravenously; higher quality can be further achieved by employing breast-dedicated MRI coils in the apparatus.

Contrast-Enhanced MRI has been shown to have high sensitivity for detecting breast cancer in high-risk asymptomatic and symptomatic women, although reports of specificity have been more variable[30].

The high signal from enhancing lesions can be difficult to separate from fat signal: image subtraction and fat suppression methods are generally used to assess disease.

Breast MRI have recently been shown to provide good sensitivity as an imaging tool for breast cancer in women at increased risk based on family history[31].

Several studies have demonstrated the ability of MRI to detect cancer with early-stage tumors that are associated with better outcomes and, although survival or mortality data are not available, MRI has higher sensitivity and finds smaller tumors, compared with standard mammography: by reasonably extrapolating that detection of noninvasive and small invasive cancers will contribute to reduced mortality, it follows that MRI currently plays an important role in the breast screening scenario[32].

### 1.1.3 Breast Ultrasound

Ultrasound imaging or sonography is a noninvasive technique which is based on the transmission of high-frequency ( $f > 15$  kHz) mechanical waves throughout a particular part of the body: waves undergo different interactions (reflection, attenuation, Doppler effect) with the tissues matter, from which it's possible to retrieve information on the physical properties of the investigated object.

In this kind of imaging, sound waves are generated through an US transducer, which is placed upon the skin for the interested area, previously lubricated with a specific ultrasound gel, and the same transducer is used to acquire echo-signal originated from the waves reflected at acoustic interfaces, constituting the separation region between different tissues. The received echoes are then registered by a computer and used to form the US digital image, displayable on a monitor in real-time.

Ultrasound has become a valuable tool to use along with mammography because it is widely available and less expensive than other options, such as MRI. Usually, breast ultrasound is used as adjunct method to target a specific area of concern previously found on the mammogram, while the use of US imaging *instead of* mammograms for breast cancer screening is not recommended due to an unacceptable false positive and false negative outcomes: at present there is little evidence to support the use of breast ultrasound in routine primary population breast cancer screening[33]. On the other hand, ultrasound helps distinguish between cysts and solid masses and sometimes can help in telling the difference between benign and cancerous tumors; it can also be used to look for enlarged lymph nodes under the arm.

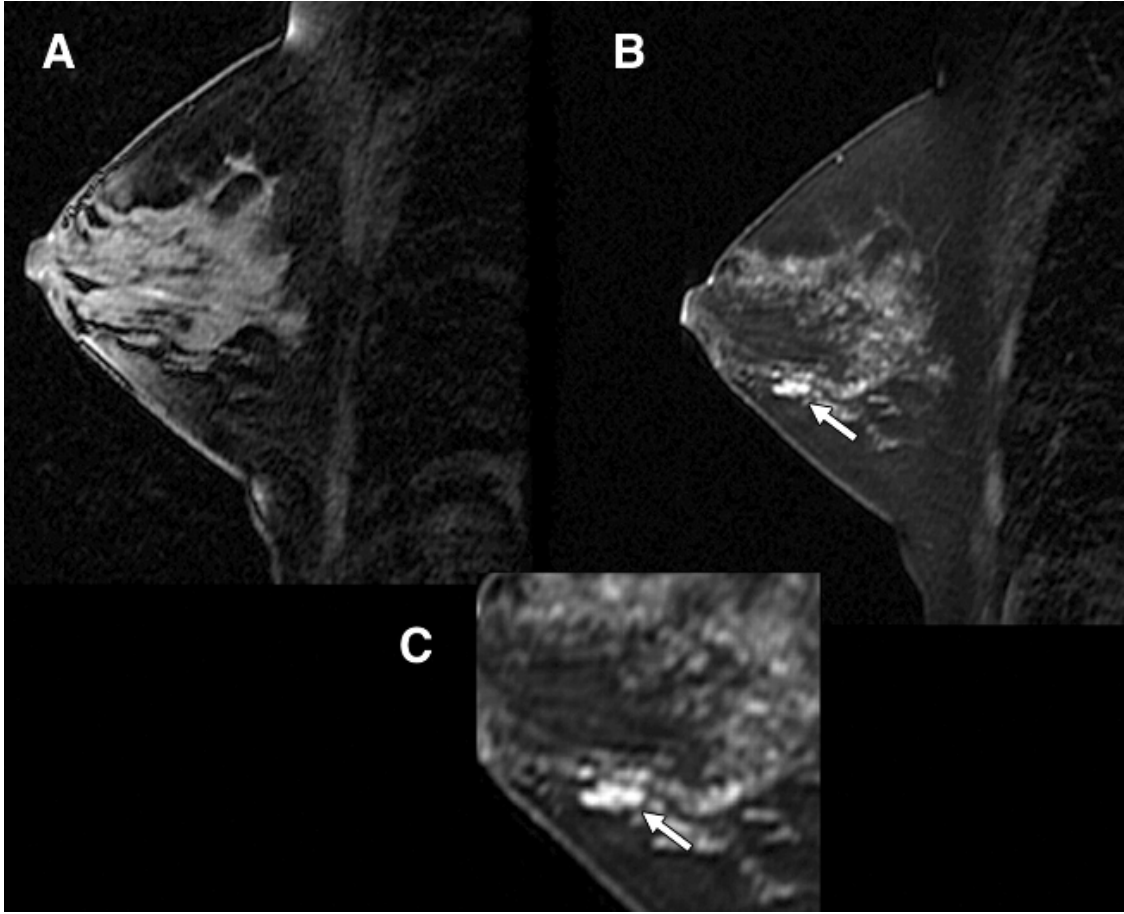


Fig.8: *Negative screening mammogram (A) and US (B) of 46-year-old woman: pathologic report proved infiltrating ductal carcinoma (C, white arrow)*<sup>10</sup>.

The overall cancer detection rate of US is comparable with X-ray mammography, recognizing a greater proportion of invasive and node-negative cancers, but, as a major drawback, the technique presents a bigger false positives rate[34].

---

<sup>10</sup>Cancer Yield of Mammography, MR, and US in High-Risk Women: Prospective Multi-Institution Breast Cancer Screening Study (RSNA, 2007).



## 1.2 Introduction to Microwave Imaging

Microwave Imaging is a method which aims at detecting a tumor by exploiting the difference in electrical properties between healthy tissue and disease. In the microwave frequency range (300 MHz – 30 GHz), the electromagnetic fields interactions with biological tissue depend on the conductivity  $\sigma$ , permittivity  $\varepsilon$  and permeability  $\mu$  of the object: when an incident microwave travelling across a homogeneous medium encounters an inhomogeneity, characterized by a change in the constitutive electromagnetic parameters of the material, the incident wave will scatter (Fig.10).

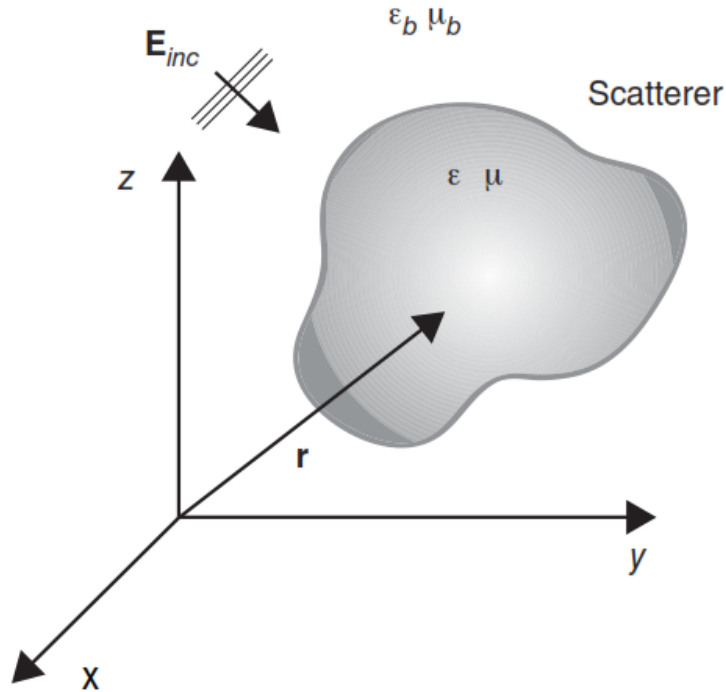


Fig.9: *Electromagnetic scattering by 3D source.*

In the picture above, the incident field passes from a *background medium*, characterized by constants  $(\varepsilon_b, \mu_b)$ , to the access volume of the *scatterer* (also called *source*), with parameters  $(\varepsilon, \mu)$ , where both materials have been considered as dielectrics or having a finite conductivity.

By illuminating the imaging domain with a transceiver antenna at a given frequency, two situations arise (Fig.10): in the absence of scatterers, the incident field transmits over the investigated domain and may be recorded by an array of receiving antennas, while in presence of a source both transmitted and reflected field can be registered by

antennas, including the same transmitter that generated the incident wave. In presence of an object, what can be physically measured is the *perturbed* or *total field*<sup>11</sup>,

$$\mathbf{E}_T(\mathbf{r}) = \mathbf{E}_I(\mathbf{r}) + \mathbf{E}_S(\mathbf{r}) ,$$

which is given by the sum of the *unperturbed* or *incident field*  $\mathbf{E}_I$ , defined as the field in the absence of the source, and the *scattered field*  $\mathbf{E}_S$ , determined by the interaction of the field  $\mathbf{E}_I$  with the scatterer[81].

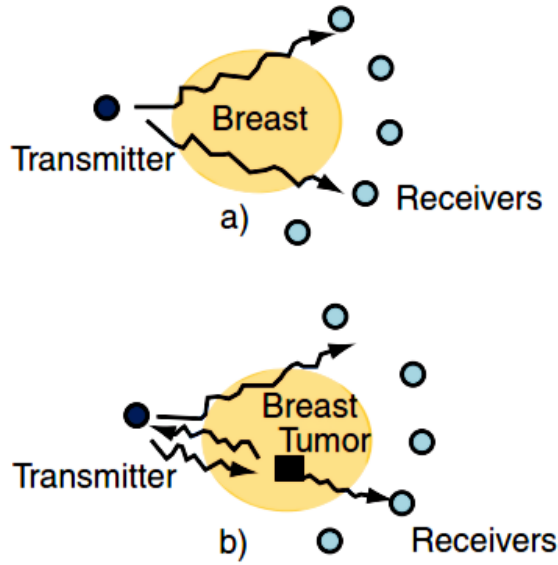


Fig.10: *Basic microwave imaging problem in absence (a) and presence (b) of a scatterer.*

The MWI methods are mainly divided into two categories: the tomographic approaches, which are based on the use of a multistatic antenna configuration to retrieve information on both field transmission and reflection, and the radar ones, which exploit a single transceiver to collect reflection data from different positions respect to the imaging domain[17].

### 1.2.1 Breast Tissues Electrical Properties

The interactions of an electromagnetic field with a material depend from the dielectric properties of the object itself, which can be defined by the complex relative permittivity

$$\varepsilon_r = \varepsilon' - j\varepsilon'' \quad (j = \sqrt{-1}) ,$$

---

<sup>11</sup>An equivalent relation occurs for the magnetic field:  $\mathbf{H}_T(\mathbf{r}) = \mathbf{H}_I(\mathbf{r}) + \mathbf{H}_S(\mathbf{r})$  .

consisting of a real part, the dielectric constant  $\varepsilon'$ , and an imaginary part, the out-of-phase loss factor  $\varepsilon''$ . The real part of  $\varepsilon_r$  determines the amount of electric field energy stored by the material due to polarization effects, while the loss factor expresses how much of that energy is actually dissipated as heat transfer due to displacement currents. The permittivity, characterizing the dielectric polarization response under the effect of an externally applied electric field, is generally a complex function of the incident field frequency. This dependance means that there is a frequency-dependant lag between changes in polarization and changes in the electric field: for this reason, a dielectric material is also referred as dispersive.

The dispersive behaviour can be shown by writing explicitly the displacement current term

$$\varepsilon''(\omega) = \frac{\sigma}{2\pi\nu\varepsilon_0} = \frac{\sigma}{\omega\varepsilon_0} ,$$

where  $\varepsilon_0$  is permittivity of free-space and  $\nu$  is the field frequency, and the relative permittivity takes the form

$$\varepsilon_r(\omega) = \varepsilon'(\omega) - j \frac{\sigma}{\omega\varepsilon_0} .$$

If the object of interest is a biological tissue, its dielectric properties result from the interaction of electromagnetic radiation with its constituents (cells, molecules) and, in particular, the interaction mechanisms, associated to polarization, vary depending on the incident field frequency[39].

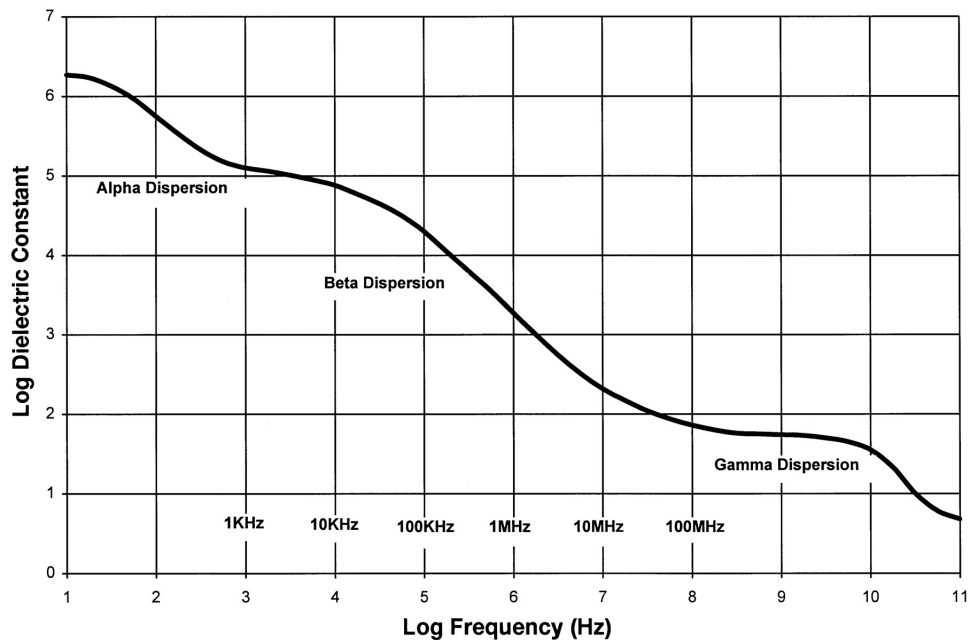


Fig.11: *Log dielectric constant of muscle tissue vs. log frequency in the  $\alpha$ ,  $\beta$ , and  $\gamma$  dispersion regions.*

The electric properties of a variety of tissues have been widely discussed and reviewed (Foster and Schwan, 1980 and 1989): different tissues (bone, blood, fat, muscle, etc.) have different permittivity values but exhibit a common trend respect to how permittivity varies with frequency. The spectrum is characterized by three main regions (Fig.11) referred to as  $\alpha$ -,  $\beta$ -, and  $\gamma$ -dispersion regions<sup>12</sup> where step changes in  $\epsilon_r$  are observed due to the loss of particular polarization processes as frequency increases[36][39]. At low frequency ( $\sim$  KHz), tissues have high permittivity due to the insulating cell membrane:  $\alpha$ -dispersion region depends from ionic flux across the membrane[39]. At intermediate frequency ( $\sim 10^2$  KHz), the  $\beta$ -dispersion occurs for the interfacial polarization of cell membrane systems (Maxwell-Wagner effect) which blocks the flow of ions between intra- and extra-cellular medium[37]. At high frequency ( $\sim$  GHz),  $\gamma$ -dispersion region is observed in correspondence of dipolar relaxation of water molecules in the tissues[17]. In microwave frequency range, the dominant relaxation mechanism is the dipolar relaxation of water molecules associated to  $\gamma$ -dispersion region, suggesting that water content is a major factor in determining tissue permittivity[41]. Low water content tissues, like fat, show lower permittivity values than high water content tissues, like muscle tissue.

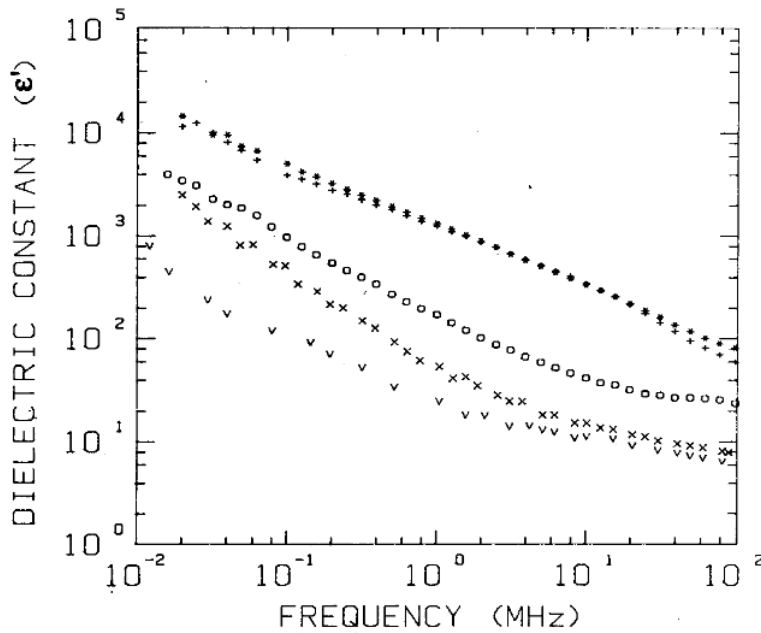


Fig.12: Dielectric constant of breast carcinoma as a function of frequency.

(\*): central part of tumor; (+): tissue surrounding the tumor;  
(o): adipose tissue containing infiltrating tumor cells; (x): peripheral sample distant 25 mm  
from central part of tumor; (v): normal breast tissue.

<sup>12</sup>Other minor dispersions such as the  $\delta$ -dispersion ( $\sim$  MHz) have been observed for certain tissues[35].

Several studies in the literature suggest that a large electrical contrast exists between normal breast tissues and malignant tumors[42]: measurements for various healthy and diseased tissues have indicated that tumors exhibit a greater permittivity (10–20%)[17]. In particular, normal breast tissue displays similar properties to fatty tissue, while for the corresponding characteristics tumor is more similar to muscle[17].

### 1.2.2 Dielectric Spectrum and Tissue Models

Biological tissues are naturally inhomogeneous and show considerable variability in structure and composition: dielectric properties differ widely among different tissues (inter-class variability) but also for the same kind of tissue from different specimen (intra-class variability). A concrete example is given by permittivity values of the same tissue for samples at different levels of aging[43].

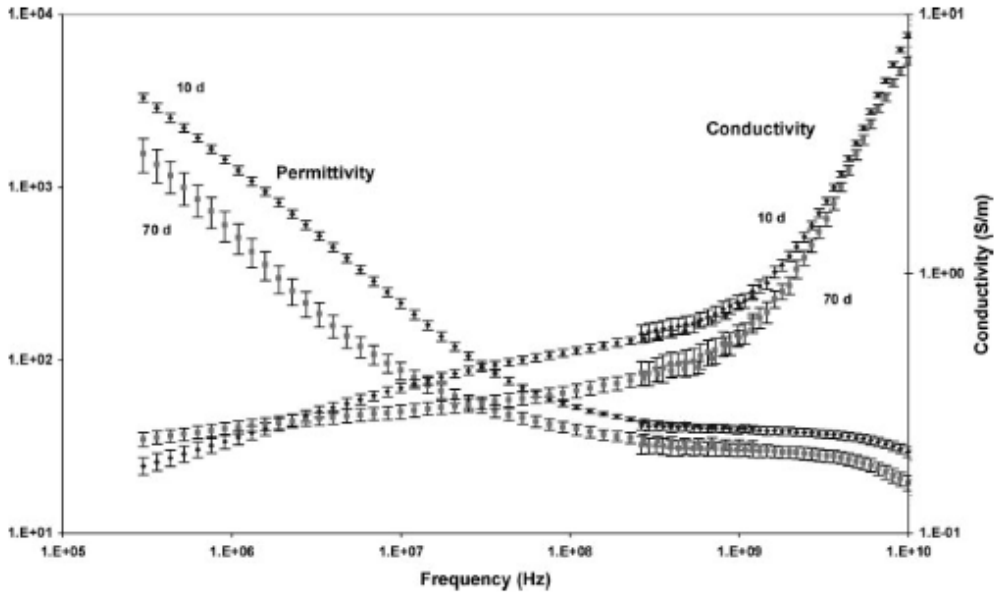


Fig.13: *Dielectric data for skin tissue in 10 and 70 day-old Wistar strain rats at 37°.*

As we saw, the permittivity of a single tissue can be characterized by at least three relaxation regions (fig.11), where each one resembles a typical polarization mechanism. In its simplest approximation, frequency-dependent dielectric relaxation of a material can be characterized by a single-time constant  $\tau$  response by the Debye equation

$$\varepsilon_r = \varepsilon_\infty + \frac{\varepsilon_s - \varepsilon_\infty}{1 + j\omega\tau} ,$$

where  $\varepsilon_r$  is the relative permittivity,  $\omega$  is the angular frequency,  $\varepsilon_\infty$  is the permittivity at field frequencies where  $\omega\tau \gg 1$ ,  $\varepsilon_s$  is the permittivity at which  $\omega\tau \ll 1$  and  $j = \sqrt{-1}$ . The magnitude of the dispersion is given by the difference  $\Delta\varepsilon = \varepsilon_s - \varepsilon_\infty$ . Li and Hagness (2001) have exploited a first order Debye dispersion with an additional conductivity term to fit published data (Fig.14) for healthy versus malignant tissue,

$$\varepsilon_r = \varepsilon_\infty + \frac{\Delta\varepsilon}{1 + j\omega\tau} - j\frac{\sigma_s}{\omega\varepsilon_0}, \quad (1.1)$$

where  $\sigma_s$  is the static ionic conductivity and  $\varepsilon_0$  the permittivity of free space.

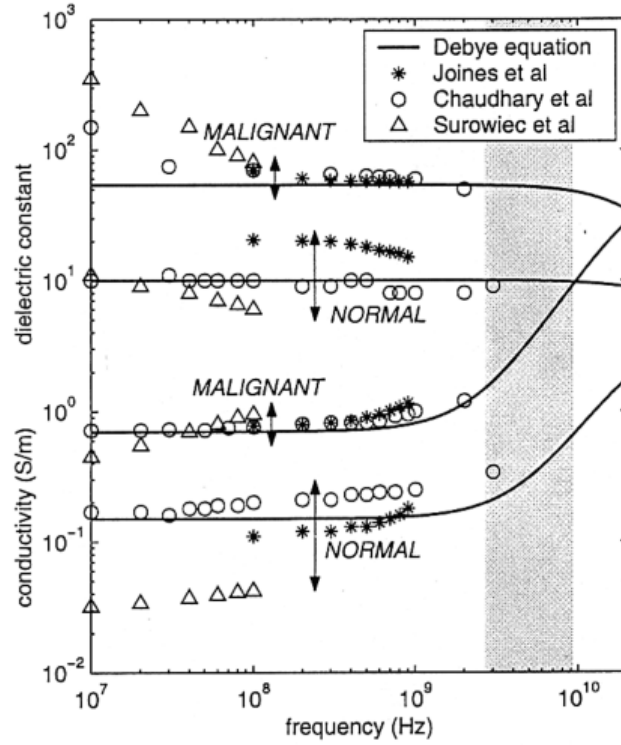


Fig.14: *Single-pole Debye curve fits of measures baseline dielectric-properties data for normal and malignant breast tissue at radio and microwave frequencies.*

In this study, the following Debye parameters have been chosen to fit the published data for normal against malignant breast tissue (up to 3GHz frequency)[44]:

- $\varepsilon_\infty = 7$  ,  $\varepsilon_s = 10$  ,  $\sigma_s = 0.15$  S/m ,  $\tau = 6.4$  ps (*normal, healthy breast tissue*);
- $\varepsilon_\infty = 4$  ,  $\varepsilon_s = 50$  ,  $\sigma_s = 0.7$  S/m ,  $\tau = 6.4$  ps (*malignant, diseased breast tissue*).

More complex models take into account the summation of multiple Debye dispersions, each one relative to a different relaxation mechanism:

$$\varepsilon_r(\omega) = \varepsilon_\infty + \sum_{n=1}^N \frac{\Delta\varepsilon_n}{1 + j\omega\tau_n}.$$

Hurt (1985) proposed a similar formulation to model the dielectric spectrum of the muscle (Fig.15), where five Debye dispersions were observed and the conductivity contribution was taken into account:

$$\varepsilon_r(\omega) = \varepsilon_\infty + \sum_{n=1}^5 \frac{\Delta\varepsilon_n}{1 + j\omega\tau_n} + \frac{\sigma_s}{j\omega\varepsilon_0} = \varepsilon_\infty + \sum_{n=1}^5 \frac{\Delta\varepsilon_n}{1 + (\omega\tau_n)^2} - j \left( \sum_{n=1}^5 \frac{\omega\tau_n\Delta\varepsilon_n}{1 + (\omega\tau_n)^2} + \frac{\sigma_s}{\omega\varepsilon_0} \right),$$

$$\varepsilon' = \varepsilon_\infty + \sum_{n=1}^5 \frac{\Delta\varepsilon_n}{1 + (\omega\tau_n)^2}.$$

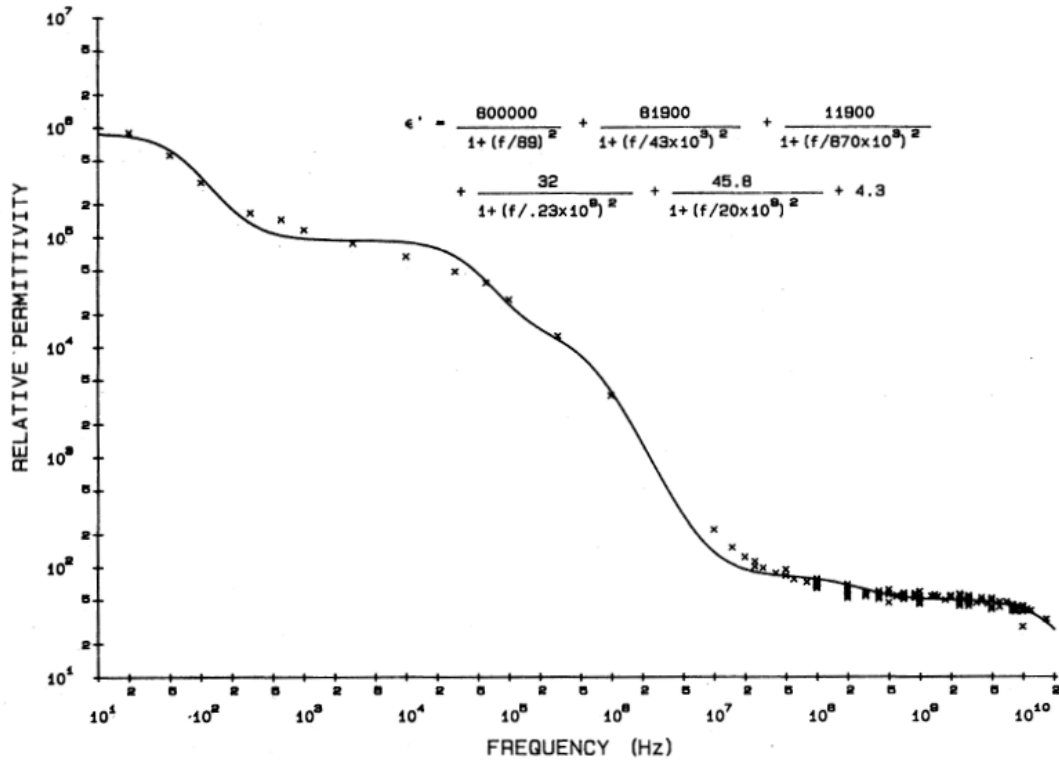


Fig.15: *Relative dielectric permittivity versus frequency: curve is best fit for five-term Debye expression respect to muscle published data[46].*

In Hurt study, the limit value  $\varepsilon_\infty$  was assumed to be equal to 4.3[46]. Although some of the published measurements differ by more than 20% from the obtained expression, most data are within 10% [46]: the empirical dispersion relations found by Hurt can be used as reasonable approximations for modelling the muscle tissue dielectric properties in the frequency range from 10 Hz to 100 GHz.

The complexity of biological tissues is such that it's possible to further consider multiple contributions for every dispersion region. The Cole-Cole equation takes into account in an empirical way the dispersion broadening by introducing a parametrical dependance in the Debye relaxation model,

$$\varepsilon_r(\omega) = \varepsilon_\infty + \frac{\Delta\varepsilon_n}{1 + (j\omega\tau)^{(1-\alpha)}} ,$$

where  $\alpha$ , which takes a value between 0 and 1, is the distribution parameter. The resulting dielectric spectrum can be rewritten in terms of multiple Cole-Cole dispersions, where each tissue has associated a specific parameter, and can be used to model the dielectric response over a certain frequency range:

$$\varepsilon_r(\omega) = \varepsilon_\infty + \sum_{n=1}^N \frac{\Delta\varepsilon_n}{1 + (j\omega\tau_n)^{(1-\alpha_n)}} + \frac{\sigma_s}{j\omega\varepsilon_0} .$$

A large-scale study performed by Lazebnik et al. [47][48] in 2007 employed a one-pole Cole-Cole model to analyze the dielectric properties of normal, malignant and benign breast tissues in the 0.5–20 GHz frequency range. They have showed that in normal breast tissue the dielectric properties are primarily determined by the adipose content of the sample, and that secondary factors (patient age, tissue temperature, excision to measurement time) generally have negligible effects on the overall dielectric behaviour of the sample[47][48]; dielectric properties of normal, healthy tissues span a very large range of values, from very low lipid-like ones to high ones approaching those of saline [47][48]; in contrast to healthy tissues, the malignant ones exhibit high values for dielectric properties enclosed in a small range, such that the dielectric contrast between malignant and normal, adipose dominated breast tissue is large as 10:1 when considering entirely adipose healthy tissue (85-100% fat content, low water content)[48]; the dielectric contrast between diseased and fibro-glandular breast tissue is much lower than the malignant versus normal-adipose one, approximately equal to 10%[48]; benign tissues (fibroadenomas and cysts) have similar dielectric properties to the lower-adipose (0-30% fat content, high water content) normal breast tissues[48].



# Chapter 2

## Reconstruction Algorithm

In the problem of detecting the presence of a small tumor inside an investigation domain by exploiting microwave radiation, one of the main aspects of interest is to develop and employ a procedure for *reconstructing* the scattering scenario, starting from the equations that govern electromagnetic scattering phenomena. The choice of experimental setup and tailoring of the algorithm in use should, in first place, take the imaging objective into consideration: MWI applications range from radar methods to object shape and dielectric full-profile reconstruction for a given scene.

In this thesis, the problem of detecting the presence of unknown scatterers, with successive localization by means of retrieving their spatial position from scattered field measurements, is addressed.

### 2.1 Electromagnetic Scattering Problem

In presence of a source which perturbs an incident field radiation, giving rise to the total field  $\mathbf{E}_T = \mathbf{E}_I + \mathbf{E}_S$  which have been introduced before, we expect to have two borderline cases, in terms of problem shaping.

In the first situation, we suppose to know everything about both the unperturbed field (before scattering occurs) and the object causing the field to scatter<sup>1</sup> and want to determine the perturbed radiation; this is defined as *direct scattering problem*. In this problem, a Fredholm linear integral equation of the second kind,

$$\mathbf{E}_T(\mathbf{r}) = \mathbf{E}_I(\mathbf{r}) + j\omega\mu_b \int_{V_0} \tau(\mathbf{r}') \mathbf{E}(\mathbf{r}') \cdot \vec{\mathbf{G}}(\mathbf{r}, \mathbf{r}') d\mathbf{r}' \quad (\text{data equation}), \quad (2.1)$$

where  $\tau(\mathbf{r}) = j\omega[\varepsilon(\mathbf{r}) - \varepsilon_b]$  is the *scattering potential*, must be solved in order to compute the total electric field vector  $\mathbf{E}_T$  (which is the only unknown) for any  $\mathbf{r}$  inside and

---

<sup>1</sup>This means we know the field  $\mathbf{E}_I(\mathbf{r})$  everywhere, the backing material dielectric properties  $(\varepsilon_b, \mu_b)$  and the object volume and dielectric properties  $\varepsilon(\mathbf{r}), \mu(\mathbf{r})$  of scattering source anywhere inside the object volume.

outside the object volume  $V_0$ [81]. In the second case, which is of predominant interest for microwave imaging, the object is completely unknown (volume, position, dielectric properties distribution) and we want to deduce information on it from measurements of the scattered field (Fig.16), which are usually collected in the space outside the investigated object by means of an antenna array; this is defined as *inverse scattering problem*.

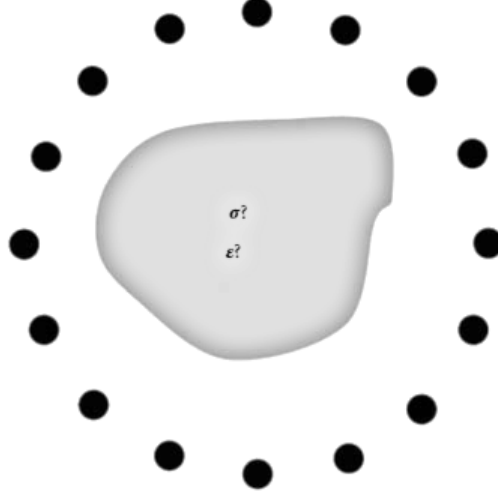


Fig.16: *The microwave inverse scattering problem.*

In this scenario, we assume to be able to measure only the total *external* electric field, which means anywhere *outside* the object volume  $V_0$ , and we derive an equation formally similar to the previous data equation, except now the field values are known everywhere outside  $V_0$  (data collection is performed in the domain volume  $V_m$ ),

$$\mathbf{E}_T(\mathbf{r}) = \mathbf{E}_I(\mathbf{r}) + j\omega\mu_b \int_{V_0} \tau(\mathbf{r}') \mathbf{E}(\mathbf{r}') \cdot \vec{\mathbf{G}}(\mathbf{r}, \mathbf{r}') d\mathbf{r}' , \quad \mathbf{r} \in V_m \text{ (data equation)} , \quad (2.2)$$

which is a Fredholm equation of the first kind[81]. Together with this equation, another related to the internal field distribution must be solved,

$$\mathbf{J}_{eq}(\mathbf{r}) = \tau(\mathbf{r}) \mathbf{E}_I(\mathbf{r}) + j\omega\mu_b \tau(\mathbf{r}) \int_{V_0} \mathbf{J}_{eq}(\mathbf{r}') \cdot \vec{\mathbf{G}}(\mathbf{r}, \mathbf{r}') d\mathbf{r}' , \quad \mathbf{r} \in V_0 \text{ (state equation)} . \quad (2.3)$$

The problem unknowns are the equivalent current density  $\mathbf{J}_{eq}$  and the scattering potential  $\tau$ . The solution of the inverse problem can be regarded as the search for the physical object that produces the *external* scattered field distribution, measurable in the observation domain  $V_m$ , and the *internal* field distribution, consistent with the known incident field, into the object volume  $V_0$ .

In general, as well as in the present thesis, the microwave image-reconstruction problem is addressed as a particular type of inverse problem.

## 2.2 Scattering as an Inverse Problem

From a mathematical point of view, it's arbitrary to define whether a problem is the direct or inverse part respect to its counterpart: according to J.B. Keller (1976), one generally calls two problems inverse to each other if the formulation of one problem involves the other one; for historical reasons, the direct problem is usually referred to as the one which has been studied or understood for the most part.

Physically, if we are to predict the future behaviour of a particular system from knowledge of its present state and the physical laws, we usually refer to a direct problem, while we can think of the corresponding inverse problem as the determination of the present state of the same system from future observations, leading to the calculation of the evolution of the system backwards in time[50].

One of the main difficulties associated to solving inverse problems in general, thus including the aforementioned inverse scattering problem, is the *ill-posedness*. According to the definition given by Hadamard, a problem is *well-posed* if it has a solution, which must be unique and it depends continuously on the data: if even one of these conditions is not satisfied, the problem is *ill-posed*.

Several difficulties arise in an attempt to solve an ill-posed problem: existence of an exact solution is not guaranteed; multiple solutions can be found as causes for an observed phenomenon; small perturbations of the data can lead to large perturbations of the solution (the problem is not stable). In imaging problems, where we try to obtain information on the scattering source from scattered field data, the ill-posedness leads to a variety of scenarios: for a given set of measurements, one can find no object at all or multiple objects at once producing the data, or substantially different objects giving place to very similar data-sets (large perturbation of the solution can take place from small perturbation of the data).

Although it is not possible to entirely swap an unstable problem into a stable one, a partial remedy to ill-posedness is given by the use of *regularization methods*, which in practice do establish a tradeoff between accuracy and stability in the reconstruction[50]. Applying a regularization procedure means to replace the original, unstable problem with a more stable one by exploiting additional *a-priori* information, for which we can obtain a solution in a simpler and more stable way and accept it as an approximate solution for the ill-posed problem[81]. This additional information is often given, in imaging applications, by knowing some of the physical features of the inspected object or the noise level of measured data.

Inverse problems are also *non-linear*, hence closed form methods to find the problem solution do not exist. Several approaches for solving non-linear, ill-posed inverse problems exist and are generally split into two main categories, which are the *linear methods* and the *non-linear methods*.

In the present thesis, we avail ourselves of a linear, Time-Reversal (TR) inversion method[49].

### 2.2.1 Non-Linear Methods

The non-linear reconstruction methods, often referred with the term *quantitative*, is a class of inversion techniques which includes all the ones based on “exact” models, theoretically valid for any scatterers, and that take into account the nonlinear nature of the inverse scattering problem[81]; quantitative methods can be further divided into *deterministic* and *stochastic*.

The quantitative, deterministic reconstruction algorithms are those procedures which aim at obtaining the distribution of electromagnetic parameters of the investigated scene by exploiting deterministic algorithms, that is by attempting to solve in a direct way the nonlinear systems of the electric field integral equations<sup>2</sup>, which relate the problem unknowns to the measured field values. This way, the reconstruction problem is treated as an iterative procedure with an optimization task to be fulfilled, usually involving the achievement of the minimum for a proper cost function. Common methods include the Newton-like iterative inversion schemes, as the Gauss-Newton (Meaney et al.[51][52]) or the Inexact-Newton (Pastorino et al. [53][54][55][56]), and the Distorted Born Iterative Method<sup>3</sup>(Winters et al. [57], Shea et al.[58], Khalil et a.[59]).

All of these methods rely on the use of a *forward solver* for equations involved in the scattering problem: the most widely used ones are the method of moments (MoM), the finite-element method (FEM) and the finite-difference time-domain (FDTD). By numerically solving the Maxwell’s equations, the continuous investigation domain becomes spatially discretized into a number of variables which are assigned the unknown dielectric properties values.

Regularization algorithms are always adopted along with non-linear reconstruction methods in order to control noise propagation and possibly avoid the achievement of meaningless solutions: classic examples include the Tikhonov method([57]), the truncated singular value decomposition method, the truncated Landweber method ([56]) and the conjugate gradient (Rubæk et al. [60]).

Optimization task of such a high-dimensional problem with many variables is not trivial and chances are high to trap into a local minimum: in order to suitably initialize the local optimization procedure and avoid false solutions, a-priori information should be included into the process and, if not available, search should be started from an approximate, linearized solution. By choosing the stochastic reconstruction algorithms instead, which are nonlinear, global optimization methods, the initial guess is not a critical aspect anymore since they are able to escape from local minima; they include, among others, simulated annealing (SA) algorithm and several population-based ones, like the genetic algorithm (GA); stochastic methods have proven an easier inclusion of a-priori information and capability to operate in a strongly noisy environment (Caorsi et al.[61]).

---

<sup>2</sup>EFIE have been previously introduced in the inverse electromagnetic scattering as the data and state equations.

<sup>3</sup>DBIM.

The main disadvantage of non-linear methods is their computational burden (stochastic) and presence of false solutions (deterministic); most often, they require parallel-computing and software optimization to provide suitable synergy between hardware and software in an attempt to significantly reduce acquisition time for the image.

### 2.2.2 Linear Methods

The linear reconstruction methods, often referred with the term *qualitative*, is a class of inversion techniques including all the ones which can retrieve only partial information about the scatterer under test, for example its shape or spatial location inside the investigation domain; it also includes the methods which are based on a certain approximation (Born-type, Rytov-type, Kirchoff-type), for which some a-priori knowledge about the object (weakly scattering source, perfectly conducting body) is required and thus the chosen, inexact model needs to be validated accordingly. Despite their intrinsic drawback, limiting the range of practical applications for which these methods can be exploited, a huge advantage is given in terms of computational efficiency, enabling fast and robust reconstructions[81]. In terms of MWI, only strong scatterers (e.g. tumor) detection is possible, which means it's not possible to obtain a quantitative reconstruction (i.e. dielectric properties distribution) of the breast; imaging problem is dramatically simplified, no false solutions exist and reconstruction is extremely quick if compared to non-linear methods.

Up until now, several linear inversion techniques have been developed in the breast cancer detection scene and three large families are generally acknowledged: beamforming methods, holographic methods and time-reversal methods.

Beamforming was one of the first linear inversion techniques to be developed and has been much studied since then. In the simplest Delay And Sum (DAS) configuration, which can work both in a monostatic and multistatic antenna configuration, reconstruction is performed by delaying the registered time-domain signals, according to a-priori information related to the wave propagation speed in the breast and test-point location, and summing them to obtain the image-pixel value; variants of the default modality include the Delay Multiply And Sum (DMAS) and the Improved Delay And Sum (IDAS, Klemm et al. [62]) algorithms, which have proven an overall better performance compared to DAS for the homogeneous, adipose case and a reduced improvement in the dense, fibroglandular case[63]. Other significant methods in the UWB beamforming framework are the Microwave Imaging via Space-Time (MIST) beamforming [64] and the Confocal Microwave Imaging (CMI) technique [44].

We usually address as *data independent* beamformers the ones employing an assumed propagation model to compensate for path dependent attenuation and dispersion, and as *data adaptive* those that perform signal processing in order to weigh the contributes

from different locations<sup>4</sup>; data-adaptive algorithms have been used to remove artifacts in the received signals due to backscatter from the skin-breast interface[64].

The microwave holographic methods (Fig.18) are based on coherent (magnitude and phase) back-scattered signal acquisition on a surface, similarly to conventional optical holography, with successive application of a sequence of direct and inverse Fourier transforms (FT)<sup>5</sup>: the surface data are simultaneously employed in an attempt to reconstruct the reflectivity distribution of the investigated object[66].

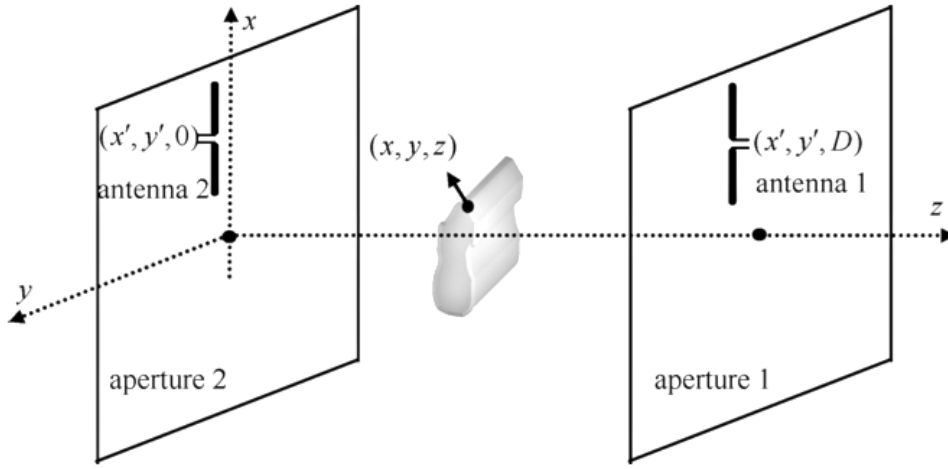


Fig.17: A 3D microwave holography setup scheme.

Finally, the time-reversal (TR) linear methods are based on time-reversibility of the wave equation in lossless and stationary media; the robustness of TR algorithms with respect to breast inhomogeneities has been demonstrated, suggesting it's a noticeably valid technique in breast cancer detection (Kosmas and Rappaport, 2005 [67]).

TR techniques (Fig.18) in general exploit multipath components in the investigation media to achieve *super-resolution* (i.e. resolution that beats the classical diffraction limit) and involve physical or synthetic retransmission of signals acquired by a set of transceivers in a time-reversed fashion (i.e. last-in, first-out): the retransmitted signals propagate backwards, reversing the path they underwent during forward propagation, resulting in an energy-focus around the initial source location[68]. The source can be either active (transceiver) or passive (scatterer). Their robustness, in terms of *statistical stability*, is given by the use of the techniques in UWB, making possible to operate at

<sup>4</sup>The early-time clutter consists of the incident pulse and reflections from the skin, while the late-time clutter is primarily due to the heterogeneity of breast tissue[44].

<sup>5</sup>Holographic methods are based on the linear Born approximation to achieve direct, non-iterative image reconstruction: by assuming that the object is a weak scatterer, reconstruction can be performed via FT[65].

low frequencies, resulting in more penetration in lossy material, and high frequencies, augmenting resolution, thus enabling the imaging procedure on random media[68].

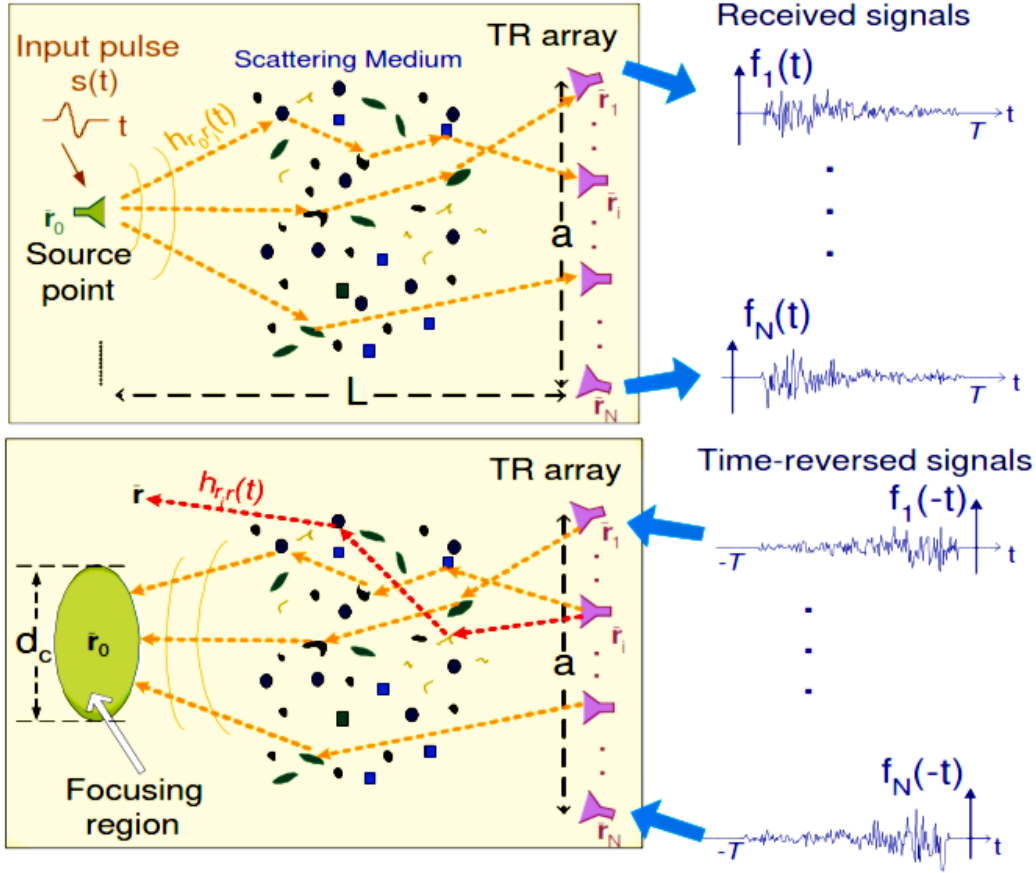


Fig.18: *Example of an active mode (source is a transceiver) time-reversal experiment, where  $h(t)$  is the impulse response between different antenna locations. Top image: forward propagation of the input pulse. Bottom image: backward propagation of the time-reversed signals.*

Examples of time-reversal algorithms are the Decomposition of the Time Reversal Operator (DORT) and Time Reversal-Multiple Signal Classification (TR-MUSIC), which both rely on the eigenspace analysis of the time-reversal operator; DORT computes and backpropagates each eigenvector corresponding to the significant, highest eigenvalues (i.e. signal subspace) of the data matrix, resulting in scatterer focusing (present sources must be well resolved); TR-MUSIC performs an equivalent operation on the data matrix, with the difference it exploits the complementary space to signal subspace (i.e. eigenvectors associated with near zero eigenvalues[68]), and retrieves a projection operator, the *pseudospectrum*, which peaks in correspondence of the scatterer location. It has been shown

that time-domain DORT is outperformed by TR-MUSIC under weak clutter conditions, but this last has proven to be less stable under increased clutter[68]; both methods, especially TR-MUSIC, can achieve improved focusing ability also in the presence of clutter due to dense fibroglandular tissue[69].

In the present thesis, the MWI problem is addressed by means of a TR-MUSIC reconstruction algorithm, for which a further explanation is given in the next section.

## 2.3 TR-MUSIC

For real-valued, time-dependent signals, expressible in the Fourier integral form,

$$X(t) = \frac{1}{2\pi} \int_{-\infty}^{\infty} d\omega \tilde{X}(\omega) e^{-i\omega t}$$

$$\tilde{X}(\omega) = \int_{-\infty}^{\infty} dt X(t) e^{i\omega t} ,$$

it can be shown that time-reversal operation (in time domain) is equivalent to phase conjugation in the frequency domain: we want to solve the electric field integral equations in the discrete frequency domain.

### 2.3.1 TR Formulation in Multistatic Antenna Configuration

We consider an array of  $N$  antennas (Fig.19), each one located at the space point given by the vector  $\mathbf{R}_j$  ( $j = 1, 2, \dots, N$ ), where each antenna radiates a scalar field  $\psi(\mathbf{r}, \omega)$  into a half-space ( $z > 0$ ) which has embedded the scatterers we are to detect (investigation domain). We further assume that the antennas can be treated as ideal, infinitesimal dipoles (Hertzian dipoles), the targets are ideal point scatterers and we neglect multiple scattering between targets.

The wavefields radiated by the  $j$ -th antenna (incident field) and scattered by the buried sources can be described by the equations

$$\psi_j^{(i)}(\mathbf{r}, \omega) = G(\mathbf{r}, \mathbf{R}_j) e_j(\omega)$$

$$\psi_j^{(s)}(\mathbf{r}, \omega) = \sum_{m=1}^M G(\mathbf{r}, \mathbf{X}_m) \tau_m(\omega) G(\mathbf{X}_m, \mathbf{R}_j) e_j(\omega) ,$$

where  $\tau_m$  is the target scattering amplitude,  $\mathbf{X}_m$  is the location of the  $m$ -th target, for all possible ( $m = 1, 2, \dots, M$ ) scatterers,  $e_j$  is the  $j$ -th antenna excitation voltage and  $G(\mathbf{r}, \mathbf{r}')$  is the Green's function of the background medium.



By explicitly writing the total radiated and scattered electric fields<sup>6</sup>, corresponding to when the entire array is excited, we obtain

$$E^{(i)}(\mathbf{r}, \omega) = \sum_{j=1}^N E_j^{(i)}(\mathbf{r}, \omega) = \sum_{j=1}^N G(\mathbf{r}, \mathbf{R}_j) e_j(\omega)$$

$$E^{(s)}(\mathbf{r}, \omega) = \sum_{j=1}^N E_j^{(s)}(\mathbf{r}, \omega) = \sum_{j=1}^N \sum_{m=1}^M G(\mathbf{r}, \mathbf{X}_m) \tau_m(\omega) G(\mathbf{X}_m, \mathbf{R}_j) e_j(\omega) .$$

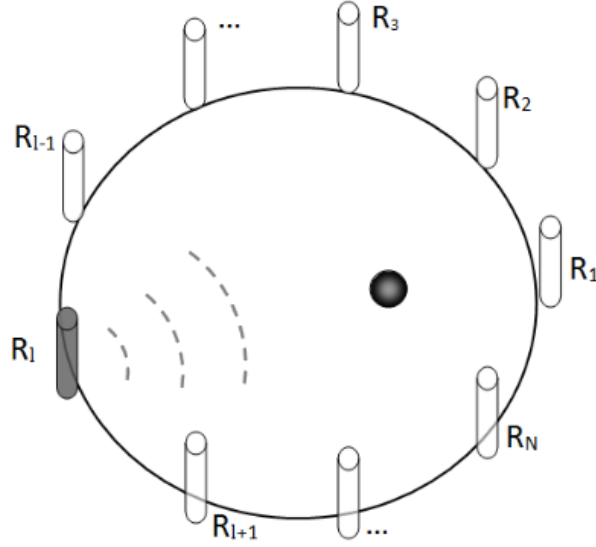


Fig.19: *TR-MUSIC in multistatic configuration scheme: once for each antenna, we have it act both as transmitter and receiver, while the remaining ones receive only.*

Now, the measured voltage output  $v_l(\omega)$  is given by the amplitude of the total scattered field collected at  $l$ -th antenna:

$$v_l(\omega) = \sum_{j=1}^N E_j^{(s)}(\mathbf{R}_l, \omega) = \sum_{j=1}^N \sum_{m=1}^M G(\mathbf{R}_l, \mathbf{X}_m) \tau_m(\omega) G(\mathbf{X}_m, \mathbf{R}_j) e_j(\omega) .$$

By introducing the Green's function column vector compact notation,

$$g_m(\omega) = \{G(\mathbf{R}_l, \mathbf{X}_m)\} = [G(\mathbf{R}_1, \mathbf{X}_m), G(\mathbf{R}_2, \mathbf{X}_m), \dots, G(\mathbf{R}_N, \mathbf{X}_m)]^T ,$$

---

<sup>6</sup> $\psi(\mathbf{r}, \omega) = E(\mathbf{r}, \omega)$ .

we can define the *multistatic response matrix* as

$$A(\omega) = \{A_{l,j}\} = \sum_{m=1}^M G(\mathbf{R}_l, \mathbf{X}_m) \tau_m(\omega) G(\mathbf{X}_m, \mathbf{R}_j) e_j(\omega) = \sum_{m=1}^M g_m \tau_m(\omega) g_m^T .$$

The response matrix  $A$  is a matrix propagator so that the element  $(j, i)$  represents the total field received by the  $j$ -th element when  $i$ -th element is “fired”. The output voltage registered by the  $l$ -th antenna, in the multistatic case can be finally rewritten as

$$v_l(\omega) = \sum_{j=1}^N A_{l,j} e_j = A(\omega) \bar{e}(\omega) ,$$

where  $\bar{e} = [e_1, e_2, \dots, e_N]^T$  is the input-voltage vector. By computing this for each antenna, we can obtain the voltage-output vector  $\bar{v} = [v_1, v_2, \dots, v_N]^T$  for the multistatic case. It's possible to define the following correlation matrix, defined as Time Reversal Matrix,

$$T(\omega) = A^\dagger(\omega) A(\omega) = A^*(\omega) A(\omega) ,$$

where the symbols  $^\dagger, *$  denote respectively the adjoint and complex conjugate, so the second equality follows from the simmetry of  $A$ . The eigenvectors of the  $T$  matrix with non-zero eigenvalues build the signal space  $\mathcal{S}$ , while the eigenvectors with zero eigenvalues build the noise space  $\mathcal{N}$  (these spaces are orthogonal). Explicit calculus yields to

$$T(\omega) = \left[ \sum_{m=1}^M \tau_m g_m g_m^T \right]^* \left[ \sum_{m'=1}^M \tau_{m'} g_{m'} g_{m'}^T \right] = \sum_{m=1}^M \sum_{m'=1}^M \Lambda_{m,m'} g_m^* g_{m'}^T ,$$

where  $\Lambda_{m,m'} = \tau_m^* \tau_{m'} \langle g_m, g_{m'} \rangle = \tau_m^* \tau_{m'} \sum_{n=1}^N g_m^*(n) g_{m'}(n)$  .

The time reversal matrix  $T$  is Hermitian and non-negative, thus it possesses a complete set of orthonormal eigenvectors having non-negative eigenvalues; if the number of scatterers inside the domain is equal or inferior to the number of antennas and the rank of  $T$  is equal to  $M$ , there are exactly  $M$  non-zero eigenvalues[49].

### 2.3.2 Multiple Signal Classification

The MUSIC algorithm, used in conjunction with TR processing, makes use of the fact that the time-reversal matrix  $T$  is a projection operator onto the subspace  $C^N$  spanned by the complex conjugates of the Green's function vectors<sup>7</sup> (i.e. the signal subspace  $\mathcal{S}$ ) and that the noise subspace  $\mathcal{N}$  is spanned by the eigenvectors of  $T$  having zero eigenvalue,

---

<sup>7</sup>In the case of well-resolved targets, the eigenvectors of the time-reversal matrix spanning the signal subspace are the complex conjugates of the Green's function vectors.

where  $C^N = \mathcal{S} \oplus \mathcal{N}$ . It follows that the complex conjugate of each Green's function vector must be orthogonal to the noise subspace and, in particular, to the eigenvectors of the time-reversal matrix having zero eigenvalues:

$$\langle \mu_{m_0}, g_m^* \rangle = \langle \mu_{m_0}^*, g_m \rangle = 0 ,$$

where  $\mu_{m_0}$  are the eigenvectors of  $T$  having zero eigenvalue in the case we have  $m = 1, 2, \dots, M$  scatterers and  $N$  antennas<sup>8</sup>.

We can define the *pseudospectrum* quantity as

$$P(\mathbf{R}_p) = \frac{1}{\sum_{m_0=M+1}^N |\langle \mu_{m_0}^*, g_p \rangle|^2} , \quad (2.4)$$

where  $g_p$  is defined as *steering vector*,

$$g_p(\omega) = \{G(\mathbf{R}_l, \mathbf{R}_p)\} = [G(\mathbf{R}_1, \mathbf{R}_p), G(\mathbf{R}_2, \mathbf{R}_p), G(\mathbf{R}_N, \mathbf{R}_p)]^T ,$$

which is the Green's function vector evaluated for a target at the *test location*  $\mathbf{R}_p$  and for which it's fundamental to have some knowledge about the background Green's function. By noticing that the denominator in (2.4) is equal to the magnitude square of the projection of the complex conjugate of the steering vector onto the noise subspace, pseudospectrum can be written as

$$P(\mathbf{R}_p) = \frac{1}{|P_{\mathcal{N}}[g_p^*]|^2} = \frac{1}{|(I - P_{\mathcal{S}})[g_p^*]|^2} ,$$

where  $P_{\mathcal{S}}$  and  $P_{\mathcal{N}}$  are respectively the signal subspace and noise subspace projection operators, for which  $P_{\mathcal{S}} + P_{\mathcal{N}} = I$  holds[70]. Since the signal subspace  $\mathcal{S}$  is orthogonal to the noise subspace  $\mathcal{N}$ , the inner product  $\langle \mu_{m_0}^*, g_p \rangle$  will vanish when the test location is equal to the actual location of the target: this means that the pseudospectrum  $P$  will have a peak (theoretically to infinity) at each target location, enabling to detect scatterers in a deterministic way<sup>9</sup>.

Thus, with this algorithm it's possible to perform time-reversal imaging.

### 2.3.3 TR-MUSIC in Monostatic Antenna Configuration

The imaging system employed in the current thesis has a simpler configuration than the multistatic one discussed above.

---

<sup>8</sup>The number of eigenvectors having zero eigenvalue is  $m_0 = M + 1, M + 2, \dots, N$ .

<sup>9</sup>Sources are localized by finding the steering vectors which are orthogonal to the noise subspace[70].

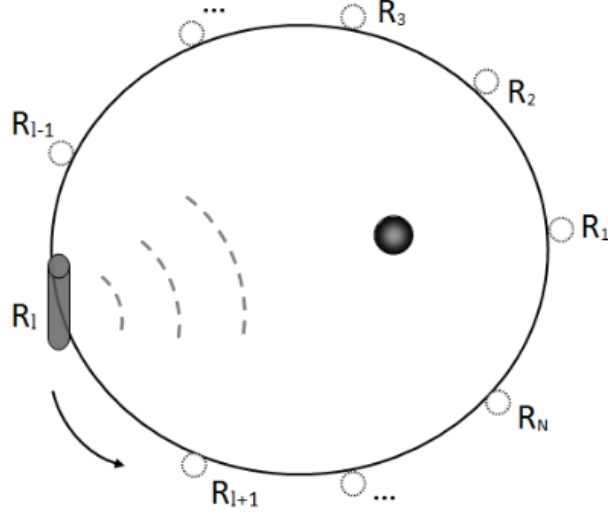


Fig.20: *TR-MUSIC in monostatic configuration: a single transceiver irradiates the investigation domain and then collects scattered field data for different positions.*

In the *monostatic antenna configuration*, a single antenna (Fig.20) acts both as transmitter and receiver for a fixed number of positions, and for each of these a measure of the scattered electric field is recorded. In this case, the response matrix  $A(\omega)$  reduces to a vector since the collected signal is always associated to the same antenna that “fired” the excitation pulse, so that the measured voltage output collected at each antenna location

$$v_l(\omega) = E_l^{(s)}(\mathbf{R}_l, \omega) = \sum_{m=1}^M G(\mathbf{R}_l, \mathbf{X}_m) \tau_m(\omega) G(\mathbf{X}_m, \mathbf{R}_l) e_l(\omega) = A_l(\omega) e_l(\omega) ,$$

can be rewritten in the compact form

$$\bar{v}(\omega) = \bar{A}(\omega) \bar{e}(\omega) ,$$

where  $\bar{A}(\omega) = [A_1(\omega), A_2(\omega), \dots, A_N(\omega)]^T$  is the *monostatic response* and  $\bar{e} = [e_1, e_2, \dots, e_N]$  is the input-voltage vector. The imaging procedure aims at detecting the presence of a scattering source by finding the steering vector

$$\bar{A}(\mathbf{R}_p, \omega) = [G(\mathbf{R}_1, \mathbf{R}_p) \tau G(\mathbf{R}_p, \mathbf{R}_1), G(\mathbf{R}_2, \mathbf{R}_p) \tau G(\mathbf{R}_p, \mathbf{R}_2), \dots, G(\mathbf{R}_N, \mathbf{R}_p) \tau G(\mathbf{R}_p, \mathbf{R}_N)]^T$$

which is orthogonal to the noise subspace  $\mathcal{N}$  in the trial point  $\mathbf{R}_p$ , in order to have the pseudospectrum peak. The achievable imaging performance can be equivalently and more conveniently studied by exploiting the projection operator onto the signal subspace respect to the steering vector  $\bar{A}_p(\omega) = \bar{A}(\mathbf{R}_p, \omega) / \|\bar{A}(\mathbf{R}_p, \omega)\|$  ,

$$\|P_{\mathcal{N}} [\bar{A}_p(\omega)]\|^2 = \|(I - P_{\mathcal{S}}) [\bar{A}_p(\omega)]\|^2 = 1 - \|\langle \bar{A}_p(\omega), \bar{\mu}(\omega) \rangle\|^2 ,$$

where  $\bar{\mu}(\omega) = \bar{v}(\omega)/\|\bar{v}(\omega)\|$  is the single eigenvector corresponding to the theoretically strongest eigenvalue different from zero, in the single scattering source assumption[70], given, in monostatic environment, by the signal collected at each antenna location. The pseudospectrum value at the corresponding test-location  $\mathbf{R}_p$  can thus be calculated as

$$P(\mathbf{R}_p, \omega) = \frac{1}{1 - \|\cos \eta_p\|^2} , \quad (2.5)$$

where we associated the projection of the steering vector  $\bar{A}_p(\omega)$  over the strongest eigenvalue  $\bar{\mu}(\omega)$  with the  $n$ -dimensional scalar product in  $C^N$ ,

$$\cos \eta_p = \frac{\langle \bar{A}_p(\omega), \bar{\mu}(\omega) \rangle}{\|\bar{A}_p(\omega)\| \cdot \|\bar{\mu}(\omega)\|} ,$$

which still enhances the correlation between test and signal vector while forming the visual image and peaks in proximity of the scatterer position[71].

The range of values of the *correlation term*, associated to the square modulus of  $\cos \eta_p$ , is between 0 and 1; we can interpret it as the probability that the measured signal vector  $\bar{\mu}(\omega)$  is actually given by a single-scattering process, occurring in test-point location  $\mathbf{R}_p$ , which is described, respect to each measurement point (i.e.  $l$ -th antenna location), by the product of an outward ( $G(\mathbf{R}_l, \mathbf{R}_p)$ ) and inward ( $G(\mathbf{R}_p, \mathbf{R}_l)$ ) Green's vector.

### 2.3.4 Background Green's Functions

Modeling of the Green's function propagation vector is necessary in order to compute the steering vector and reconstruct image, and requires both knowledge of the exploited antenna elements and investigated domain (background) properties. In the current thesis, we shall use and compare the reconstruction results obtained with two different kinds of background Green's functions:

- 2D Hankel propagator;
- 3D Hertzian propagator (within scalar approximation).

For the two-dimensional imaging problem, we exploit the standard free-space Green's function given by the Hankel function of the second type and zeroth order,

$$G_{2D}(\mathbf{r}, \mathbf{r}', \omega) = -\frac{j}{4} H_0^{(2)}(k|\mathbf{r} - \mathbf{r}'|) , \quad (2.6)$$

which models the propagation of the travelling wave with wavenumber  $k = \omega/c$  between  $\mathbf{r}$  and  $\mathbf{r}'$ <sup>10</sup>. The case of two space dimensions corresponds physically to when the antennas

---

<sup>10</sup>Or viceversa, due to reciprocity  $G(\mathbf{r}, \mathbf{r}', \omega) = G(\mathbf{r}', \mathbf{r}, \omega)$ [72].

are line sources and targets line scatterers, all perpendicular to the plane  $R^2$ ; from a purely mathematical point of view one can just as well consider the antenna elements and the scatterers as point-like sources in  $R^2$ [49].

The background Green's functions can be calculated, for the three-dimensional case, from a relationship between the source current, characteristic of the antenna in use, and the incident field. If we consider a  $z$ -polarized, ideal dipole-antenna of length  $l$  characterized by a  $z$ -directed source current  $I_0$ , the corresponding DGF(2) can be calculated as

$$\vec{\mathbf{G}}_{back}(\mathbf{r}, \mathbf{r}', \omega) = \frac{1}{k\eta I_0 l} \begin{bmatrix} 0 & 0 & 0 \\ 0 & 0 & 0 \\ E_x(\mathbf{r}, \omega) & E_y(\mathbf{r}, \omega) & E_z(\mathbf{r}, \omega) \end{bmatrix},$$

where  $\eta$  is the wave impedance and  $k$  is the wavenumber<sup>11</sup>. The first two rows of the tensor are zeroed since no  $x$ -directed or  $y$ -directed sources are used. When the scalar field approximation is used, cross-polarization scattering effects are assumed to be negligible, thus  $E_x$ ,  $E_y$  are set to zero and the tensor is reduced to a single element[57].

In the scalar and point-like source approximations, we have thus used the following Green's function propagator for the 3D case:

$$G_{3D}(\mathbf{r}, \mathbf{r}', \omega) = \frac{E_z(\mathbf{r}, \omega)}{k\eta I_0 l}.$$

The value of  $E_z$ , for any  $\mathbf{r}$  inside the imaging domain, has been computed by evaluating the  $z$ -axis projections of field components  $E_\theta$ ,  $E_r$  associated to the Hertzian dipole total electric field(3):

$$E_z(\mathbf{r}, \omega) = E_\theta(\mathbf{r}, \omega) \sin \theta + E_r(\mathbf{r}, \omega) \cos \theta.$$

In radiation scattering, we mainly make use of the *radiation term*, for which  $E_r$  vanishes (see end of Appendix B), obtaining

$$G_{3D}(\mathbf{r}, \mathbf{r}', \omega) \simeq \frac{E_\theta(\mathbf{r}, \omega) \sin \theta}{k\eta I_0 l} = iG_0(\mathbf{r}, \mathbf{r}') \sin^2 \theta, \quad (2.7)$$

where  $G_0$  is the tridimensional Green's function in free-space(1).

### 2.3.5 Multi-Frequency Imaging

The TR-MUSIC algorithm proposed so far is exploited in a multi-frequency approach in order to achieve a better performance than the single-frequency case: it has been shown

---

<sup>11</sup>Ideal sources as the infinitesimal dipole are worthy of consideration when the focus is limited to the algorithm. Moreover, as antennas are generally characterized in terms of far-field behavior, the choice of best performing antenna in a complex near-field scenario is not obvious, for a particular imaging application.

(Ruvio et. al [70]) that single-frequency approaches heavily suffer from *undersampling*, leading to the rise of *artefacts* (i.e. source replicas) which corrupt the pseudospectrum and prevent scatterer detection and, due to the rank deficiency of the time reversal matrix, when *multiple sources* populate the investigation domain the performance degrades accordingly. To employ the data collected at different frequencies and achieve a performance enhancement in reconstruction, we have the single pseudospectra, obtained at a given frequency, combined incoherently into a recombined, improved pseudospectrum. Different methods can be exploited to perform the recombination procedure. We shall use the wide-band MUSIC and the interferometric MUSIC, which have been extensively studied and applied in TR imaging procedures. By defining the single-frequency image by means of the single-frequency pseudospectrum as the quantity

$$P_i = P(\omega_i) = \frac{1}{1 - \|\cos \eta_i\|^2} ,$$

obtained at frequency  $\omega_i$  , the corresponding WB-MUSIC and I-MUSIC recombined pseudospectra are given by the following expressions,

$$P_{WB} = \left[ \sum_{i=1}^N \frac{1}{P_i} \right]^{-1} , \quad (2.8)$$

$$P_I = \frac{1}{\left| \log \left( \prod_{i=1}^N \|\cos \eta_i\| \right) \right|} , \quad (2.9)$$

where N is the total number of unique frequencies.

By using the multi-frequency recombination method, we expect to observe a significant mitigation of artefacts occurrence, since their appearance at different locations is frequency dependent, as well as multiple-sources detection ability[70]. These methods will be used both for 2D and 3D pseudospectra.

## 2.4 Reconstruction Supplementary Processes

Generally speaking, a *complete* reconstruction procedure comprises several aspects, which should all be carefully evaluated as much as the reconstruction algorithm itself in order to achieve a *high quality* imaging. It's customary to divide them into pre-processing and post-processing features, as to characterize whether they should precede or follow the image reconstruction phase, defined as the moment where a dedicated algorithm returns an image (i.e. the pseudospectrum) of the investigated domain (i.e. breast or phantom) by means of scattered field data.

Among the most important processing tasks to be accomplished *before* the reconstruction algorithm is run we mention the signal filtering, which mainly aims at removing or reducing the unwanted contributions from clutter signal, thus enhancing the overall reconstruction quality, and the preliminary assesment of scattering scenario, whose primary focus is the estimation of important breast features (i.e. dielectric permittivity), which are then exploited in order to optimize the computational routine as well as to obtain a better imaging outcome.

Furthermore, considerations have to be taken *after* reconstruction is accomplished: it's fundamental to equip ourselves with useful tools to let us evaluate the goodness of the reconstruction, as well as to compare the results provided by different ones. Last but not least, images returned by reconstruction can be further enhanced in many, different ways; the same MUSIC algorithm is used by us to get an improved, multi-frequency image by “mixing” ones reconstructed at different frequencies but, in line of principle, its actual use can be extended to a different one than image recombination by frequency.

### 2.4.1 Signal Filtering and Clutter Cancellation

Several artifact removal algorithms have been proposed in the MWI scene. In order to properly reconstruct the scatterer position, a right estimate of the scattered field component must be achieved by filtering out unwanted contributions, which are usually given by a variety of factors (e.g. antenna and skin reflections, clutter). The simplest filtering method which can be adopted is called *average subtraction* since it's based on considering artifact formation in the pseudospectrum image as an *average* of the signal recorded at each antenna: artifact can thus be removed by subtracting the *mean of signals* from each  $i$ -th antenna individual signal, obtaining the *subtracted mean signal*

$$\mathbf{S}_{filtered}(\omega) = \mathbf{S}_{recorded}(\omega) - \mathbf{J}_{1,N} \frac{1}{N} \sum_{i=1}^N S_{recorded}^i(\omega) , \quad (2.10)$$

where  $N$  is the total number of antenna acquisitions in monostatic configuration, at a given frequency  $\omega$  and the signal vectors  $\mathbf{S}_{filtered}$  and  $\mathbf{S}_{recorded}$  respectively represent the collection of the individual filtered and raw signals from  $N$  antenna positions ( $\mathbf{J}_{1,N}$  is a  $N$ -dimensional vector-of-ones). The measured signal  $S_{recorded}^i$  in monostatic configuration is simply given by the reflected-to-incident wavefield ratio for the  $i$ -th antenna,

$$S_{recorded}^i = \frac{b_i}{a_i} , \quad (2.11)$$

where  $a_i$  and  $b_i$  respectively represent the incident (i.e. emitted) and reflected wavefields.



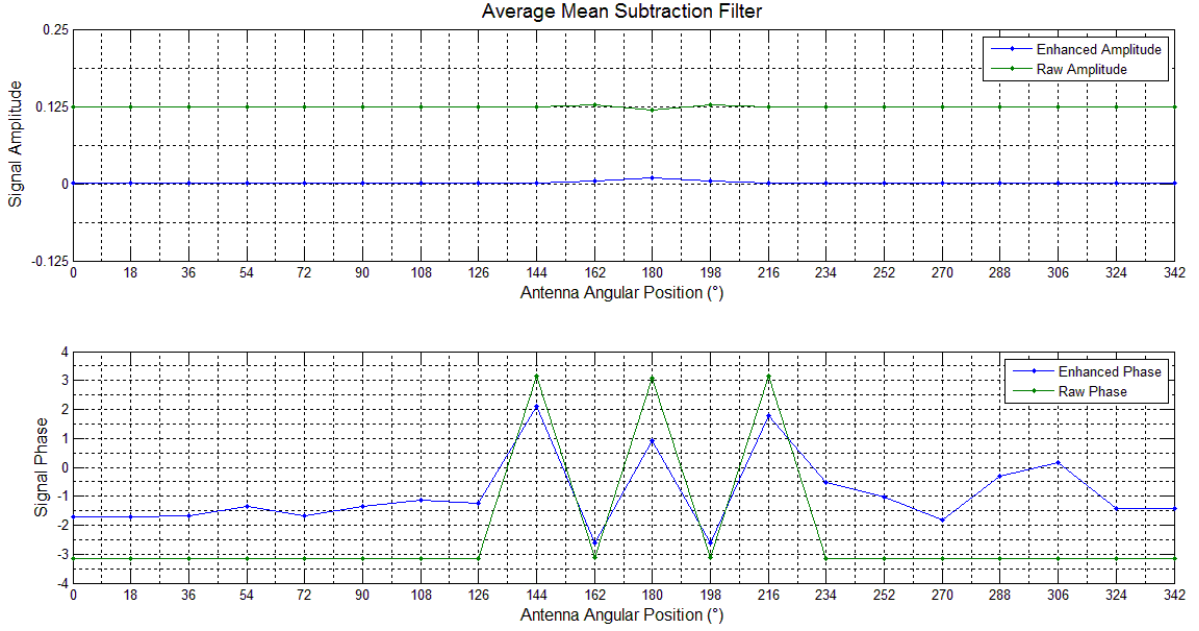


Fig.21: *Signal amplitude (top) and signal phase (bottom) graphs of the filtered and raw signal. The original signal is acquired by the same antenna in different angular positions respect to an imaging domain where a scatterer has been embedded.*

The additive component we are removing is usually about two order of magnitude greater than the wanted signal scattered from the source.

This particular method is valid because of the particular central-symmetry of the problem involved, where an antenna collects measurements by shifting of discrete angular step movements around a cylindrical domain: apart from statistical fluctuations, so, the average value of the additive component is expected to be constant along the antenna motion around the breast [71].

It has been proven that the average subtraction artifact removal algorithm performs worse than other more complex filters, especially in a more realistic scenario where early-time artifacts are due to local variation in skin thickness, breast heterogeneity and differences in antenna-skin distances (Elahi et al., [73]). Among these filtering algorithms it's noteworthy mentioning *Wiener Filter*, Recursive Least Squares (RLS), Singular Value Decomposition (SVD) and neighborhood-based hybrid algorithm (Maklad et al., [74]).

## 2.4.2 Preliminary Assesment of Domain Properties

Gaining an insight into present breast properties, spanning features from geometrical nature (e.g. skin layer thickness and surface extension) to eletric one, can lead us to a more accurate and efficient imaging procedure.

Preliminary assesment of outer layer properties, which are addressed major reflection contributions even in presence of a proper matching medium between breast and transceiver, is fundamental in order to apply effective methods for removing skin artefacts while enhancing the signal coming from the internal structure, thus reducing blurring and other corruption effects. Also knowing the average dielectric permittivity and conductivity of the interior breast, before imaging occurs, can help in smoothing the reconstruction by optimizing the focusing stage (linear methods) or setting a better starting point (non-linear methods).

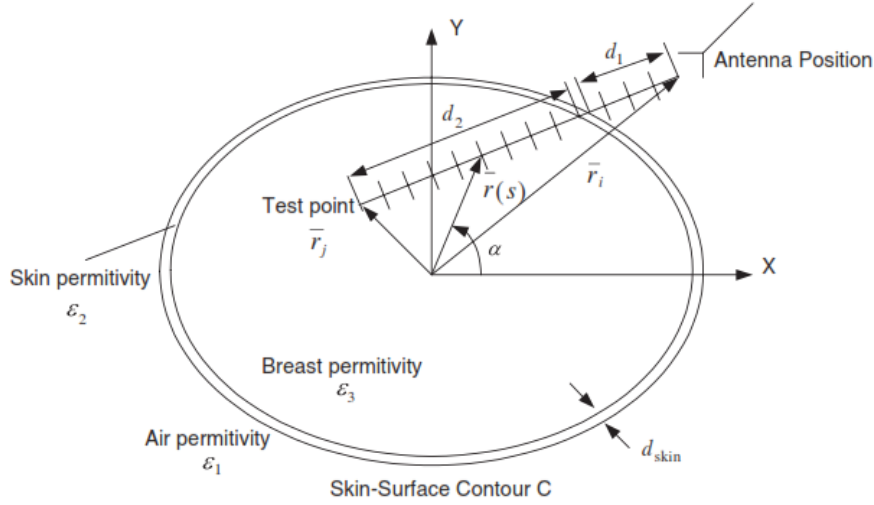


Fig.23: *Breast phantom imaging representation.*

An example of how these preliminary information can come to a concrete use is given by a rough model (Fig.23) for calculating the signal propagation delay between the  $i$ -th antenna and the test-point  $\mathbf{r}_j$ , which is given by

$$\tau_{ij} = \frac{2d_1}{c/\sqrt{\varepsilon_{medium}}} + \frac{2d_{skin}}{c/\sqrt{\varepsilon_{skin}}} + \frac{2d_2}{c/\sqrt{\varepsilon_{breast}}}$$

in monostatic topology, where  $c$  is the light velocity ( $c = 3 \cdot 10^8 m/s$ ),  $d_1$  is the distance between the antenna position  $\mathbf{r}_i$  and the outer skin-surface,  $d_{skin}$  is the skin thickness and  $d_2$  is the distance between the inner skin surface and the test point<sup>12</sup>;  $\varepsilon_{back}$ ,  $\varepsilon_{skin}$  and  $\varepsilon_{breast}$  are the relative dielectric permittivities of the antenna-breast coupling medium, skin and breast, respectively [75]. This value is very important in the tailoring of algorithms which aim at filtering out the signal associated to skin-reflection, by determining proper skin-dominant time-windows: this is because the “good” signal, coming from the

---

<sup>12</sup> $d_2 = |\mathbf{r}_j - \mathbf{r}_i| - d_1 - d_{skin}$ .

inner breast region, is preceded by an unwanted signal (mainly due to outer layer reflections) which is assumed to be the only contribute recorded for the entire duration of this early time-window.

When realistic, more complex problems which concern the reconstruction of inhomogeneous scenarios are tackled, a preliminary, viable approach is to find an approximate solution to the problem by trying to estimate some equivalent, average properties of the domain, thus reducing the actual inhomogeneous problem to an homogeneous one[76]. Breast properties average approximations can be obtained by performing a statistical analysis for breast phantom data; the University of Wisconsin Cross-Disciplinary Electromagnetics Laboratory (UWCEM) Numerical Breast Phantom Repository<sup>13</sup> contains a number of MRI-derived, numerical breast phantoms whose breast tissues include the realistic, ultrawideband dielectric properties reported in Lazebnik ([47][48]).

The freely available phantom data-sets are organized for *radiographic-density class*, defined by the following American College of Radiology (ACR) 4-level scale:

- Class 1 - Almost entirely fatty (< 25% glandular tissue);
- Class 2 - Scattered areas of fibroglandular density (25-50% glandular tissue);
- Class 3 - Heterogeneously dense (51-75% glandular tissue);
- Class 4 - Extremely dense (> 75% glandular tissue).

The volumetric, grid data is “unrolled” to one-dimensional data: a single phantom-data set is characterized by two vector arrays of data<sup>14</sup>,  $\vec{m}$  and  $\vec{p}$ , which provide information on the assumed tissue-composition and resultant dielectric properties. In particular, each image voxel  $i$  is assigned a couple of values  $(m_i, p_i)$  which denote its *media number*, a numerical index for characterizing the voxel estimated tissue type, and *probability value* ( $p \in [0, 1]$ ), which directly corresponds to the voxel dielectric property value (i.e. higher probability corresponds to a higher dielectric value). The probability value corresponding to the non normal-breast tissues is 0: the remaining seven classes of tissues are then considered in the analysis.

---

<sup>13</sup><http://uwcem.ece.wisc.edu/phantomRepository.html>

<sup>14</sup>Voxel dimensions are 0,5mm × 0,5mm × 0,5mm and typical phantom dimensions are (in cells) 300 × 300 × 300; each of the two vector data contains ~ 27 000 000 elements.

Tissue Type	Media Number
Immersion medium	-1
Skin	-2
Muscle	-4
Fibroconnective/glandular-1	1.1
Fibroconnective/glandular-2	1.2
Fibroconnective/glandular-3	1.3
Transitional	2
Fatty-1	3.1
Fatty-2	3.2
Fatty-3	3.3

To take into account statistical variability, each of the normal-breast tissues is assigned a region (Fig.24) comprised between two frequency-dependent Cole-Cole single-pole curves<sup>15</sup>, which serve as upper and lower bounds. In total, eight curves are used to enclose the seven types of normal-breast tissues. To obtain the set of Debye parameters for a given voxel, characterizing its frequency-dependent behaviour, a weighted average of the data is done

$$\begin{aligned}
\varepsilon_{\infty}^i(m_i) &= p_i * \varepsilon_{\infty}^{upper}(m_i) + (1 - p_i) * \varepsilon_{\infty}^{lower}(m_i) \\
\Delta\varepsilon^i(m_i) &= p_i * \Delta\varepsilon^{upper}(m_i) + (1 - p_i) * \Delta\varepsilon^{lower}(m_i) \\
\tau^i(m_i) &= p_i * \tau^{upper}(m_i) + (1 - p_i) * \tau^{lower}(m_i) \\
\sigma^i(m_i) &= p_i * \sigma^{upper}(m_i) + (1 - p_i) * \sigma^{lower}(m_i) ,
\end{aligned}$$

where the upper and lower bound values are given by the limiting Cole-Cole curves and are functions of tissue type  $m$ , as it defines the current tissue dielectric region. By extending this calculus to every voxel of the grid, it's possible to gather all the necessary data to perform a statistical analysis and obtain the expected value and deviation for every Debye parameter of the phantom, thus expressing the wanted homogenized dielectric behaviour. Multi-phantom analysis can also be performed; in this case, Debye average parameters and deviation must be estimated for different phantom models and then averaged with proper weights.

---

<sup>15</sup>Also Debye multi-pole models can be employed[77].

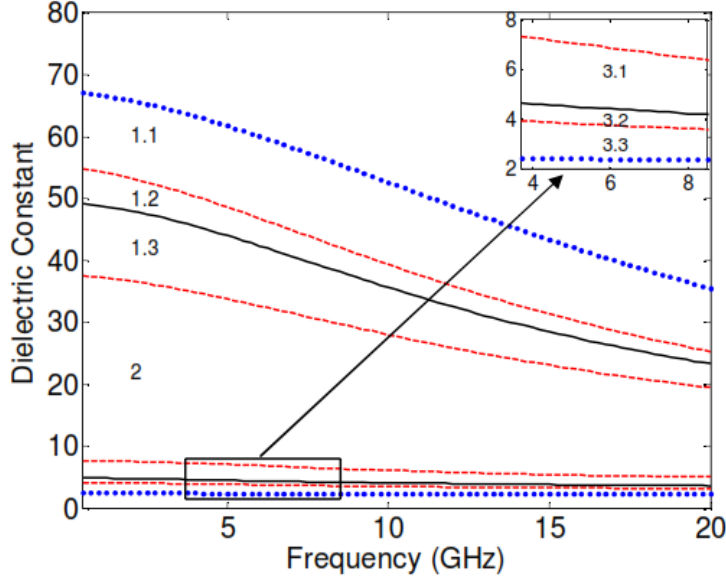


Fig.24: The dielectric properties of normal breast tissue. The seven tissue-type regions bounded by the eight Cole-Cole curves in the graph are labeled with the corresponding media numbers.

## 2.5 Numerical Assessment and Evaluation of Reconstruction Results

Once the reconstruction process is over, it's possible to perform various enhancement operations along with quantitative measurements on the resulting image, which can be thus used to evaluate the quality of the reconstruction.

When the task of object reconstruction consists in scatterer localization, as in our case, it's customary to define a set of *spatial* and *contrast metrics*, whose values can be directly calculated by defining a proper region of interest in the examined image, usually centered in the image “hotspot” (i.e. the maximum pseudospectrum value) and by employing all the pseudospectrum values included in it. In the present work, the following features will be used in order to evaluate the reconstruction output:

- **Spatial Metrics:** absolute displacement, full width at half maximum, p-value;
- **Contrast Metrics:** signal to clutter ratio, signal to clutter mean ratio.

### 2.5.1 Spatial Metrics

The TR-MUSIC algorithm makes source localization correspond to the maximum pseudospectrum value. We recall that this maximal value, since it's given by a Dirac delta

function, has theoretically value of infinite, while in a real reconstruction it takes a finite value corresponding to the maximal correlation ( $\cos \eta \simeq 1$ ) between the test and signal vectors.

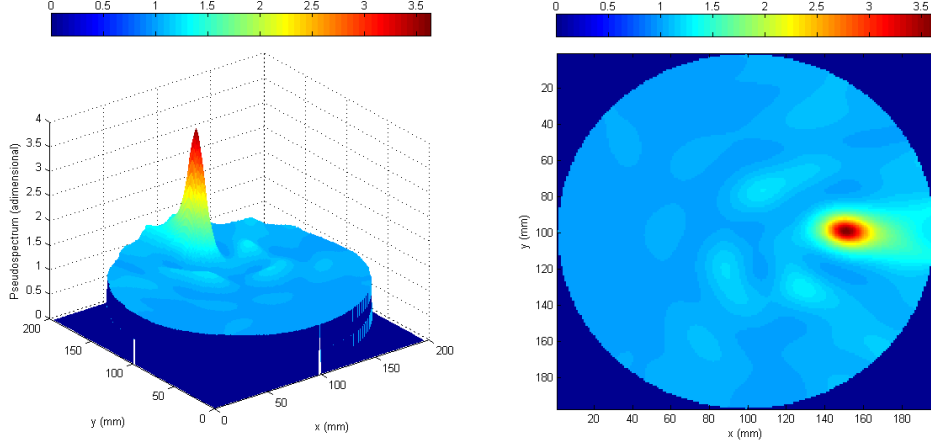


Fig.25: *Graphical visualization methods for a bidimensional pseudospectrum: three-dimensional surface view (left) and transverse plane image (right).*

Since the spread curve is usually not symmetrical with respect to the maximum value (Fig.25), source detection cannot be confidently associated to the maximum position; we estimate it as the centroid of the PSF (point spread function) curve<sup>16</sup> from half maximum (HF). After we have the curve cut from half maximum, we perform the PCA on the whole half-to-maximum pseudospectrum data which is present in a proper ROI centered in the maximum.

The principal component analysis method, given a data-set with centroid  $\boldsymbol{\mu}$ , assigns to it a new coordinate system whose axes are the eigenvectors  $\mathbf{u}_i$  of the covariance matrix  $\mathcal{C}$ , and represent the principal directions of shape variation (i.e. maximal variance); the number of axes is two for 2D data, three in case of 3D data.

Geometrically, the eigenvectors  $\mathbf{u}_i$  define the ellipsoid that best encloses the given data-set (Fig.26), and the corresponding principal semi-axes lengths are given from the *singular values*  $\sigma_i = \sqrt{\lambda_i}$ , which can be obtained from the eigenanalysis of the covariance matrix,

$$\mathcal{C}\mathbf{u}_i = \lambda_i\mathbf{u}_i .$$

The PCA eigenvalues, representing the data spread in the direction of the eigenvectors, are used to estimate the FWHM<sup>17</sup> of the PSF, which is a measure of system resolution:

$$\text{FWHM}_i = 2\alpha\sqrt{\lambda_i} . \quad (2.12)$$

<sup>16</sup>In 2D pseudospectrum, PSF is a surface curve.

<sup>17</sup>The number of eigen-widths depends from the problem dimensionality  $N$ .

The parameter  $\alpha$  is used to scale the confidence interval (i.e. the ellipsoid size); a choice of  $\alpha = 1.96$  represents a 95% confidence interval.

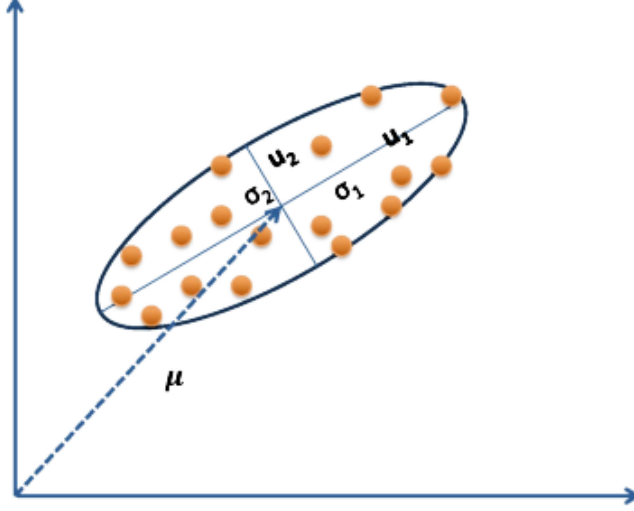


Fig.26: *Example of a 2D data-set oriented along the PCA coordinate system axes.*

From the unidimensional  $N$ -resolutions one can calculate the image average resolution

$$\text{AR} = \frac{\sum_{i=1}^N \text{FWHM}_i}{N} , \quad (2.13)$$

which in fact expresses the degree of resolution averaged over  $N$  dimensions[78].

The net error in localizing the object position is given by the distance between the actual source location  $\mathbf{X}_{\text{source}}$  and the half maximum data centroid  $\boldsymbol{\mu}$  and is called absolute displacement value:

$$\text{AD} = \|\mathbf{X}_{\text{source}} - \boldsymbol{\mu}\| . \quad (2.14)$$

The last quantity that was adopted in order to test the significance level (5%) of reconstruction and assess the detection likelihood is the  $p$ -value,

$$p\text{-val} = [1 - F(\mathbf{X}, \boldsymbol{\mu}, \boldsymbol{\Sigma})] , \quad (2.15)$$

where  $F$  denotes the multivariate normal *cumulative distribution function* (CDF). The

*probability density function* (PDF) of the 3-d multivariate normal distribution is given by

$$f(\mathbf{X}, \boldsymbol{\mu}, \boldsymbol{\Sigma}) = \frac{1}{\sqrt{|\boldsymbol{\Sigma}|} 2\pi^3} e^{-\frac{1}{2}(\mathbf{X}-\boldsymbol{\mu})\boldsymbol{\Sigma}^{-1}(\mathbf{X}-\boldsymbol{\mu})^T}.$$

After calculus,  $p$ -val needs further interpretation:

- a small  $p$ -value ( $p\text{-val} \leq 0.05$ ) indicates strong evidence against the null hypothesis, so it is rejected;
- a large  $p$ -value ( $p\text{-val} > 0.05$ ) indicates weak evidence against the null hypothesis, thus fails in rejecting it;
- $p$ -values very close to the cutoff ( $p\text{-val} \sim 0.05$ ) are considered to be marginal (need attention).

## 2.5.2 Contrast Metrics

Contrast features must be employed when evaluating images in order to quantify how well or badly the object of interest (in our case, the tumor) is visually discriminated from the surrounding scenario. The SCR and SMR are used to compare, respectively, the maximum/average source response to the maximum/average clutter in the reconstructed image:

$$\text{SCR} = \frac{\max_{N_{\text{Signal}}} [P(\mathbf{r}_n)]}{\max_{N_{\text{Noise}}} [P(\mathbf{r}_n)]} \quad (2.16)$$

$$\text{SMR} = \left( \frac{\sum_{N_{\text{Signal}}} [P(\mathbf{r}_n)]}{N_{\text{Signal}}} \right) / \left( \frac{\sum_{N_{\text{Noise}}} [P(\mathbf{r}_n)]}{N_{\text{Noise}}} \right), \quad (2.17)$$

where the pseudospectrum values  $P(\mathbf{r}_n)$  are respectively calculated in the signal ( $\mathbf{r}_n \in N_{\text{Signal}}$ ) and clutter ( $\mathbf{r}_n \in N_{\text{Noise}}$ ) area.

The signal and clutter areas have been defined by means of the normal distribution standard deviation

$$\sigma = \frac{\text{FWHM}}{2\sqrt{2\ln 2}} \simeq \text{FWHM}/2.3548,$$

where the FWHM values are given by the eigen-widths(2.12) associated to the ellipsoidal neighbourhood of the data centroid  $\boldsymbol{\mu}$  and, since the ellipsoid principal semi-axes lengths are functions of the PCA eigenvalues  $\lambda_i$ , they depend on the PSF resolution. The signal is thus represented by an ellipsoid centered in  $\boldsymbol{\mu}$  with semi-axes of length equal to  $3\sigma$ ,



while clutter is a hollow ellipsoid centered in  $\boldsymbol{\mu}$  of semi-axes lengths equal to  $6\sigma$  and cavity dimensions given by the signal ellipsoid:

$$a^{Signal} \leq 3 \cdot \sigma, \quad 3 \cdot \sigma < a^{Noise} < 6 \cdot \sigma.$$

In order to assess a high-quality detection, we're interested in both having a well resolved and localized target as well as a clearly distinguishable one.

### 2.5.3 Uncertainty of Estimated Values

TR-MUSIC reconstruction algorithm performs target detection and metrics computation in a *deterministic* way, for a given data-set of recorded signal at a fixed working-frequency. Nevertheless, several *random* factors are to disrupt signal-data: in a natural way, during real-life laboratory acquisitions, or by artificial inclusion, through the addition of statistical noise on the data. This way, a pair of reconstruction processes for the same data-set, acquired at given frequency  $\nu$ , are likely to provide images and numerical values differing from each other. In order to account the statistical variability associated to numerical output, a common approach is to reconstruct several times the image at a given frequency  $\nu$  and perform the statistical analysis on the output metrics  $m(\nu)$ , obtaining

$$\bar{m}(\nu) = \frac{1}{N_{m(\nu)}} \sum_{i=1}^{N_{m(\nu)}} m_i(\nu), \quad se_{m(\nu)} = \frac{\sigma_{m(\nu)}}{\sqrt{N_{m(\nu)}}}, \quad (2.18)$$

where  $\bar{m}(\nu)$  and  $se_{m(\nu)}$  are respectively the mean value and the standard error associated to the metrics values distribution, which tends to a normal distribution for an increasing number of measures.

Due to the computational effort required in order to reconstruct 3D-pseudospectrum, it wasn't possible to opt for such a strategy in the present work, requiring a prohibitive amount of time in order to reconstruct the same volume several times per frequency and thus derive the uncertainty estimates. We availed ourselves of the statistical analysis and error estimates performed by Pareo[79] and Grandi[71], which were performed for 2D virtual models at varying frequency and scenario conditions, and thus exploited the relative error estimates  $E_r[m(\nu)]$  to address metrics uncertainty for the simulated case. In the experimental scenario, instead, we adopted Nanetti[80] error estimates, derived from the 2D-imaging for different types of real-phantoms at the microwave laboratory. Due to the complete lack of information on vertical-dimension metrics, though, in a conservative approach we forced the relative error on vertical resolution  $E_r[R_z]$  to be given by the maximum between horizontal resolutions ( $R_x, R_y$ ) relative error estimates:

$$E_r[R_z] = \max(E_r[R_x], E_r[R_y]).$$

## Chapter 3

# Image Reconstruction and Source Detection

In this section we address the problem of detecting small spherical scatterers located inside a cylindrical and homogeneous imaging domain by irradiating this last with microwave radiation and collecting the scattered field data with a multi-monostatic/multifrequency antenna configuration: we shall then exploit a linear-inversion, TR-MUSIC reconstruction algorithm to obtain the pseudospectrum image from antenna signal measurements. While doing so, we shall treat the dielectric sphere, representing diseased tissue, in the approximation of point-like scatterer, for which it's required that the scatterer linear dimensions are inferior to one incident radiation wavelength.

Frequency	Wavelength
1.5 GHz	20 cm
2.0 GHz	15 cm
2.5 GHz	12 cm
3.0 GHz	10 cm

In order to obtain qualitative information on the distribution of the scatterers inside the domain, a single-scattering model is employed (i.e. multiple scattering is neglected) and point-source locations are described as the support of  $\delta$ -functions.

In first place, the detection and localization of the source is performed starting from synthetic-data, produced with the aid of a virtually-generated phantom in the COMSOL Multiphysics workspace; an essential review of the simulated phantom properties and generating software is presented. Then, a multiple-signal-classification reconstruction algorithm, funded on the purpose of a 3D-Green's scalar propagator for the Hertzian dipole, is described and its main features are characterized. Finally, we evaluate the performance of the 3D-linear-inversion reconstruction algorithm at varying conditions of the imaged scenario; these results are visually and quantitatively compared to the ones of a standard imaging method based on the 2D reconstruction of multiple tomographic

slices, which are taken at different scene heights and allow volumetric data reconstruction by exploiting interpolation methods.

## 3.1 Synthetic Data Collection

The use of synthetic data is a good way to start off the characterization of the reconstruction algorithm in use: making use of a virtual breast-phantom in a software-created environment makes possible to vary at our own will the set of crucial parameters from which scattering depends, and it also lets us focus in an easier way on the major sources of uncertainty during reconstruction. Widening the synthetic-data results to real-problems ones, in terms of expected performance, is in fact a critical aspect, which requires accurate analysis and further evaluation of the former. It should also be kept in mind that numerical simulations imply the use of computationally intensive forward solvers: even if synthetic-data generation is potentially unlimited, in terms of model complexity and features variability (e.g. geometry, physical properties), prompt availability of data is constrained to real hardware and software processing time, suggesting that a proper, focused use of them is done. With this in mind, the preliminary study of breast dielectric properties and microwaves interactions in biological matter can help in tailoring simple, useful models in order to highlight significant aspects of the reconstruction.

In the present work, computer simulations are carried out with the COMSOL Multi-physics software, which is a finite-element-analysis (FEA)<sup>1</sup> solver.

### 3.1.1 Finite-Element-Method

FEA is a numerical technique aimed at finding approximate solutions to boundary value problems for partial differential equations. A large, complex problem can in fact be divided into smaller, simpler parts (i.e. finite elements) so that the physical behaviour of each individual piece can be described in terms of simple equations. These equations, modelling the finite elements, can then be assembled into an arbitrarily large system of equations, used to model the entire problem; FEM then uses *variational methods* (e.g. the Galerkin method) from the calculus of variations to approximate a solution by minimizing an associated error function.

In applying FEA, the complex, addressed problem is usually a physical system with underlying physics such as the partial differential equations or integral equations, and the divided small elements of the complex problem represent different areas in the physical system. The process of dividing the complex problem into small elements, known as discretization, is usually performed by grid generation techniques, which in practice create

---

<sup>1</sup>FEA is sometimes referred as FEM, and viceversa.

a polygonal (2D) or polyhedral (3D) mesh that approximates the geometric domain<sup>2</sup>; as a result, the continuum model is transformed into a system with a finite number of degrees of freedom.

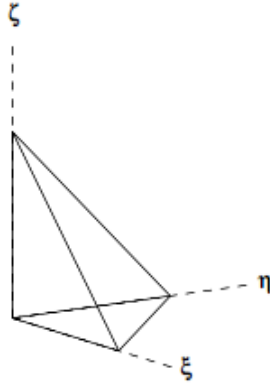


Fig.27: *The reference, four-nodes linear tetrahedron, characterized by linear polynomials shape functions.*

A *discretization strategy* consists of various steps:

- Creation of finite element meshes;
- Definition of basis or shape functions on reference elements;
- Mapping of reference elements onto the elements of the mesh.

FEM also comprises a *numerical solution algorithm*, that can be a direct or iterative solver, which should be designed in order to exploit the sparsity of matrices that depend on the choices of variational formulation and discretization strategy. The corresponding finite element solution is then evaluated by proper *postprocessing procedures* which also feature the extraction of the data of interest from the solution. In order to meet the requirements of solution verification and achieve data-validation, postprocessors need to perform a sensitivity analysis, which provides for a-posteriori error estimation in terms of the quantities of interest: when the errors of approximation are larger than what is considered acceptable, the discretization has to be changed either by an automated adaptive process or by action of the analyst.

### 3.1.2 Virtual Breast Phantom System

The RF Module of COMSOL Multiphysics simulation software has been used to solve the EFIE for the *direct* scattering problem, in frequency domain, for a virtual 3D model

---

<sup>2</sup>Three-dimensional meshes created for finite element analysis need to consist of tetrahedra, pyramids, prisms or hexahedra.

of the breast illuminated by a dipole antenna.

The main model (Fig.28) is made up of five sub-elements, each one characterized by a specific geometry and physical properties: breast interior (cylinder), skin layer (hollow cylinder containing the breast cylinder), scattering source (small sphere), dipole antenna (small cylinder) and coupling medium (covers remaining space).

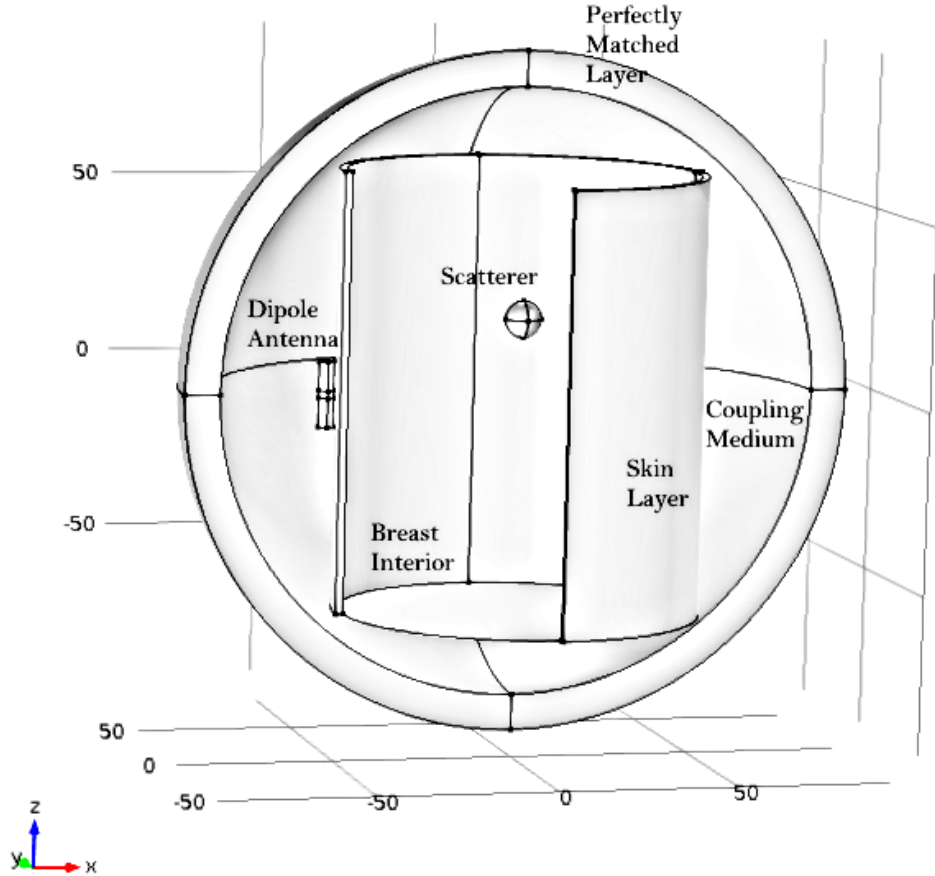


Fig.28: *Sight of the main elements in the virtual breast phantom coordinate system.*

The breast model is enclosed in a hollow sphere called *perfectly matched layer* (PML), that is an artificial absorbing layer used for wave equations to truncate the numerical methods computational region, which would otherwise present open boundaries. Thus, PML defines the geometrical limits of the whole investigation domain: in the present case, though, our interest is limited to the space-region which can be occupied by the scatterer, so we will simply refer to the breast cylinder region as *imaging domain*.

Here follows a list which summarizes the general properties of the model; some of them are changed on purpose during the work, as will be later specified. The dielectric properties of breast interior and tumor are expressed in the form of realistic first-order Debye

model (1.1) parameters  $[\varepsilon_\infty, \varepsilon_s, \tau(\text{ps}), \sigma(\text{S/m})]$ ; as it is employed in other studies[45], the assumed dielectric contrast between malignant and normal breast tissue is approximately (5:1). The *total* breast radius, which accounts for both the breast interior radius and skin thickness, is  $r^{(s)} = 50$  mm. By default, we work with *homogeneous* interior.

– **Breast interior**

Breast radius:  $r^{(b)} = 48$  mm

Breast height:  $l^{(b)} = 12$  cm

Homogeneous dielectric properties:  $[\varepsilon_\infty^{(b)}, \varepsilon_s^{(b)}, \tau^{(b)}, \sigma^{(b)}] = [7, 10, 7, 0.15]$

– **Skin layer**

Skin thickness:  $t^{(s)} = r^{(s)} - r^{(b)} = 2$  mm

Fixed relative permittivity:  $\varepsilon_r^{(s)} = 36$

Fixed conductivity:  $\sigma^{(s)} = 4$  S/m

– **Tumor**

Scatterer radius:  $r^{(t)} = 5$  mm

Homogeneous dielectric properties:  $[\varepsilon_\infty^{(t)}, \varepsilon_s^{(t)}, \tau^{(t)}, \sigma^{(t)}] = [4, 54, 7, 0.7]$

– **Dipole antenna**

Antenna radius:  $r^{(a)} = 2$  mm

Breast-antenna distance:  $d = 2$  mm

Gap size:  $s^{(a)} = 2$  mm

– **Coupling medium**

Fixed relative permittivity:  $\varepsilon_r^{(m)} = 10$

Fixed conductivity:  $\sigma^{(m)} = 0.05$  S/m

To obtain signal measurements, the antenna is kept at a distance of 54 mm from the breast cylinder rotation-axis, and is rotated around it by equal, discrete angular steps ( $\Delta\phi = 18^\circ$ ), for a total of 20 positions  $[\mathbf{R}_{pos} = (\mathbf{R}_1, \mathbf{R}_2, \dots, \mathbf{R}_{20})]$  in the transverse plane<sup>3</sup>; in each position, the transceiver emits and receives back a signal(2.11), giving rise to the monostatic signal vector  $\mathbf{S}(\omega) = [S_{11}(\omega), S_{22}(\omega), \dots, S_{2020}(\omega)]$ , where  $\omega$  is the working frequency. It's possible to perform this operation and acquire signal at a specific elevation respect to the system zero-level, that is, for present imaging purposes, at any  $z$  between the inferior and superior vertical limits of the breast<sup>4</sup>. By defining  $h^{(a)}$  as the vertical distance between antenna position  $\mathbf{R}_l$  and transverse plane, we can rewrite the

<sup>3</sup>Transverse plane is referred to as the horizontal-plane passing through the domain origin.

<sup>4</sup> $z \in [-60, 60]$  mm.

measured signal vector as a collection of individual signals taken at a given frequency  $\omega$  and elevation  $h^{(a)}$ :

$$\mathbf{S}(\omega, h^{(a)}) = [S_{11}(\omega, h^{(a)}), S_{22}(\omega, h^{(a)}), \dots, S_{2020}(\omega, h^{(a)})] . \quad (3.1)$$

Lastly, the model finite-element-analysis is based on a tetrahedral discretization grid (Fig.29), where each element in the domain presents a different mesh-size which depends on the working frequency and relative permittivity of the object:

$$D_{Mesh} \leq \frac{\lambda_0 / \sqrt{\epsilon_r}}{5} ,$$

where  $\lambda_0$  is the radiation wavelength in vacuum associated to  $\omega$ .

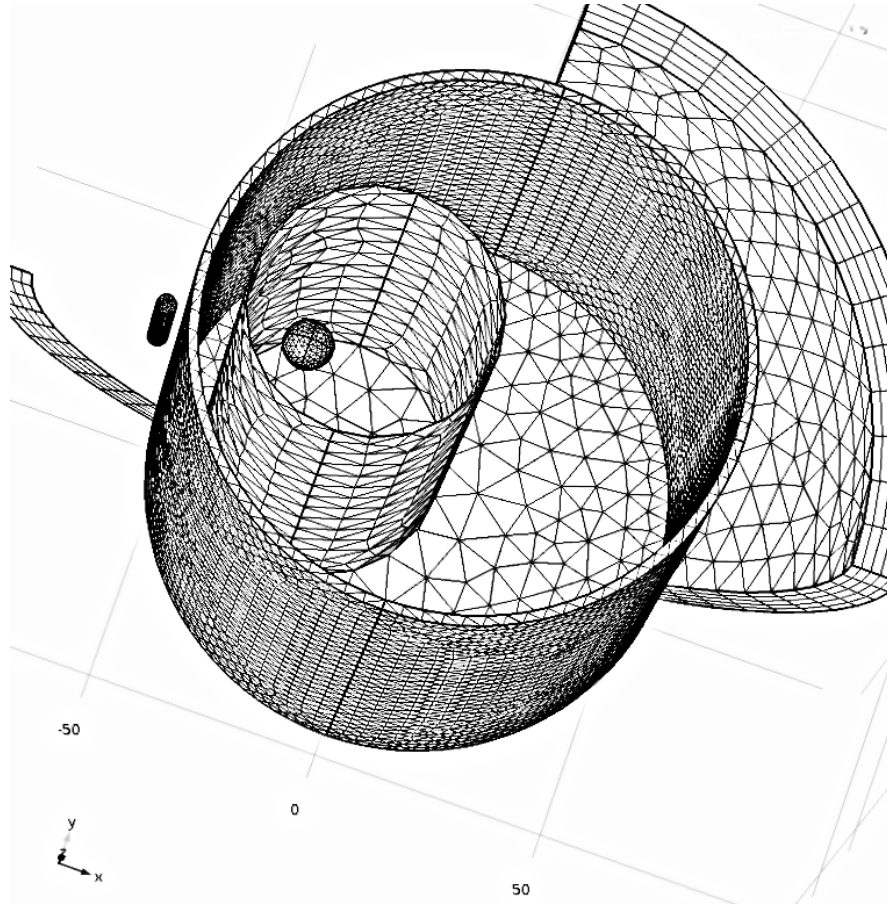


Fig.29: *Tetrahedral discretization grid view. A lesser, eccentric cylinder was added to the basic model to simulate the presence of a fibroglandular region surrounding the tumor.*

Optimal mesh-size calculation, surface-blending and mesh-resizing (occurs when changing operational parameters) tasks are automatically performed by the simulation software before the start of acquisition process.

## 3.2 Multi-Elevation Reconstruction

After the model is implemented, RF simulations are run to acquire scattered-field data, and the corresponding signal-vector  $\mathbf{S}(\omega, h^{(a)})$  can thus be exploited in order to reconstruct image values: the TR-MUSIC algorithm is capable of estimating a pseudospectrum value  $P(\mathbf{R}_p, \omega)$  for any specified test-point location  $\mathbf{R}_p$  in the imaging domain(2.5).

The signal vector, acquired at a precise elevation  $h^{(a)}$ , can in fact be used along with the 2D-Green's propagator(2.6) to calculate all the pseudospectrum values corresponding to test-points in the antenna plane ( $z_p = h^{(a)}$ ), or with the 3D-Green's scalar propagator for the infinitesimal dipole(2.7), by which also the out-of-antenna-plane values can be obtained through the evaluation of correlation between signal and monostatic response for whichever point in the domain. In this way, the 3D-propagator seems much more appealing than its 2D counterpart because it is capable of calculating and reconstructing the whole imaging domain pseudospectrum with a single vector of acquisitions  $\mathbf{S}(\omega, h^{(a)})$ ; in the 2D propagator case, instead, to reconstruct a portion of volume it's theoretically necessary to collect a signal-vector for every elevation covering the volume of interest ( $\mathbf{S}(\omega, h_0^{(a)}), \mathbf{S}(\omega, h_1^{(a)}), \dots, \mathbf{S}(\omega, h_n^{(a)})$ ) and reconstruct volumetric image by superposition of pseudospectrum slices. In practice, as we will see soon, the 3D-propagator volume reconstruction at a single elevation presents a series of major disadvantages, suggesting that a proper multi-elevation method should be adopted either way.

### 3.2.1 Mono-Elevation Reconstruction

In the preliminar part of our work, we have tested the actual potential of the 3D-reconstruction algorithm by exploiting a series of mono-elevation vector-signals  $\mathbf{S}(\omega, h^{(a)})$ , acquired by illuminating the previously presented virtual-phantom with a microwave radiation of 2GHz frequency at different antenna heights. During this test, scatterer was positioned slightly above the transverse plane,

$$\mathbf{r}_{scatt} = [40, 0, 20] \text{ mm ,}$$

where the spatial coordinates  $[x, y, z]$  are expressed respect to the domain origin. Data have thus been acquired at different antenna heights

Elevation	$h_0^{(a)}$	$h_1^{(a)}$	$h_2^{(a)}$	$h_3^{(a)}$	$h_4^{(a)}$	$h_5^{(a)}$	$h_6^{(a)}$	$h_7^{(a)}$	$h_8^{(a)}$	$h_9^{(a)}$
Value (mm)	-20	0	10	15	17.5	20	22.5	25	30	40

and, for each row of the signal matrix

$$\mathbf{S}(2\text{GHz}) = \begin{bmatrix} \mathbf{S}(2\text{GHz}, h_0^{(a)}) \\ \mathbf{S}(2\text{GHz}, h_1^{(a)}) \\ \vdots \\ \mathbf{S}(2\text{GHz}, h_9^{(a)}) \end{bmatrix} = \begin{bmatrix} \mathbf{S}_0 \\ \mathbf{S}_1 \\ \vdots \\ \mathbf{S}_9 \end{bmatrix} ,$$



a mono-elevation volumetric image of the breast have been reconstructed with 3D-propagator. The imaging volume extension and reconstruction step, whose choice drastically influences the algorithm elaboration time, must be manually set by the user: we chose to reconstruct pseudospectrum in the entire breast vertical-range  $z \in [-60, 60]$ mm and extended horizontal range<sup>5</sup>  $x, y \in [-49, 49]$ mm, with a fixed test-step of 0.5mm<sup>6</sup>.

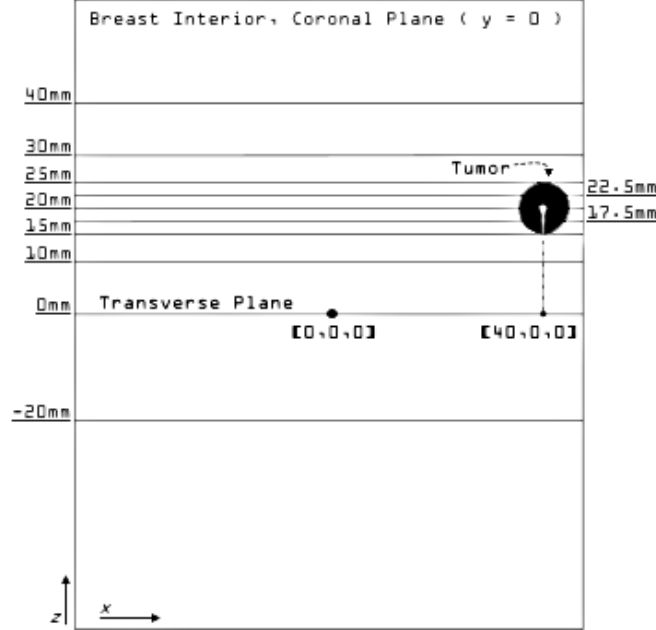


Fig.30: *Coronal slice of the breast and tumor representation; acquisition planes are marked at the corresponding antenna elevations. Objects coordinates are expressed in millimeters.*

Before attempting reconstruction, the signal matrix rows are filtered with the average subtraction filter(2.10),

$$\mathbf{S}_{filtered} = \begin{bmatrix} \mathbf{S}_{filtered}(h_0^{(a)}) \\ \mathbf{S}_{filtered}(h_1^{(a)}) \\ \vdots \\ \mathbf{S}_{filtered}(h_9^{(a)}) \end{bmatrix} = \begin{bmatrix} \mathbf{S}_{recorded}(h_0^{(a)}) - \frac{1}{20} \sum_{i=1}^{20} S_{recorded}^i(h_0^{(a)}) \\ \mathbf{S}_{recorded}(h_1^{(a)}) - \frac{1}{20} \sum_{i=1}^{20} S_{recorded}^i(h_1^{(a)}) \\ \vdots \\ \mathbf{S}_{recorded}(h_9^{(a)}) - \frac{1}{20} \sum_{i=1}^{20} S_{recorded}^i(h_9^{(a)}) \end{bmatrix},$$

where signal value mean is calculated separately respect to every set of 20 acquisitions at the same height. Finally, a white gaussian noise of 10dB is added to filtered signal in order to simulate a more realistic environment and check algorithm robustness.

<sup>5</sup>We added 1 millimeter of skin to the interior breast radius.

<sup>6</sup>Image voxels are cubes of side 0.5 mm and volume  $(0.5 \times 0.5 \times 0.5)\text{mm}^3$

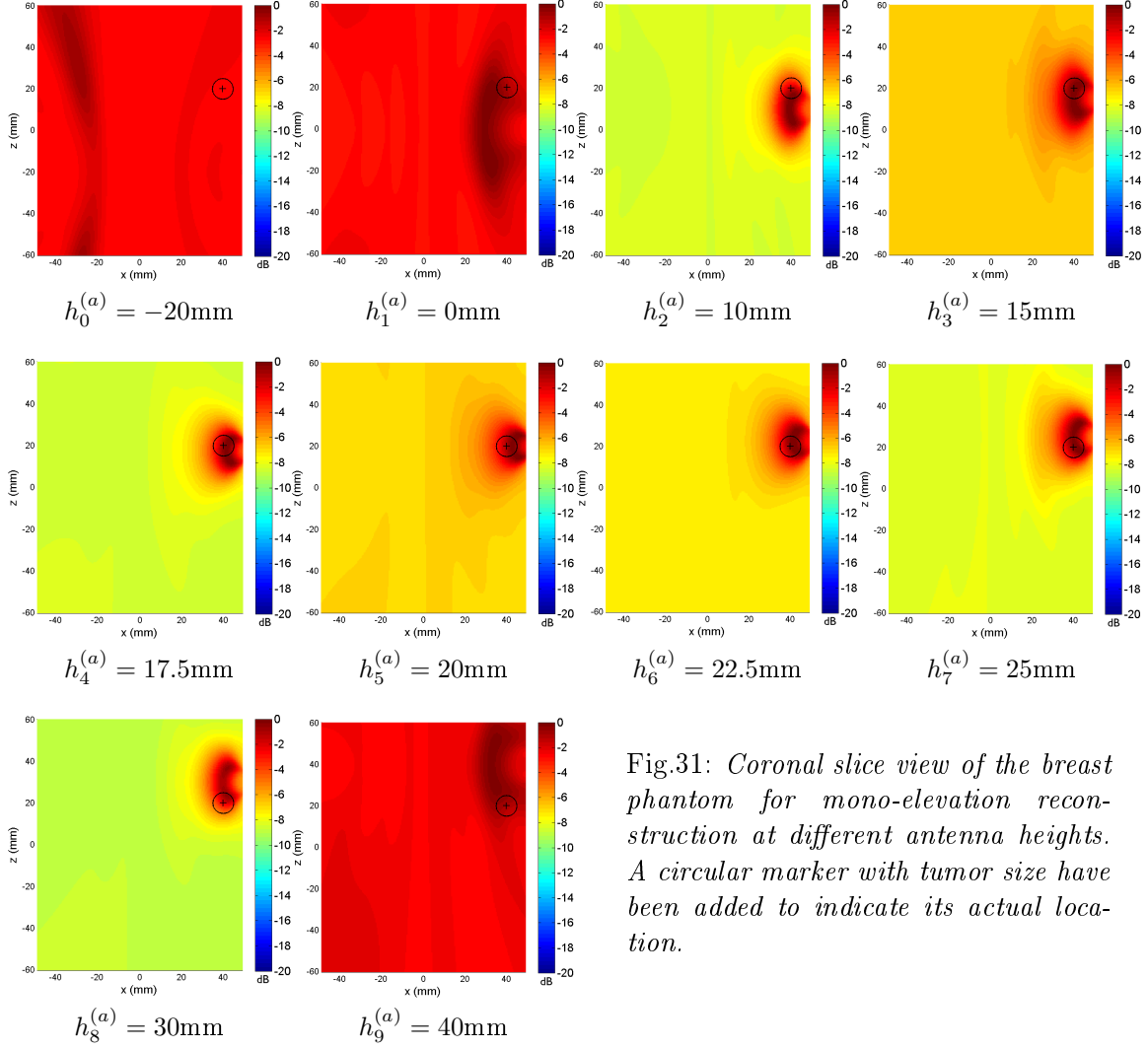


Fig.31: *Coronal slice view of the breast phantom for mono-elevation reconstruction at different antenna heights. A circular marker with tumor size have been added to indicate its actual location.*

Visual results show that, for the mono-elevation reconstruction, two major problems arise. The first issue directly derives from the particular symmetry of the dipole-antenna radiation pattern<sup>7</sup>: test-points with specular positions respect to horizontal antenna-plane present, respectively for each antenna and its relative axis, same radial distance  $r$  and polar angle  $\theta$ , and thus feel an equal radiated-field intensity  $\mathbf{E}(\mathbf{r})$  by each antenna. Since the employed 3D-propagator explicitly depends on  $E_z$ , this results in the formation of a *mirrored pseudospectrum* about antennas feed plane. In second place, it is clearly visible how image contrast is enhanced by getting the antenna closer to the source position and, viceversa, it decreases when we move it farther: after a certain ver-

<sup>7</sup>Because of the intrinsic symmetry of dipoles, relative to the  $x$ - $y$  plane containing the antenna feed point, resultant radiation is rotationally symmetric about  $z$ -axis or  $\phi$ -independent.

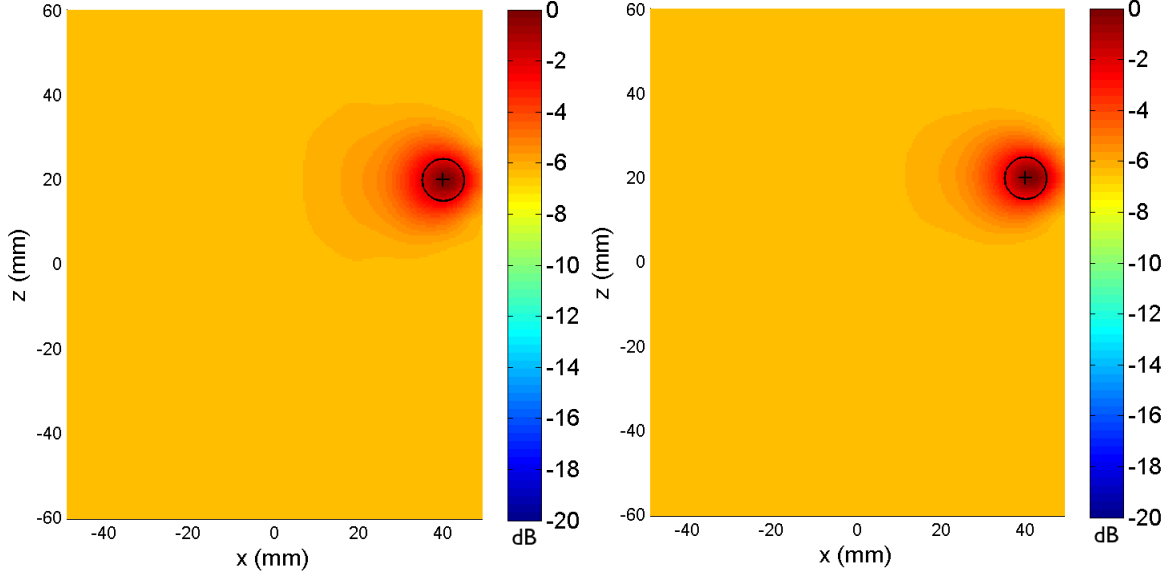


Fig.32: Coronal slice view of the breast phantom for multi-elevation reconstruction at 9 (left) and 10 (right) antenna elevations. In the left image, signal  $\mathcal{S}(h_0^{(a)})$  was not included in reconstruction.

tical distance ( $\sim 20\text{mm}$ ), image degrades quickly and, if the antenna is too distant, the weak signal mainly contributes to the rise of artefacts ( $h_0^{(a)} = -20\text{mm}$ ). This behaviour is likely to be given by the dependence of  $E_z$  on the  $\sin^2 \theta$  term, which further becomes a  $\sin^4 \theta$  dependence when evaluating the correlation term value, and can be translated in *limited visibility* by the antenna respect to vertically-far objects.

Mirroring, which shows itself as a typical effect of the mono-elevation approach, is a problem which must be worked out because it not only causes noticeable blurring, but also delocalizes the hotspot region in a major way. Furthermore, we saw that the overall reconstruction outcome is very sensitive to the particular antenna-elevation choice which is, in a typical tumor detection scenario, not trivial.

In order to overcome the evident limits of this approach, we have focused our attentions on the realization and evaluation of a monostatic *multi-elevation* method. Such a technique is based on reconstructing the volumetric pseudospectrum with the 3D-propagator by employing the entire signal matrix  $\mathbf{S}(\omega)$  at once. Preliminar results for the present case show that this approach can be preferable to the mono-elevation one since the mirroring aberration is entirely removed (employing more than one elevation breaks the symmetry condition) and source is properly localized. It's also important to notice how multi-elevation performs robustly when weak signal information are added to reconstruction; in this case, signal vector  $\mathbf{S}_{\text{filtered}}(h_0^{(a)} = -20\text{mm})$  would mainly contribute to the rise of clutter in the image, as it can be seen in the mono-elevation case, but, since it's on average contrasted by “strong” signal (i.e. signal collected by antennas in the vicinity of the source) in multi-elevation, the information still provide some usefulness (the surrounding halo is reduced) and, principally, they don't worsen the overall result.

### 3.2.2 Multi-Elevation MUSIC Algorithm Evaluation

In order to quantitatively assess the performance of multi-elevation reconstruction algorithm, we employed a grid-like imaging strategy for the phantom: signal was collected in monostatic setup, for the usual 20 antenna positions in circular motion around the breast, every 2.5mm-step in the vertical-range  $[-25, 25]$ mm.

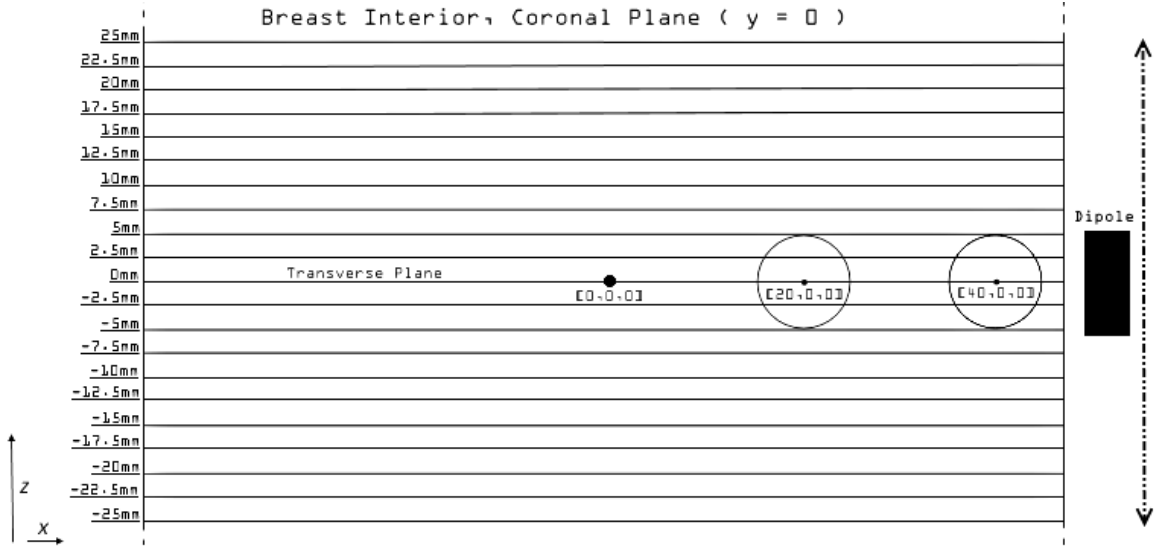


Fig.33: Coronal slice of the breast and tumor representation; grid planes are marked at the corresponding antenna elevations. Items coordinates are expressed in millimeters.

Experiment is initially conducted with the scatterer positioned on transverse plane in an outer breast position

$$\mathbf{r}_{scatt}^{ext} = [40, 0, 0] \text{ mm} ,$$

and it is then repeated by shifting the tumor in an inner location

$$\mathbf{r}_{scatt}^{int} = [20, 0, 0] \text{ mm} .$$

In order to investigate the frequency dependance of the imaging outcome, simulation was repeated for both tumor locations at four different frequencies: (1.5, 2.0, 2.5, 3.0)GHz. For every frequency and elevation

Elevation	$h_0^{(a)}$	$h_1^{(a)}$	$h_2^{(a)}$	$h_3^{(a)}$	$h_4^{(a)}$	$h_5^{(a)}$	$h_6^{(a)}$	$h_7^{(a)}$	$h_8^{(a)}$	$h_9^{(a)}$	...
Value (mm)	-25	-22.5	-20	-17.5	-15	-12.5	-10	-7.5	-5	-2.5	...
Elevation	$h_{10}^{(a)}$	$h_{11}^{(a)}$	$h_{12}^{(a)}$	$h_{13}^{(a)}$	$h_{14}^{(a)}$	$h_{15}^{(a)}$	$h_{16}^{(a)}$	$h_{17}^{(a)}$	$h_{18}^{(a)}$	$h_{19}^{(a)}$	$h_{20}^{(a)}$
Value (mm)	0	2.5	5	7.5	10	12.5	15	17.5	20	22.5	25

it's possible to collect a single row-vector of signal-data, giving rise to a total of four different signal-matrices  $\mathbf{S}(\omega)$  per experiment (i.e. tumor location); after properly filtering

each matrix-row with the usual average subtraction and adding white gaussian noise, we exploit the filtered signal matrices  $\mathbf{S}_{filtered}(\omega)$  in order to reconstruct imaging volumes in the range  $z \in [-25, 25]$ mm,  $x, y \in [-49, 49]$ mm with the usual 0.5mm test-step. To compare visual and quantitative results of the 3D-propagator, we first adopted and evaluated another volume-reconstruction method based on superposition of tomographic slices. The 2D-Hankel propagator(2.6) approach is based on reconstructing a single tomographic image for each filtered row-signal vector  $\mathbf{S}_{filtered}(\omega, h_n^{(a)})$ , for a total of  $n = 21$  elevations per frequency in the present case; missing pseudospectrum values, associated

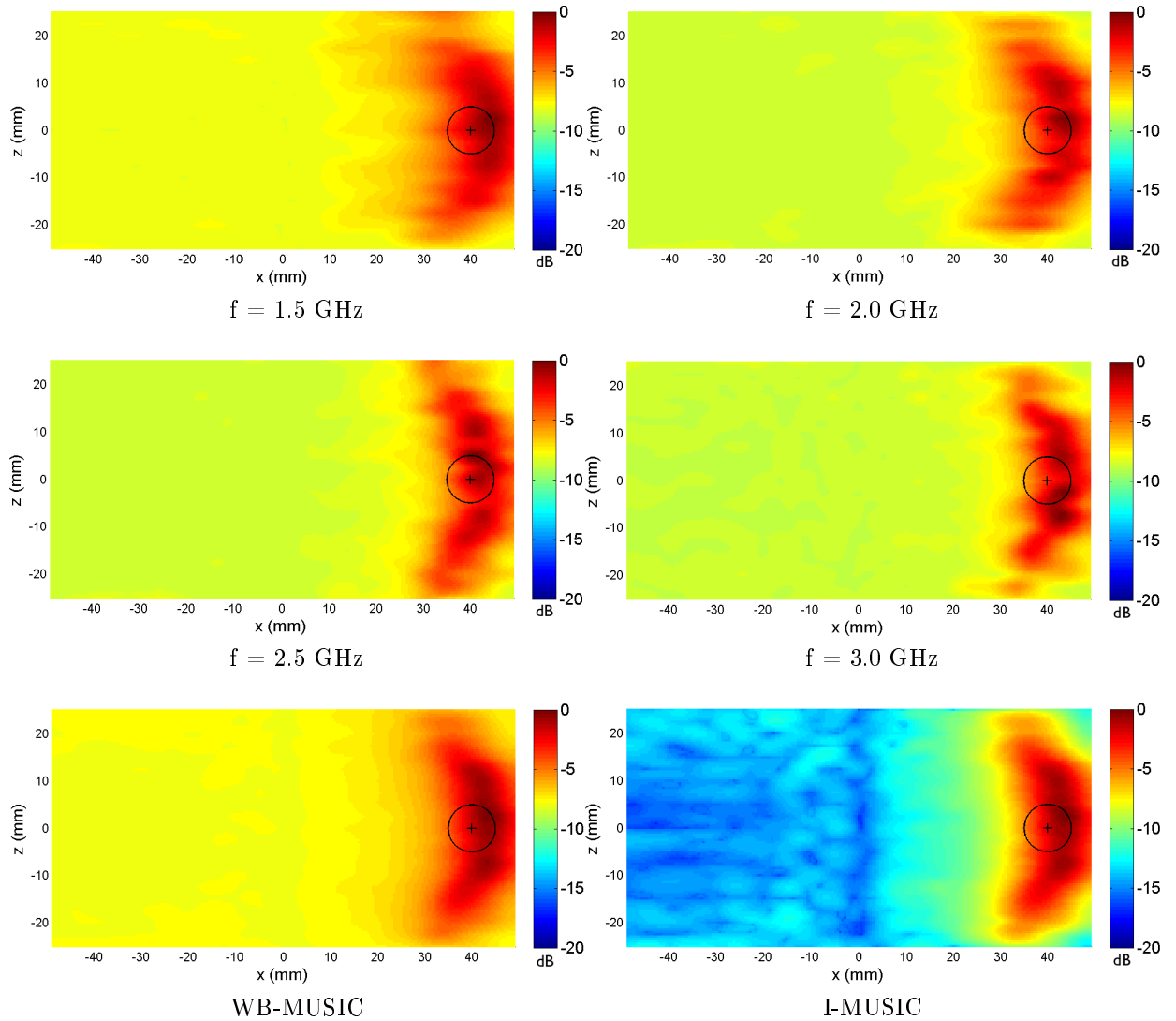


Fig.34: Coronal slice view of the breast phantom for the tomographic interpolation reconstruction method; scatterer is located in the external region (I).

to the intermediate volumes in between grid planes, are later derived by applying the cubic interpolation method to available (i.e. reconstructed) slice data, and the volumetric image is thus given by superposition of reconstructed and interpolated slices; during the present reconstruction, the interpolation grid spacing was set to 0.5mm and, since it was chosen a homogeneous 0.5mm reconstruction step for 2D-slices, the resulting image voxel is a cube of side 0.5mm (exactly as in the 3D-propagator reconstruction). After achieving “volume building” with this technique, the 3D-pseudospectra at single frequency are combined with WB-MUSIC(2.8) and I-MUSIC methods(2.9). At this

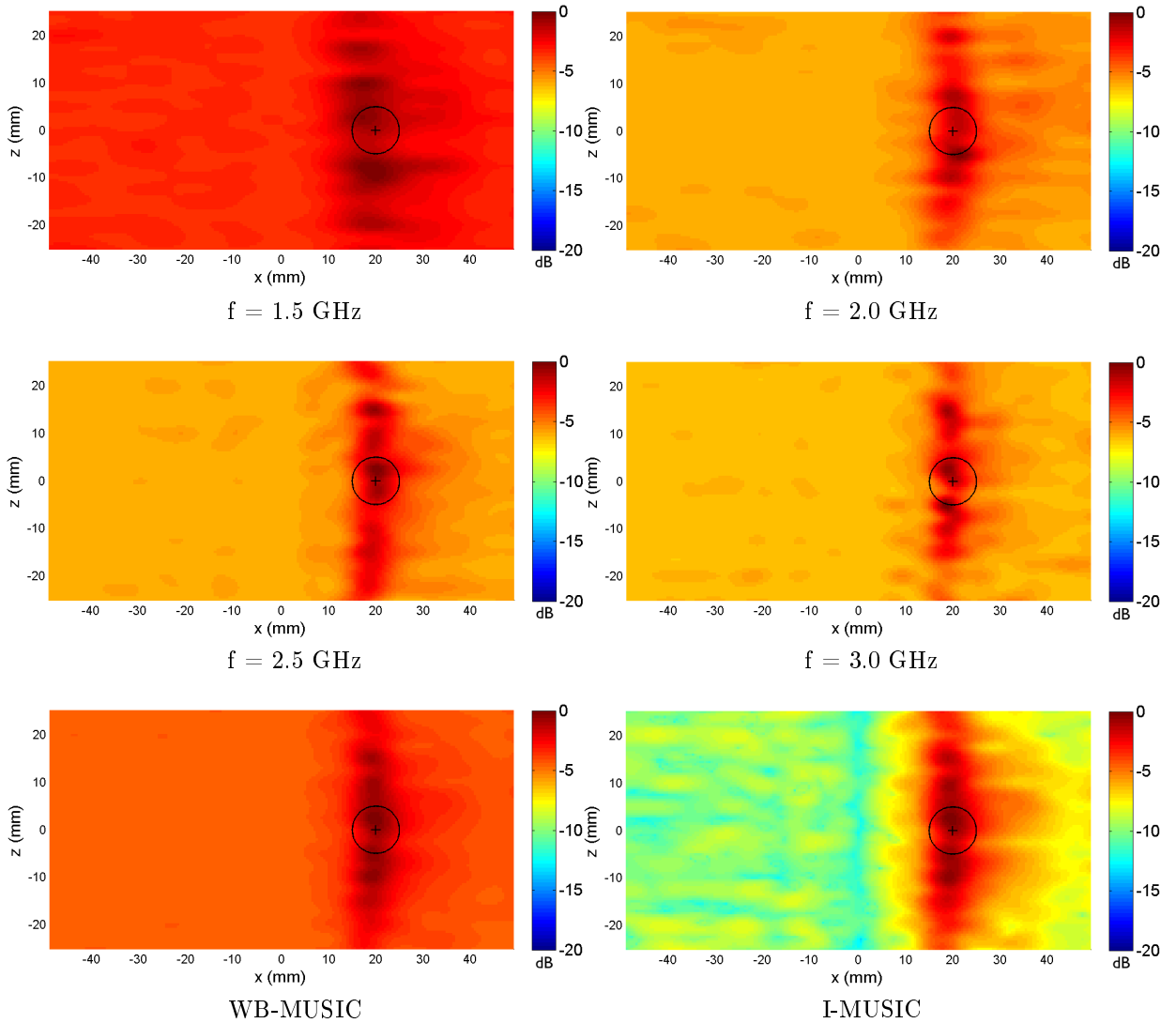


Fig.35: *Coronal slice view of the breast phantom for the tomographic interpolation reconstruction method; scatterer is located in the internal region (II).*

point, the reconstruction algorithm automatically centers a parallelepiped 3D-ROI in the maximum value of the pseudospectrum and then elaborates spatial and contrast metrics through the use of PCA on the included numerical values; we chose to set the ROI vertical dimension in order to cover the entire vertical-range of the image ( $I_z = 50\text{mm}$ ), because the spot appears visibly elongated respect to  $z$ , while the horizontal half-size was put equal to 20% of the  $x - y$  image dimension ( $I_x = I_y = 98\text{mm}$ ).

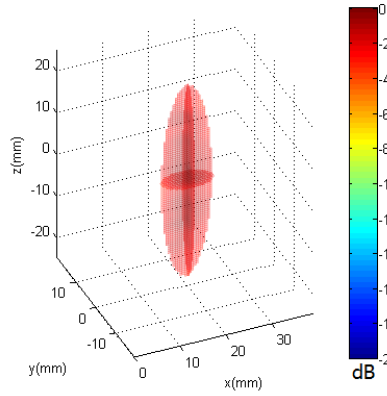


Fig.36: 3D-ROI containing the clutter-separated WB-pseudospectrum deriving from tomographical-superposition method for the internal scatterer position(II).

The following numerical values have been obtained for the external (I) and internal (II) tumor with tomographic-superposition reconstruction algorithm.

	Image Type	Spatial Metrics(mm)					Contrast Metrics(dB)		p-val
		Rx	Ry	Rz	AD	AR	SCR	SMR	
I	1.5GHz	13,7±0,9	10,3±0,5	35,5±2,3	2,7±1,4	19,8±1,2	2,8±0,6	2,4±0,3	0,85
	2.0GHz	15,7±0,6	7,6±0,3	34,5±1,3	2,6±0,8	19,1±0,7	2,6±0,3	2,5±0,3	0,84
	2.5GHz	17,1±0,9	6,0±0,3	38,1±2,0	2,0±0,6	20,0±1,0	2,9±0,2	2,3±0,2	0,85
	3.0GHz	14,7±0,4	6,7±0,1	31,0±0,9	3,1±0,9	17,1±0,7	2,5±0,1	2,7±0,1	0,84
	WB	15,2±0,4	7,5±0,2	34,5±1,0	2,7±0,8	19,0±0,6	2,8±0,1	2,5±0,1	0,84
	I	19,6±0,8	10,8±0,5	48,7±2,1	0,4±0,2	26,6±1,1	5,2±0,2	3,5±0,1	0,87
II	1.5GHz	17,6±1,1	4,8±0,3	41,4±2,7	0,5±0,3	22,6±1,4	1,3±0,3	0,9±0,1	0,87
	2.0GHz	8,9±0,3	4,5±0,1	34,4±1,3	1,0±0,3	16,2±0,6	2,9±0,3	1,7±0,2	0,85
	2.5GHz	9,1±0,5	4,2±0,2	45,0±2,3	0,4±0,1	19,2±1,0	2,7±0,2	1,8±0,1	0,86
	3.0GHz	6,7±0,2	3,2±0,1	36,0±1,1	1,8±0,5	15,3±0,4	3,3±0,1	1,7±0,1	0,78
	WB	9,5±0,3	4,9±0,1	36,8±1,1	0,5±0,2	17,1±0,5	2,3±0,1	1,4±0,1	0,85
	I	30,9±1,3	13,5±0,6	48,1±2,1	5,3±2,1	30,9±1,3	6,0±0,2	1,9±0,1	0,85

**Tab.1:** Tomographic-superposition reconstruction algorithm resulting metrics.

We can preliminarily observe that the tomographic-superposition algorithm is fairly capable of detecting the target in three-dimensions: estimated centroid location is very close to the actual tumor position, resulting in low absolute displacement (AD) values, and can be confidently accepted for the present  $p$ -value numbers. It can be noticed visually and numerically how all these reconstructions suffer from very low resolution along  $z$ -axis ( $R_z$ ), which is in most cases as low as twice the lowest horizontal resolution ( $R_x$  in this case), thus accounting for the most part of average resolution values. Absolute displacement seems to be independent from frequency choice while resolution is, on

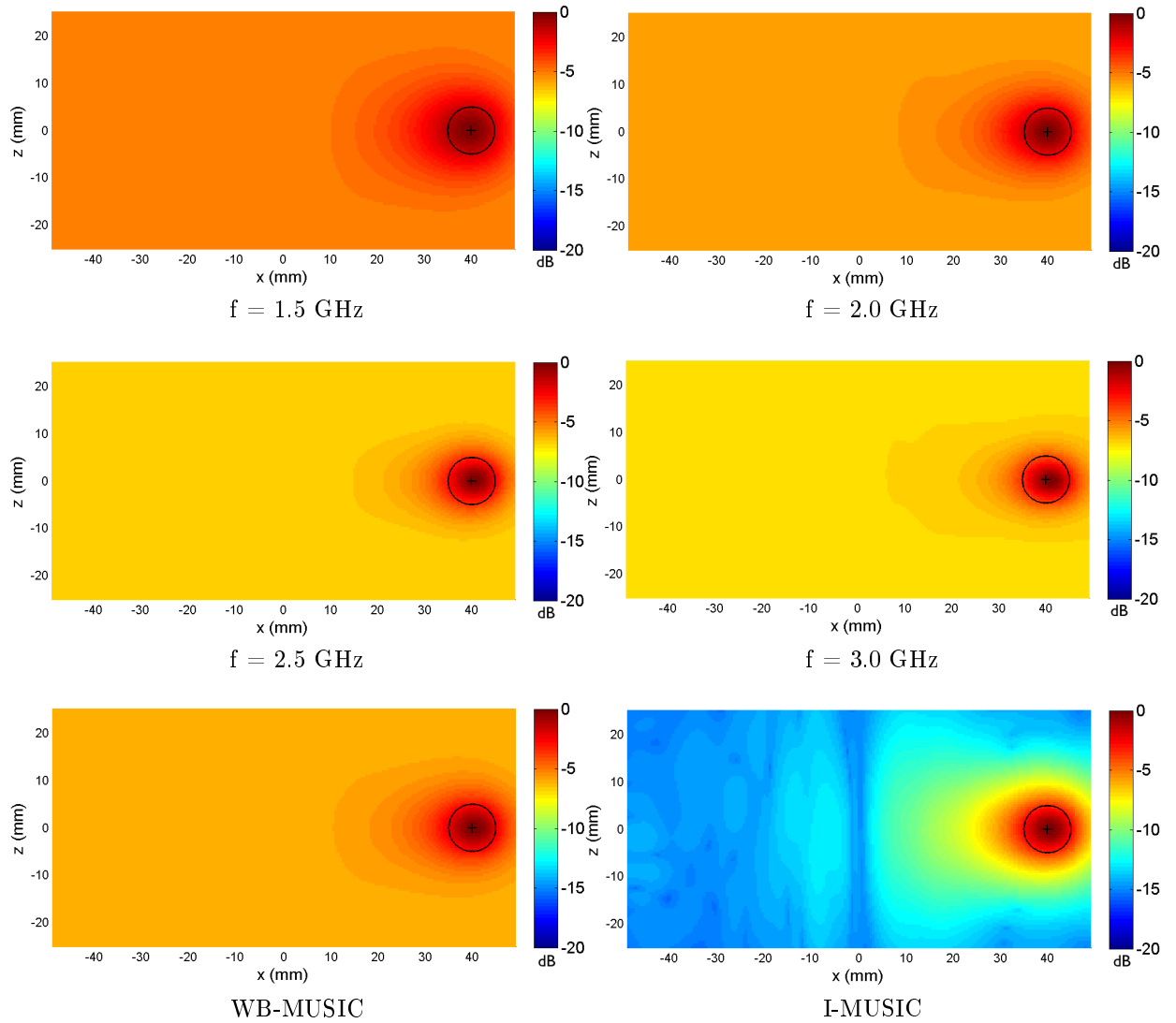


Fig.37: *Coronal slice view of the breast phantom for the multi-elevation reconstruction method; scatterer is located in the external region (I).*



average, positively influenced by working at increased frequency. Incoherent recombination methods have completely different outcomes. WB-MUSIC can be viewed as a good compromise in terms of multi-frequency resolution as it shows, on average, a better AR respect to single-frequency ones, although it doesn't offer any resolution improvement when compared to high frequency AR. I-MUSIC provides an excellent contrast enhancement both in terms of SCR and SMR but, as a major downside, it heavily worsens resolution; it should also be pointed out that contrast enhancement may bring up clutter areas as a collateral effect, and thus cause major displacement when raising clutter in

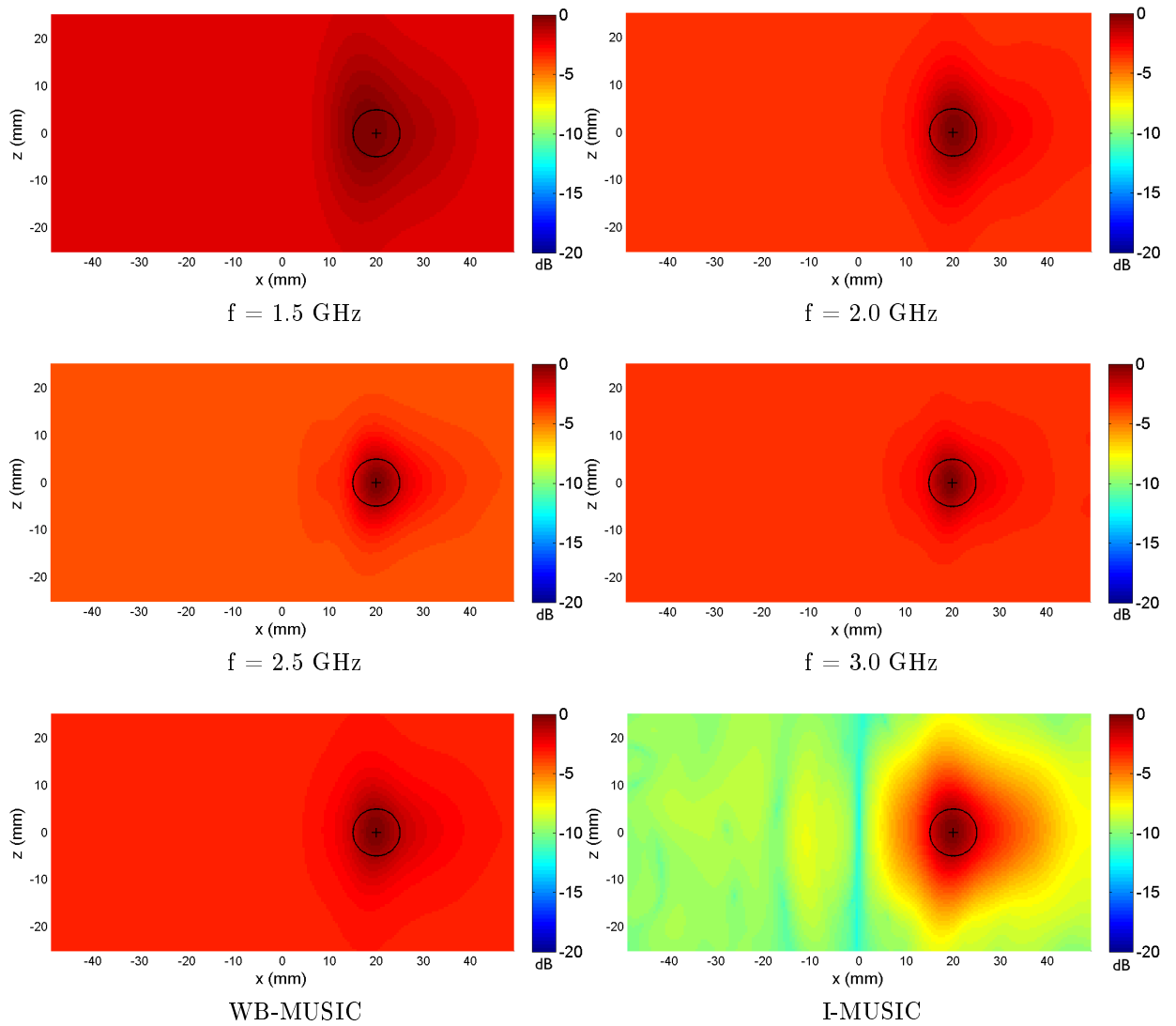


Fig.38: *Coronal slice view of the breast phantom for the multi-elevation reconstruction method; scatterer is located in the internal region (II).*

the vicinity of the source (e.g. I-MUSIC in case II). It can also be pointed out that SCR and SMR do not vary much with frequency in case I, for when antenna is close to the source also low frequency excitation produces a strong scattered signal; in case II, the deeper tumor causes weak scattered signal to be recorded when low frequency excitation is exploited, thus giving place to lower contrast values that, however, noticeably improve by increasing frequency.

By applying instead the multi-elevation reconstruction algorithm we obtained the following results for the external (I) and internal tumor (II).

	Image Type	Spatial Metrics(mm)					Contrast Metrics(dB)		p-val
		Rx	Ry	Rz	AD	AR	SCR	SMR	
I	1.5GHz	15,2±1,0	9,4±0,5	12,3±0,8	0,7±0,4	12,3±0,8	2,5±0,5	2,0±0,2	0,86
	2.0GHz	13,7±0,5	7,1±0,2	10,3±0,4	0,3±0,1	10,4±0,4	2,9±0,3	2,2±0,2	0,87
	2.5GHz	10,6±0,6	6,3±0,3	9,0±0,5	0,9±0,3	8,6±0,4	3,3±0,3	2,6±0,2	0,84
	3.0GHz	10,5±0,3	5,2±0,1	7,2±0,2	1,3±0,4	7,7±0,2	3,4±0,1	2,6±0,1	0,84
	WB	12,1±0,4	6,6±0,2	9,5±0,3	0,7±0,2	9,4±0,3	3,0±0,1	2,3±0,1	0,85
	I	24,8±1,1	12,0±0,5	17,9±0,8	1,4±0,6	18,3±0,8	6,1±0,2	4,1±0,1	0,86
II	1.5GHz	15,5±1,0	7,5±0,4	23,7±1,5	1,2±0,6	15,9±1,0	1,0±0,2	0,9±0,1	0,84
	2.0GHz	11,2±0,4	6,2±0,2	17,1±0,7	1,2±0,4	11,6±0,4	1,9±0,2	1,5±0,2	0,84
	2.5GHz	10,0±0,5	5,5±0,2	12,6±0,7	1,0±0,3	9,3±0,5	2,2±0,2	1,7±0,1	0,85
	3.0GHz	7,9±0,2	4,9±0,1	11,7±0,4	0,6±0,2	8,1±0,2	1,8±0,1	1,4±0,1	0,85
	WB	10,6±0,3	5,9±0,2	14,7±0,4	0,8±0,2	10,4±0,3	1,7±0,1	1,3±0,1	0,84
	I	32,9±1,4	20,4±0,9	26,1±1,1	4,4±1,8	25,8±1,1	5,4±0,2	2,2	0,83

**Tab.2:** *Multi-elevation reconstruction algorithm resulting metrics.*

The multi-elevation reconstruction method provides good localization capability, with low and also well supported by  $p$ -val AD values; resolution in  $z$  is particularly high when tumor is external, in which case it further proves to be better than horizontal resolution  $R_x$ , while it degrades of a consistent amount when tumor is positioned internally, since scattered signal is drastically weaker at all heights and the overall focusing diminishes. As for the tomographic-superposition algorithm case, we notice a solid increase in all resolution values by increasing frequency, while AD seems again not to be influenced by frequency choice; WB/I-MUSIC concretely offer the same results previously viewed, by respectively averaging single-frequency resolution capabilities and boosting image contrast at the price of worsened resolution and raised clutter. Finally, we notice that for both contrast indicators a slight increase in values occurs by increasing frequency, and they are again all lower in the internal tumor case.

We have then directly compared the results of different reconstruction processes.

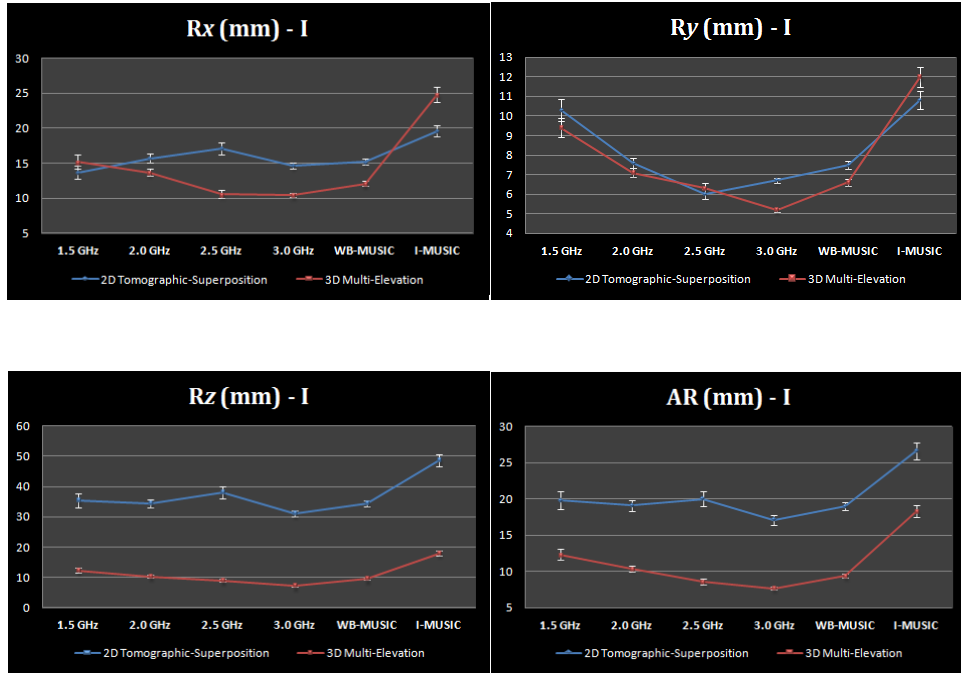
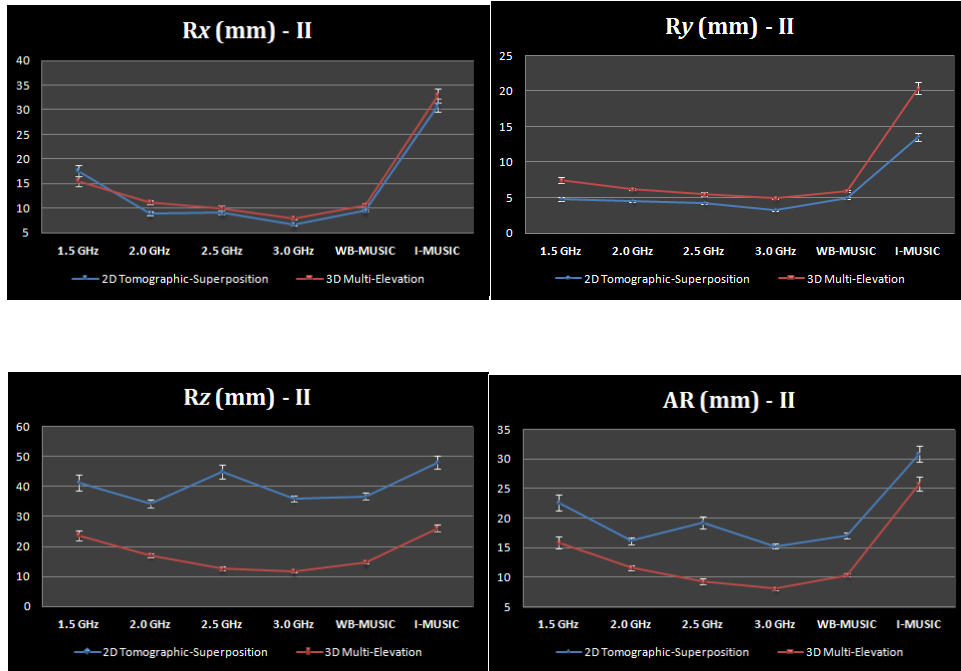


Fig.39: Comparative line graphs of resolution resulting metrics for tomographic-superposition and multi-elevation reconstruction methods.



From the point of view of resolution it emerges that, in both cases (i.e. external and internal tumor), the multi-elevation method vertical resolution  $R_z$  is definitely superior to the tomographic-superposition one, ranging from 2 to 4 times higher resolution. Being the horizontal resolution resulting values  $R_x$  and  $R_y$  comparable between the different types of reconstruction, superiority of  $R_z$  directly impacts also average resolution value, resulting in the multi-elevation AR being 1.5 to 2 times higher than the tomographic one, except for the I-MUSIC case where multi-elevation overall resolution is severely reduced. We can also notice how resolution improves steadily by increasing frequency in the case of multi-elevation algorithm, while in the tomographic-superposition case a constant fluctuation is present, and can be probably associated to the interpolation method which in the present case accounts for  $\sim 80\%$  of the image from only 21 reconstructed slices (i.e. fluctuation should decrease by increasing the portion of reconstructed volume by signal and decreasing the portion of reconstructed volume by interpolation). Obtained contrast results instead show comparable values, although multi-elevation performs slightly worse in case II where the collected scattered signal is much lower. Finally, increased focusing capability by multi-elevation is particularly noticeable in case I, where the absolute dis-

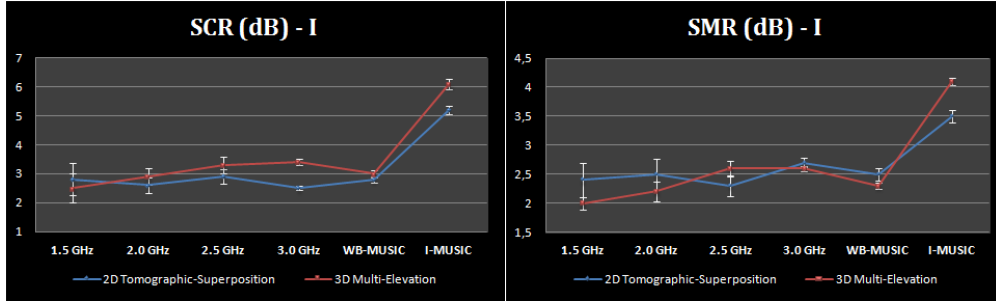
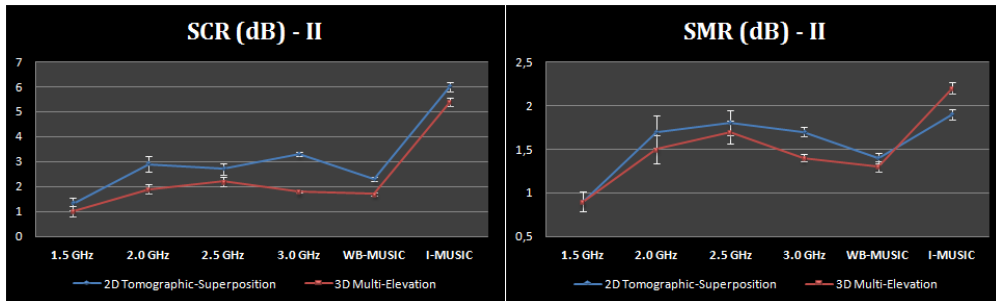


Fig.40: *Comparative line graphs of contrast resulting metrics for tomographic-superposition and multi-elevation reconstruction methods.*



placement at single-frequency is at least 2 times lower than in tomographic-superposition, while the different performance become comparable in case II.

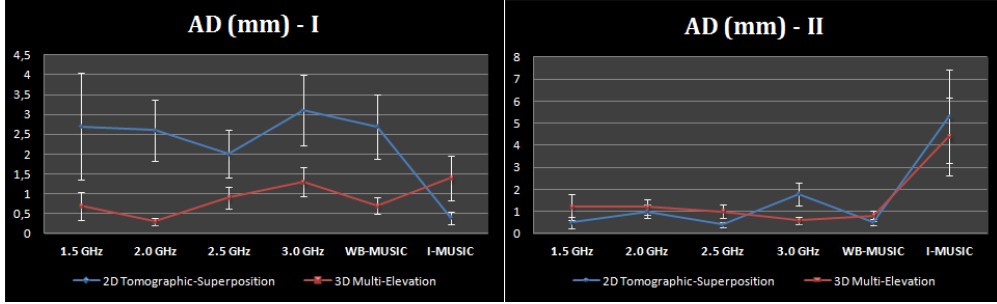


Fig.41: Comparative line graphs of absolute displacement for tomographic-superposition and multi-elevation reconstruction methods.

We have then evaluated the multi-elevation algorithm performance at increased grid spacing, as to simulate a more realistic scenario where fine grid spacing is not available. Thus, we re-reconstructed the imaging volume with 5mm, 10mm and 15mm spacings while arranging vertical grid in a way to include the transverse plane passing in tumor center, which corresponds to using 11, 5 and 3 acquisition planes respectively.

	Image Type	Spatial Metrics(mm)					Contrast Metrics(dB)		p-val
		Rx	Ry	Rz	AD	AR	SCR	SMR	
I	1.5GHz	16,5±1,1	8,7±0,5	11,3±0,7	0,6±0,3	12,3±0,8	2,5±0,5	2,0±0,2	0,86
	2.0GHz	13,3±0,5	7,3±0,2	9,5±0,4	0,5±0,2	10,1±0,4	3,0±0,3	2,4±0,3	0,87
	2.5GHz	11,1±0,6	6,8±0,3	8,3±0,4	0,6±0,2	8,7±0,4	3,4±0,3	2,6±0,2	0,86
	3.0GHz	9,1±0,3	5,1±0,1	8,6±0,4	1,4±0,4	7,6±0,2	3,4±0,1	2,6±0,1	0,82
	WB	11,9±0,3	6,8±0,2	9,3±0,3	0,7±0,2	9,3±0,3	3,1±0,1	2,3±0,1	0,85
	I	25,0±1,1	12,3±0,5	18,5±0,8	1,4±0,6	18,6±0,8	6,3±0,2	4,1±0,1	0,86
II	1.5GHz	12,9±0,8	8,2±0,4	23,8±1,5	1,6±0,8	15,5±1,0	1,0±0,2	0,8±0,1	0,83
	2.0GHz	10,1±0,4	6,3±0,2	17,7±0,7	1,6±0,5	11,5±0,4	2,0±0,2	1,5±0,2	0,83
	2.5GHz	9,0±0,5	5,5±0,2	12,7±0,7	0,9±0,3	9,0±0,5	2,2±0,2	1,7±0,1	0,85
	3.0GHz	8,5±0,3	4,6±0,1	11,3±0,4	0,4±0,1	8,1±0,2	1,9±0,1	1,5±0,1	0,86
	WB	10,0±0,3	5,7±0,2	14,8±0,4	0,8±0,2	10,2±0,3	1,7±0,1	1,3±0,1	0,85
	I	32,0±1,4	18,0±0,8	25,2±1,1	4,3±1,7	24,6±1,1	5,4±0,2	2,3	0,84

Tab.3: Multi-elevation reconstruction algorithm resulting metrics (5mm grid spacing).

	Image Type	Spatial Metrics(mm)					Contrast Metrics(dB)		p-val
		Rx	Ry	Rz	AD	AR	SCR	SMR	
I	1.5GHz	18,5±1,2	8,6±0,5	12,9±0,8	0,6±0,3	13,5±0,8	1,8±0,4	1,9±0,2	0,87
	2.0GHz	14,8±0,6	9,4±0,3	12,5±0,5	0,7±0,2	12,0±0,5	2,3±0,2	2,2±0,2	0,86
	2.5GHz	11,5±0,6	6,1±0,3	11,3±0,6	0,8±0,2	9,6±0,5	3,0±0,2	2,5±0,2	0,85
	3.0GHz	10,9±0,3	5,9±0,1	9,1±0,3	1,8±0,5	8,6±0,2	3,2±0,1	2,7±0,1	0,83
	WB	13,9±0,4	7,5±0,2	10,8±0,3	1,1±0,3	10,7±0,3	2,6±0,1	2,2±0,1	0,85
	I	25,3±1,1	12,3±0,5	16,8±0,7	1,9±0,8	18,1±0,8	5,2±0,2	4,0±0,1	0,85
II	1.5GHz	14,6±0,9	8,9±0,5	20,7±1,3	0,5±0,3	14,8±0,9	1,3±0,3	1,1±0,1	0,86
	2.0GHz	9,5±0,4	7,5±0,2	19,0±0,7	0,5±0,2	11,9±0,5	1,7±0,2	1,3±0,1	0,87
	2.5GHz	11,9±0,6	5,4±0,2	11,7±0,6	1,5±0,5	9,6±0,5	2,4±0,2	1,9±0,1	0,83
	3.0GHz	8,2±0,2	5,8±0,1	11,7±0,4	0,8±0,2	8,4±0,2	1,8±0,1	1,4±0,1	0,85
	WB	10,6±0,3	6,6±0,2	14,7±0,4	0,8±0,2	10,5±0,3	1,8±0,1	1,3±0,1	0,86
	I	29,7±1,3	16,6±0,7	24,9±1,1	5,2±2,1	23,5±1,0	5,2±0,2	2,4±0,1	0,83

**Tab.4:** Multi-elevation reconstruction algorithm resulting metrics (10mm grid spacing).

	Image Type	Spatial Metrics(mm)					Contrast Metrics(dB)		p-val
		Rx	Ry	Rz	AD	AR	SCR	SMR	
I	1.5GHz	19,0±1,2	9,1±0,5	15,7±1,0	1,4±0,7	14,8±0,9	1,8±0,4	2,4±0,3	0,85
	2.0GHz	16,0±0,6	9,7±0,3	11,9±0,5	3,1±0,9	12,5±0,5	2,1±0,2	2,9±0,3	0,82
	2.5GHz	11,2±0,6	7,7±0,3	14,7±0,8	3,0±0,9	11,2±0,6	3,5±0,3	3,4±0,3	0,81
	3.0GHz	12,8±0,4	8,7±0,1	11,5±0,3	4,1±1,2	10,9±0,3	3,0±0,1	3,6±0,1	0,79
	WB	14,9±0,4	8,8±0,3	13,0±0,4	3,2±1,0	12,2±0,4	2,6±0,1	3,0±0,1	0,82
	I	22,3±1,0	12,6±0,5	16,1±0,7	0,3±0,1	17,0±0,7	5,1±0,2	4,3±0,1	0,87
II	1.5GHz	15,1±1,0	33,4±1,8	18,4±1,2	3,7±1,9	22,4±1,3	0,7±0,1	0,4±0,1	0,84
	2.0GHz	10,4±0,4	5,2±0,2	18,0±0,7	3,0±0,9	11,5±0,4	2,3±0,2	1,7±0,2	0,78
	2.5GHz	8,9±0,5	5,2±0,2	13,2±0,7	0,9±0,3	9,0±0,5	2,5±0,2	2,0±0,2	0,84
	3.0GHz	8,7±0,3	5,1±0,1	10,6±0,3	0,9±0,3	8,0±0,2	2,5±0,1	1,9±0,1	0,85
	WB	10,3±0,3	5,6±0,2	14,9±0,4	1,1±0,3	10,3±0,3	1,9±0,1	1,4±0,1	0,83
	I	30,0±1,3	16,2±0,7	26,3±1,1	5,0±2,0	24,0±1,0	5,3±0,2	2,2	0,83

**Tab.5:** Multi-elevation reconstruction algorithm resulting metrics (15mm grid spacing).

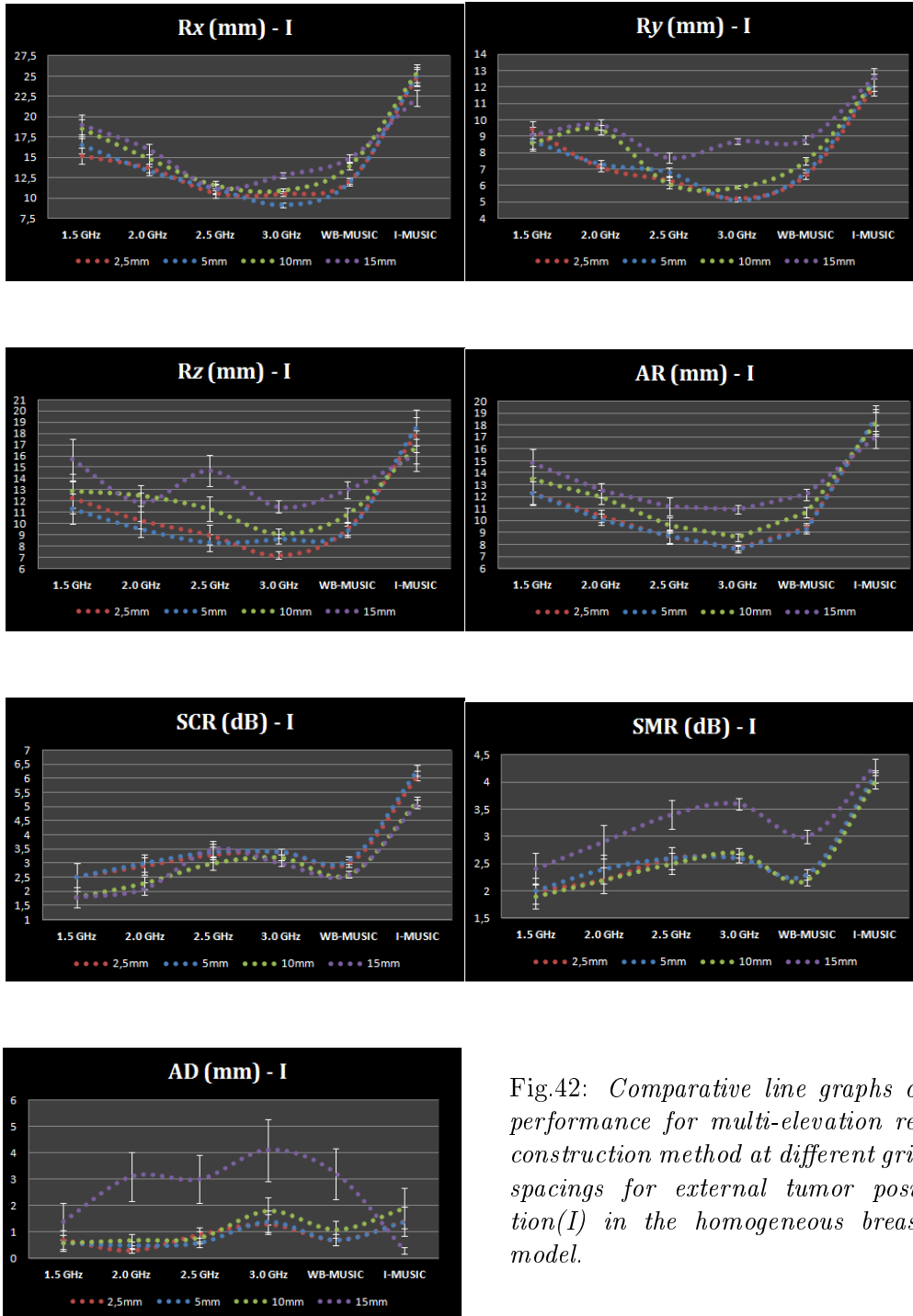


Fig.42: Comparative line graphs of performance for multi-elevation reconstruction method at different grid spacings for external tumor position(I) in the homogeneous breast model.

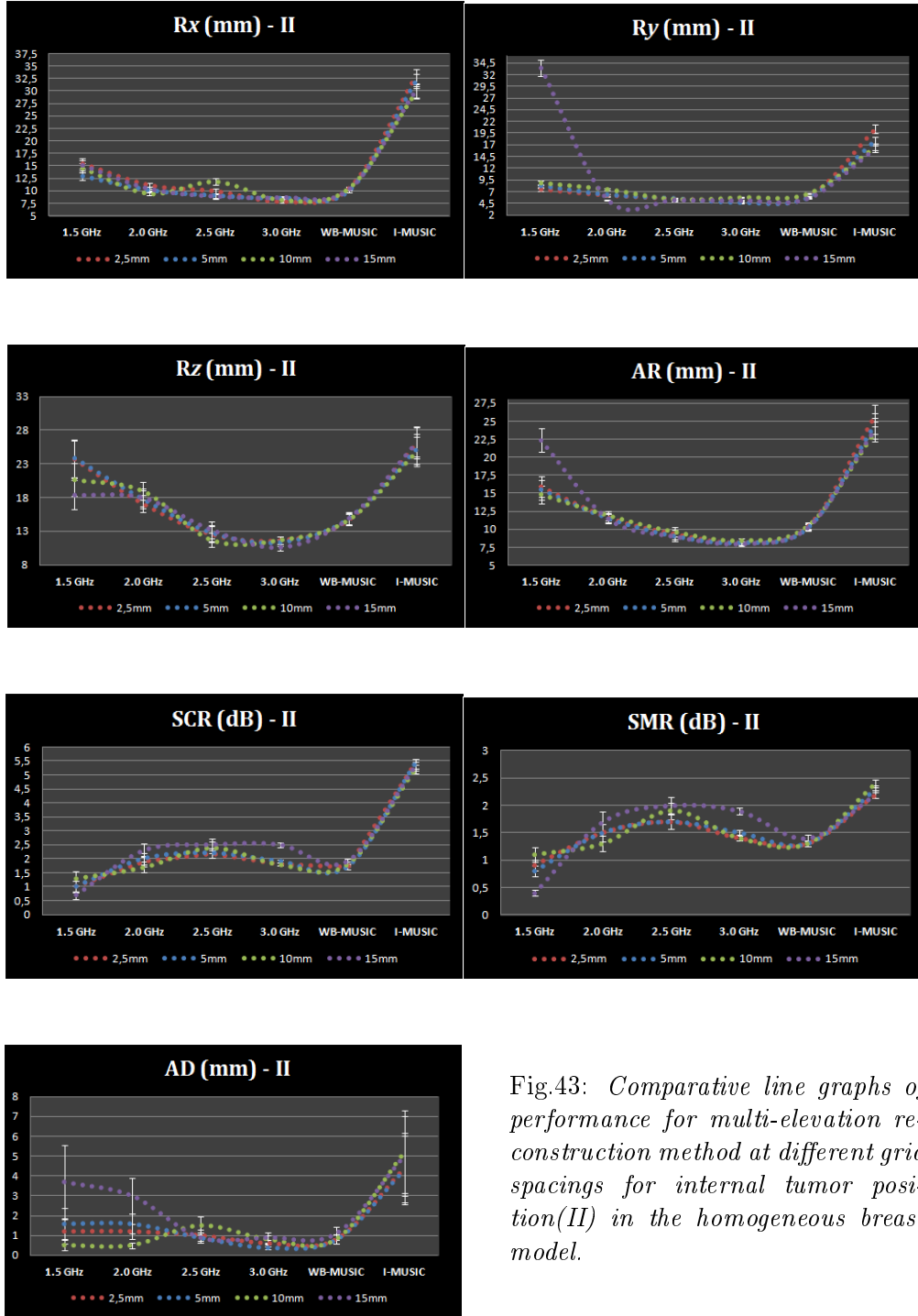


Fig.43: Comparative line graphs of performance for multi-elevation reconstruction method at different grid spacings for internal tumor position(II) in the homogeneous breast model.



In first place we notice that, even lowering the number of heights of a consistent amount (Tab.4, Tab.5), scatterer detection is confidently achieved for both tumor positions. Also, the overall performance doesn't seem to vary by increasing grid spacing from 2,5mm (Tab.2) to 5mm (Tab.3).

In case I, resolution is progressively lowered when switching from 5mm to greater spacings, where it can be seen that lesser focusing occurs at all frequencies: the spot becomes increasingly decentralized towards the closer antenna location, accounting for the most part of recorded scattered signal, and assumes a profile in the shape of a fin tail, resem-

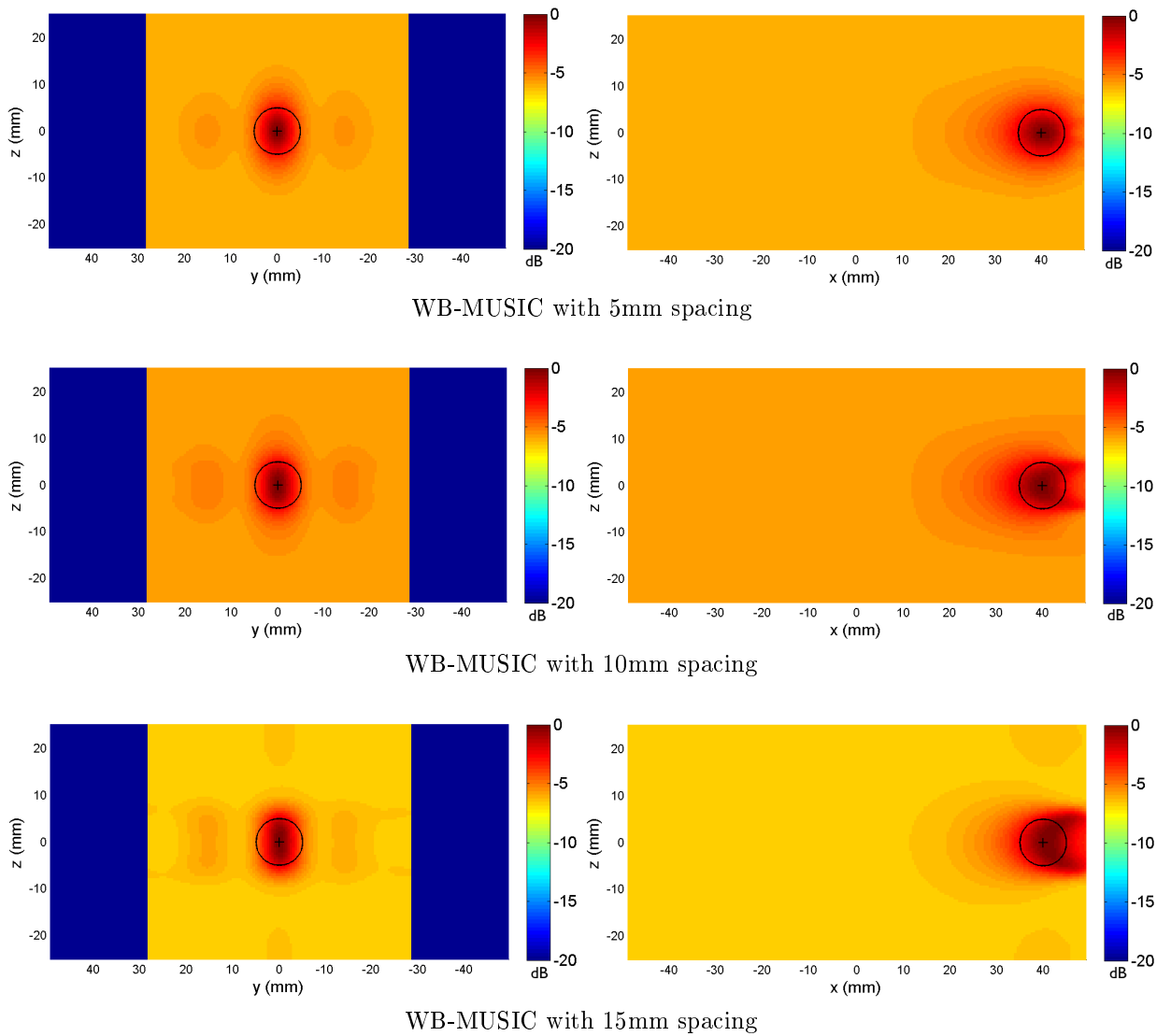


Fig.44: *Sagittal (left) and coronal (right) slice view of multi-elevation reconstruction for different grid spacings; orthogonal planes are centered in the external tumor position(I).*

bling in a predictable way the mono-elevation imaging outcome. As a direct consequence of this behaviour we measure an overall higher SMR, since the tail fin region is completely included in the signal ROI and contains values close to the maximum, and see a net increase in the absolute displacement (estimated centroid location shifts towards skin). In case II we instead notice how increased grid-spacing doesn't seem to affect the overall resolution and observed contrast, even when only 3 antenna planes are exploited. The only exception is to be made at low-frequencies, for which the already weak signal is being recorded by less numerous antennas and can thus lead to the rise of strong clutter areas in the vicinity of tumor position. These areas, which are present in all of the images as a direct effect of skin-reflection and other disrupting agents, can vary consistently in intensity between deterministic reconstructions due to the intrinsic

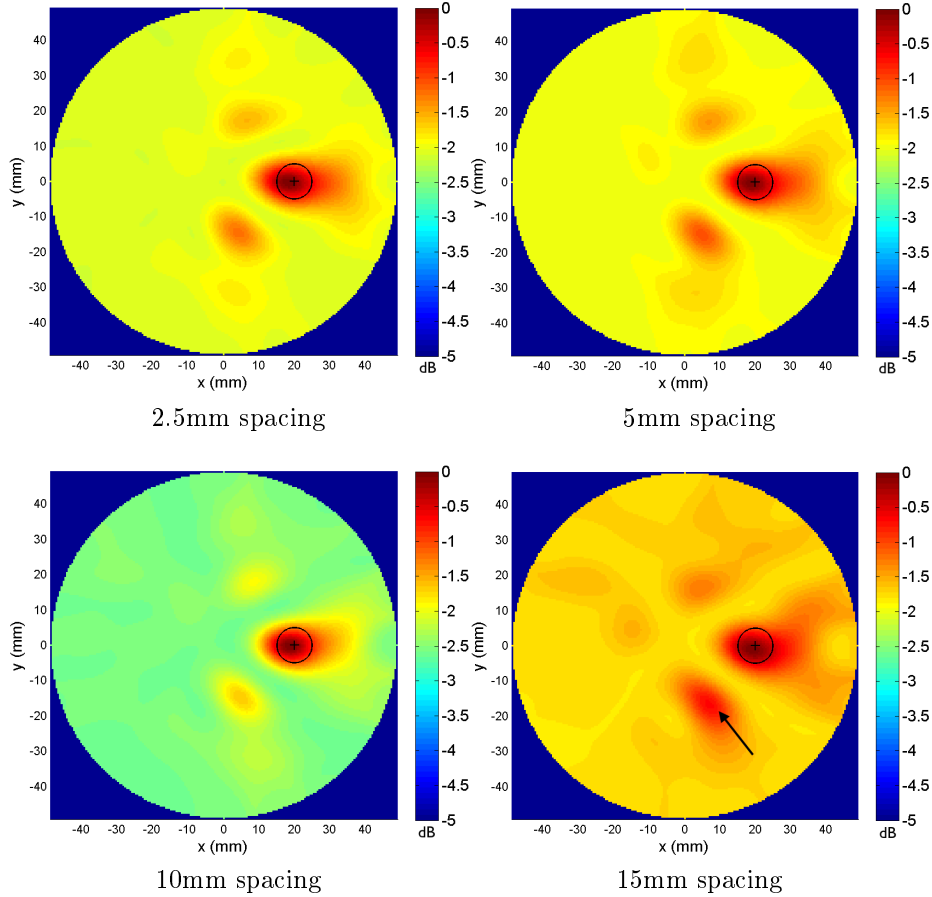


Fig.45: *Transverse plane view at 1.5GHz for internal tumor position(II). The clutter region beneath tumor location in the 15mm spacing reconstruction is strong enough to shift centroid location and cause a major increase in the evaluated dislocation. In other reconstructions, it is well-separated from signal area thanks to superior tumor-to-background contrast.*

stochasticity of added noise; still, an increased number of exploited elevations should on average mitigate their intensity (strong, random signal perturbations are more likely to affect an image given by a less numerous signal data-set). One way to directly solve this issue is, in case clutter region is well definite, to manually set the ROI boundaries and thus prevent clutter portion to enter in the metrics calculus. This approach is particularly useful when we have to work on a few, selected images, otherwise it can be very time-consuming when many reconstructions have to be evaluated and thus the automatic selection becomes a valuable compromise. The net difference between case I and case II resolution  $R_z$  performance trends can be primarily justified by recalling that antenna has a limited vertical vision of the scenario, due to the power-law dependence of the 3D-propagator on the  $\sin \theta$  term. In particular, when the scatterer is close to the domain boundaries (case I), the antenna sees it far-away in most positions (but from a “good” angle<sup>8</sup>), collecting a low signal; viceversa, when the antenna occupies a position at a “right” distance (near the source), the collected signal may result low as well depending on the antenna-elevation, which directly affects  $\theta$ . This means that, in case I, the strongest information entering reconstruction come from the few antennas which “see” the tumor *close* and from a *high*  $\theta$  angle (i.e. the ones near to transverse plane), corresponding to high signal collection: by increasing grid-spacing value, we directly reduce the number of employed antennas which enter in the optimal range-of-sight<sup>9</sup> for detecting tumor and, thus, reduce resolution performance. In case II, instead, since tumor is located in a more centered position, the angular term at increased spacings has a weaker impact on reconstruction, because antenna is capable to “see” even at farther elevations, so the need of closely packed acquisition-planes, in order to keep focusing capability, is eliminated; on the other side, this results in the impossibility, when tumor is deeply buried, of further increasing the resolution by choosing finer grid-spacings. It’s important to remark how, for all the inspected grid-spacings, the multi-elevation algorithm provides better resolution along vertical direction respect to the tomographic-superposition method, in both tumor positions.

### 3.2.3 3D Scatterer Detection in Heterogeneous Media

In this concluding section, we start addressing the problem of detecting a scatterer which has been inserted in a inhomogeneity in the breast. Performance is another time evaluated for the tomographic-superposition and multi-elevation methods, in relation to a single-frequency microwave reconstruction of our virtual breast model, which has been slightly modified in order to cope to the posed objective.

The simulation setup and signal acquisition is pretty much similar to the one previously

---

<sup>8</sup>We recall that  $\theta$  is the *polar* angle, which is the angle between the  $z$ -axis direction and the test-vector  $\mathbf{R}_P$ .

<sup>9</sup>In general, we expect this range to vary with the particular source position and size.

performed: we have collected the signal deriving from the scenario scattering of a single-frequency ( $f = 2.5\text{GHz}$ ) antenna radiation emitted in 20 equispaced circular positions for all the elevation planes in the  $z \in [-25, 25]\text{mm}$  interval with a vertical grid-spacing of 2.5mm. The modified version of the virtual breast model had the skin layer removed (it is actually replaced with a layer with the same dielectric properties of the breast interior), in order to neglect good part of the unwanted clutter contribution and, thus, be able to entirely focus the analysis of our results on the introduced inhomogeneity, at the cost of a lower realism.

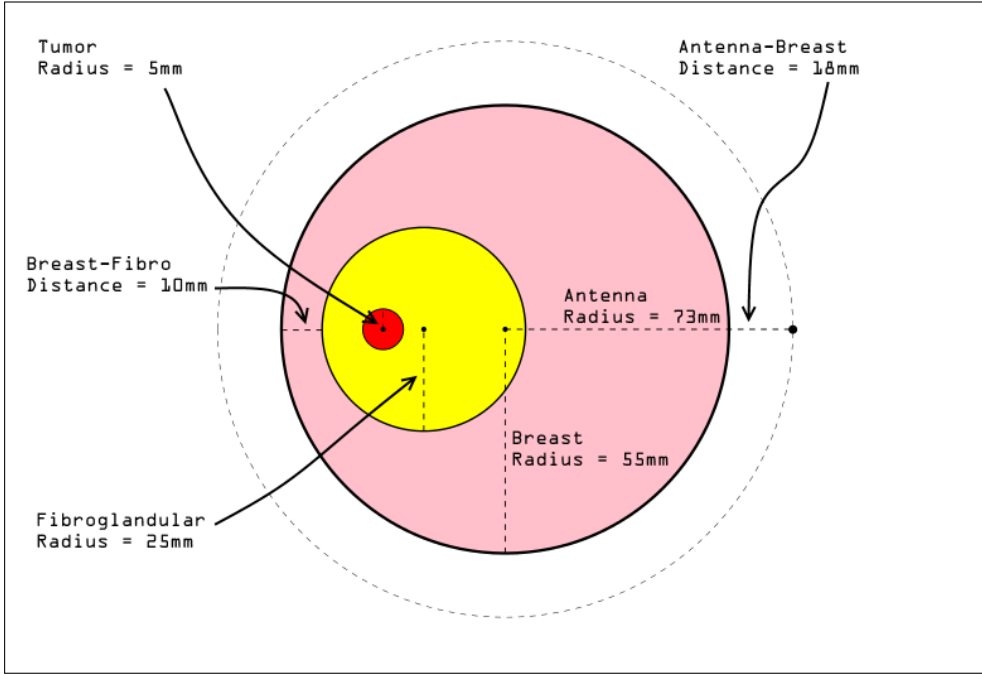


Fig.46: *Transverse plane view of the virtual breast model with heterogeneity and embedded tumor.*

Another simplification was to assign to breast interior the same, fixed dielectric property of the coupling medium, in order to have perfect coupling between antenna<sup>10</sup> and heterogeneity volume; this last has been modeled as an eccentric cylinder respect to the breast interior cylinder rotation axis, meaning that, tumor apart, domain interior is not anymore symmetric by rotation as it was before. One of the main issues associated to system asymmetry is given by how signal filtering is performed: we expect to observe an overall reduced performance due to the fact that the exploited average subtraction filter properly works when clutter contributions are equally perceived in different positions around the breast, while in this situation we already know that each antenna will experience a different one depending on its relative position respect to heterogeneity.

<sup>10</sup>Antenna can be thought as immersed inside the breast-medium.

The experiment has thus been conducted with fixed model properties and for a single tumor position; the only parameter which was varied is the relative permittivity of the simulated fibroglandular region, which is assigned two different values. The general properties of the model are as follows.

– **Breast interior**

Breast radius:  $r^{(b)} = 55$  mm

Breast height:  $l^{(b)} = 12$  cm

Fixed relative permittivity:  $\varepsilon_r^{(b)} = 2.5$

– **Tumor**

Tumor location:  $\mathbf{r}^{(t)} = [-30, 0, 0]$  mm

Scatterer radius:  $r^{(t)} = 5$  mm

Homogeneous dielectric properties:  $[\varepsilon_\infty^{(t)}, \varepsilon_s^{(t)}, \tau^{(t)}, \sigma^{(t)}] = [4, 54, 7, 0.7]$

– **Dipole antenna**

Antenna-breast distance:  $d = 18$  mm

– **Coupling medium**

Fixed relative permittivity:  $\varepsilon_r^{(m)} = 2.5$

– **Fibroglandular tissue**

Fibro (axis) location:  $\mathbf{r}^{(f)} = [-20, 0, 0]$  mm

Fibro radius:  $r^{(f)} = 25$  mm

Fixed relative permittivity(I):  $\varepsilon_r^{(f)} = 5$

Fixed relative permittivity(II):  $\varepsilon_r^{(f)} = 8$

From now on we will customarily refer to the simulation results relative to heterogeneity with  $(\varepsilon_r^{(f)} = 5)$  as case I and to the other one with  $(\varepsilon_r^{(f)} = 8)$  as case II.

	Image Type	Spatial Metrics(mm)					Contrast Metrics(dB)		p-val
		Rx	Ry	Rz	AD	AR	SCR	SMR	
I	TS	9,7±0,5	8,6±0,4	52,8±2,7	8,0±2,4	24,0±1,2	2,5±0,2	2,6±0,2	0,79
	ME	13,8±0,7	10,1±0,4	32,0±1,7	6,4±1,9	18,7±0,9	1,9±0,2	1,4±0,1	0,79
II	TS	12,7±0,7	7,9±0,3	46,0±2,4	8,1±2,4	22,2±1,1	2,2±0,2	2,3±0,2	0,78
	ME	13,6±0,7	10,4±0,4	33,2±1,7	6,6±2,0	19,0±1,0	1,7±0,1	1,3±0,1	0,80

**Tab.6:** Reconstruction results of the heterogeneous breast model at 2.5GHz for tomographic-superposition (TS) and multi-elevation(ME) algorithms.

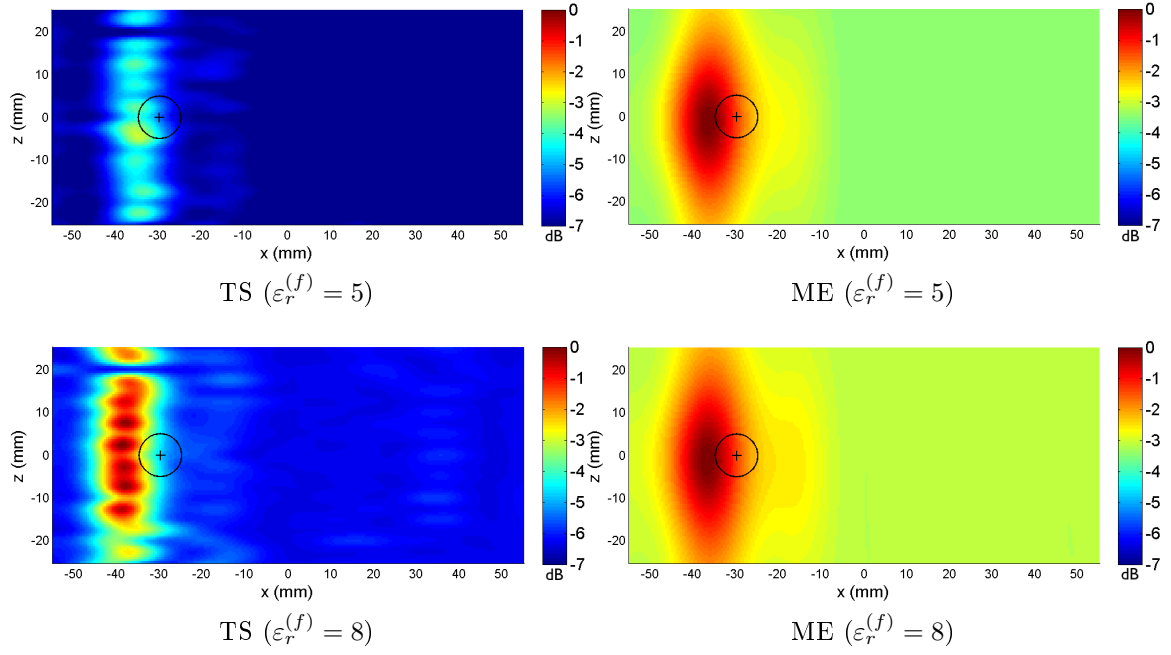
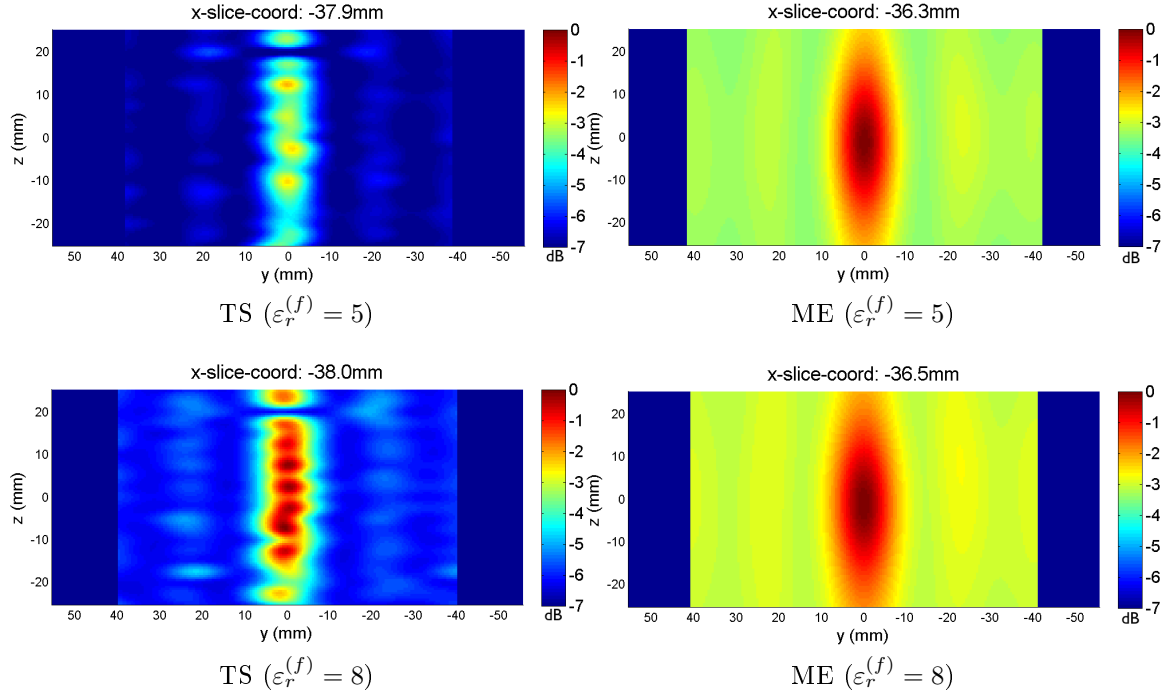


Fig.47: Coronal (top) and sagittal (bottom) slice view of the resulting pseudospectrum at 2.5 GHz for tomographic-superposition (TS) and multi-elevation (ME) reconstruction methods, applied to the heterogeneous breast phantom. Sagittal slices have been taken in the  $x$ -coordinate of estimated centroid location, which is reported above each figure.



Despite the use of average filtering, both algorithms are capable of detecting the source inside heterogeneity. As it could be expected, however, a major displacement factor in all reconstructions is observed, due to the heterogeneity layer covering the source, and it can be visually seen that the identified spot location is always closer to the outer part of the breast: this is because the heterogeneous layer effective thickness appears inferior for antenna positions closer to tumor, where recorded signal is stronger, and, viceversa, appears higher for farther antenna positions, accounting for lesser scattering signal from the tumor. This means that, for the particular geometry of our model, these latter positions are further penalized in providing localization information and, so, they cannot correctly balance the stronger contributes associated to closer-to-tumor antennas<sup>11</sup>.

The absolute displacement value is generally superior in the tomographic-superposition reconstruction, deriving from lesser capability of focusing the spot along  $z$  (notice how the 3D-propagator reconstruction designates a concentrated spot, while 2D-superposition gives place to a series of sparse ones), which then provokes a sensible vertical displacement of estimated centroid. Resolution in  $z$  is, in fact, notably superior in the ME reconstruction, while ME horizontal resolution performance is slightly worse than TS one. Experimentally, the same difference in relative performance was also observed in the previous section when reconstructing the homogeneous breast model for the internal scatterer position.

As well, the contrast metrics are noticeably higher in the TS algorithm. Having an overall diminished contrast is a peculiar drawback of the ME method which, for how it operates, evaluates the correlation term<sup>12</sup> from the entire signal matrix  $\mathbf{S}(\omega)$ : it's particularly rare to observe space-point correlation drop from high to low value, when it depends on such a high number of *different* acquisition positions (420 in the current setup) and, as a result, correlation is seen to drop smoothly from a focused region to image background. In the TS algorithm, instead, every acquisition plane is used to *separately* reconstruct tomographic-slices, which means that space-point correlation is evaluated with many less signal-data (20 per elevation) and sharp falls are more likely to occur; this structural difference could also be related to the superior performance observed for TS in horizontal resolution. In substance, the particular approach of ME sacrifices general contrast capability in spite of robustness (it's more difficult for clutter areas to arise) and overall enhanced focusing around few, concentrated spots.

Finally, we notice that a sensible *blurring* occurs on reconstructed images by increasing the heterogeneous region dielectric permittivity  $\varepsilon_r^{(f)}$ . This effect directly derives from the increased quantity of scattering due to heterogeneity, which physically influences the signal recorded by each antenna during the simulation phase: in particular, we expect

---

<sup>11</sup>This issue can be optimally solved by exploiting more powerful filtering techniques, which are capable of taking into account the clutter contribution for each individual channel; their implementation and analysis is, however, beyond the scope of the present work.

<sup>12</sup> $(\|\cos\eta_p\|^2)$  gives the probability that the measured signal vector is actually given by a single-scattering process, occurring in the test-point location  $\mathbf{R}_p$ .

that at increased  $\varepsilon_r^{(f)}$  more points in the heterogeneity will take part in the formation of recorded signal, giving place to an extended region providing positive point-correlation during pseudospectrum reconstruction. We can see that SMR and SCR (Tab.6) in case II are sensibly reduced for both TS and ME methods respect to case I due to blurring. This effect further proves visible evidence (Fig.47) in the form of back- (coronal slice) and side- (sagittal slice) enlargement of the spot in the ME image; in the TS image, instead, it's quite noticeable how both signal and clutter areas are raised<sup>13</sup> in correspondence of outer heterogeneity. Generally, the scattering due to the heterogeneity region is a frequency-dependant behaviour which is usually investigated by employing multi-frequency strategies.

In the very last part of this study, we performed multi-elevation reconstruction of the heterogeneous model with increased grid-spacings (5mm, 10mm, 15mm), corresponding to the utilization of less numerous antenna planes (11, 5, 3).

	Image Type	Spatial Metrics(mm)					Contrast Metrics(dB)		p-val
		Rx	Ry	Rz	AD	AR	SCR	SMR	
I	5mm	14,1±0,7	9,3±0,4	33,5±1,7	7,7±2,3	19,2±1,0	1,5±0,2	1,1±0,2	0,72
	10mm	14,4±0,7	11,6±0,5	29,5±1,5	8,1±2,4	18,3±0,9	1,3±0,1	1,0±0,1	0,70
	15mm	13,4±0,7	9,1±0,4	31,1±1,6	6,3±1,9	18,0±0,9	2,4±0,2	1,7±0,1	0,80
II	5mm	14,5±0,8	8,4±0,4	36,5±1,9	7,7±2,3	20,1±1,0	1,3±0,1	1,0±0,1	0,74
	10mm	14,9±0,8	10,6±0,4	33,4±1,7	8,4±2,5	19,5±1,0	1,2±0,1	0,9±0,1	0,70
	15mm	12,1±0,6	10,5±0,4	30,1±1,6	6,9±2,1	17,5±0,9	2,3±0,2	1,8±0,1	0,79

**Tab.7:** *Reconstruction results of the heterogeneous breast model at 2.5GHz for multi-elevation algorithm at different grid-spacings.*

It's very important to notice how increasing grid-spacing up to 10mm brings to an overall image degradation (Fig.48) respect to the 2,5mm spacing, while the 15mm reconstruction offers a better one, in particular in terms of SMR; furthermore, the outcome in this case seems not to be influenced from increasing  $\varepsilon_r^{(f)}$  from 5 to 8, which usually has a worsening effect on reconstruction (Fig.48). Depending on the particular tumor size, fibroglandular region extension, working frequency and involved dielectric constants, there may exist an optimal grid-spacing setup that manages to collect most information from tumor and least from fibroglandular region with a limited number of antennas. This is particularly plausible in the ME reconstruction, where correlation calculus is performed on the entire signal matrix, and when more antennas are likely to collect information from the enveloping region than the tumor; the behaviour should also depend on the particular type of employed propagator (in our case, only the  $E_z$  component is evaluated).

<sup>13</sup>Thus, their mean and max ratios don't increase in practice.



As for the homogeneous breast phantom model, we notice that also in the heterogeneous case the multi-elevation method performs better than the tomographic-superposition one in terms of vertical resolution, also when grid-spacings leading to performance degradation are employed.

We conclude suggesting that the *shielding* effect caused by the heterogeneous tissue could be addressed by adopting multi-channel techniques (e.g. multistatic configuration), in which the single-scattering information from tumor is registered by more antennas (the non-transmitting ones), because much part of it is lost when a multi-monostatic antenna setup is employed; this solution, along with multi-channel filtering techniques, can hopefully aid in the future to provide an enhanced reconstruction.

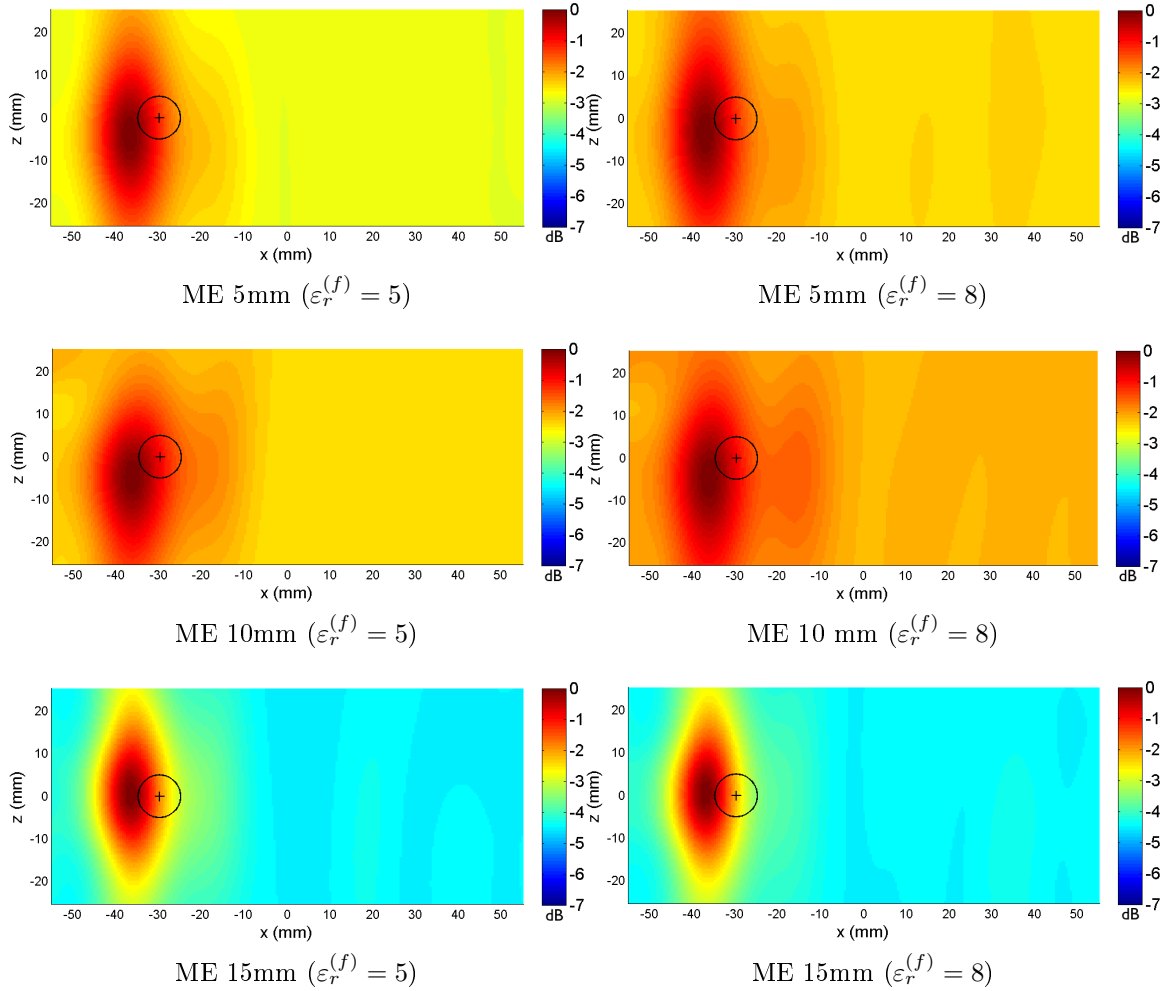


Fig.48: Coronal slice view of the resulting pseudospectrum at 2.5 GHz for multi-elevation (ME) reconstruction method at different grid spacings for the heterogeneous breast phantom.

## Chapter 4

# Experimental Measurements

The multi-elevation 3D-reconstruction algorithm is a linear-inversion method which was developed during the present thesis and which relies on the pseudospectrum formation by evaluating the correlation between the signal matrix  $\mathbf{S}(\omega)$  and the monostatic response matrix for any given test-point  $\mathbf{R}_p$  in the imaging domain. In particular, the monostatic response matrix can be entirely described in terms of the Green's propagator function, which was by us implemented in the form of the Hertzian dipole electric-field propagator with a scalar approximation(2.7).

The reconstruction algorithm was preliminarily tested and evaluated for synthetic data, which were acquired via a software-simulated environment through the microwave irradiation of a virtual breast-phantom. Simulations are generally very useful since they let us have a complete control of the physical and geometrical properties of the system we want to investigate, so they can be fruitfully used in advance in order to get an insight on the strenghts and defects of the particular method we're exploiting. Still, simulation tests are by far limitative respect to a complex, real-life scenario; simulation results can be used only to *partially* predict a real experiment outcome and, in this sense, their analysis is much valuable because it can help us to focus on the most critical aspects for a given model.

In this final chapter, we want to evaluate the reconstruction performance of the multi-elevation algorithm starting from real-life laboratory data, acquired by means of a breast-phantom prototype and antenna piloting system in the microwave laboratory at DIFA, University of Bologna. The various experiments which were arranged aim at partially recreating the operational conditions exploited during simulation phase, in the hope of being able to take advantage of the previously done analysis and succesfully validate experimental data.

The results that have been achieved and are here presented derive from the joint efforts of the present candidate and Nanetti F. [80], colleague candidate responsible, in this part of the work, of the real-hardware programming and measurements automation-system.

## 4.1 Experimental Setup



Fig.49: *Picture of the microwave laboratory data acquisition chain.*

The experimental data acquisition system we utilize is composed of a breast-phantom prototype, an automated measuring system and a graphical interface.

### 4.1.1 Breast Phantom Prototype

The prototype we use, ACHILLE, is the second breast-phantom developed in the microwave laboratory at University of Bologna. It mainly consists of three components, which are the breast interior region, the skin layer and the tumor; its geometrical and physical configuration resembles the simulated setup previously implemented with COM-SOL Multiphysics.

The breast interior is an open plastic cylinder of radius  $r^{(b)} = 55\text{mm}$  and height  $l^{(b)} = 50\text{cm}$  which is, by default, filled with *seed oil* in order to obtain the characteristic dielectric properties of a homogenized breast adipose tissue:  $\varepsilon_r^{(b)} = 2.5$ . In order to confer heterogeneity to the phantom, another open cylinder of radius  $r^{(f)} = 25\text{mm}$  can be included inside the main breast structure and, in a later moment, be filled with a proper fluid to grant the desired  $\varepsilon_r^{(f)}$ . The skin layer is given by the cylinder own plastic wall, which is characterized by a thickness  $t^{(s)}$  and unknown dielectric properties. Finally, the tumor is given by an extractable insert: in the present work, we adopted two different

ones (Fig.50) which were freely changed depending on the particular microwave imaging experiment (homogeneous/heterogeneous breast model) we wanted to realize.



Fig.50: *Picture of the inserts.*

In the homogeneous experiment, we have used GLASSBURGER, which consists of two hemispherical, smooth glass stones, glued at their base together with a nylon string by a drop of hot glue: the resulting object geometry is roughly approximated to a spherical one, with a radius  $r^{(G)} = 8\text{mm}$ . The dielectrical property of this insert is assumed to be equal to the relative permittivity of glass,  $\varepsilon_r^G = 5$ .

In the heterogeneous experiment, instead, we adopted PATROCLO, a plastic bottle of cylindrical form of height  $l^{(P)} = 30\text{mm}$  and base radius  $r^{(P)} = 8\text{mm}$ . To confer the wanted dielectrical property to the insert, the bottle was filled up to  $l_{filled}^{(P)} = 16\text{mm}$  with a solution made of (60% alcool, 40% water), resulting in  $\varepsilon_r^P = 47$ , while the remaining part of the bottle interior was filled with seed oil (in order to limit the effective scatterer dimensions). Also this insert has been glued together with a nylon string, which is necessary for immersing the tumor into the wanted breast region.

In order to perform signal measurements, the whole phantom-system is being rotated of discrete angular steps around the structure main axis under the action of an electrical motor: at each position, a dipole antenna emits an excitation radiation and collects scattered signal through a Vector Network Analyzer (VNA). The whole breast system we described is supported by a reinforced wooden structure on the top side and by a circular guide on the bottom; phantom rotation is achieved by connecting the main cylinder breast structure to a stepper motor with a toothed belt. In order to provide automatic data acquisition, the stepper motor is driven by the LabView interface, and the piloting software has been specifically developed by Nanetti.

### 4.1.2 Dipole Antenna Transceiver

During this experiment, a half-wave dipole antenna is exploited, which is a particular type of dipole antenna with linear dimension  $l$  equal to half-wavelength  $\lambda$ . Its radiated field component  $E_\theta$  can be directly computed by letting  $l = \lambda/2$  in the ideal dipole radiated field equation:

$$E_\theta = j\eta \frac{I_0 e^{-jkr}}{2\pi r} \left[ \frac{\cos\left(\frac{\pi}{2} \cos\theta\right)}{\sin\theta} \right] .$$

The particular model we used is the ANT-24G-905-SMA antenna, developed by RF Solutions, which has the following specifications.

- Frequency range: 2.4 – 2.5 GHz
- Gain: +5 dB
- Vertical Polarization
- Internal/External usage
- Adjustable 90° SMA connector

### 4.1.3 Vector Network Analyzer

A network analyzer is an instrument generally used to analyze the transmission and reflection behaviour ( $S$ -parameters) of electrical networks, including their frequency dependent electrical properties. In order to measure  $S$ -parameters, the electrical device is tested in a broad frequency range: operating frequencies can vary in a wide range (5Hz – 1.05 THz), though the reflection and transmission properties are easier to measure at high frequencies.

A vector network analyzer, specifically, is able to measure both amplitude and phase properties for an inspected device by sending a signal of a certain amplitude and phase to the device under test and then measuring the amplitude and phase of both the reflected and transmitted signal. In the case of a generic *multiport* network with  $N$  ports, the *incident* power wave on each port is defined by

$$a = \frac{1}{2}k(V + Z_p I) ,$$

while the *reflected* power wave is given by

$$b = \frac{1}{2}k(V - Z_p^* I) .$$

Here,  $Z_p$  represents the diagonal matrix of the reference complex impedance for each  $n$ -th port and  $Z_p^*$  is the complex conjugate of matrix  $Z_p$ . The column vectors  $V$ ,  $I$  contain the values of voltage and current for each port and  $k$  is given by

$$k = \left( \sqrt{|\Re[Z_p]|} \right)^{-1} .$$

When the reference impedance is the same for all the  $N$  ports, the incident and reflected power waves can be rewritten as

$$a = \frac{1}{2} \frac{(V + Z_0 I)}{\sqrt{|\Re[Z_p]|}}$$

$$b = \frac{1}{2} \frac{(V - Z_0^* I)}{\sqrt{|\Re[Z_p]|}} .$$

Reflected power waves can be defined, for all the ports, in terms of the  $S$ -parameters matrix and incident power waves as  $b = Sa$ , where  $S$  is a  $N \times N$  matrix and each  $ij$ -element is given by the ratio of reflected to incident power wave

$$S_{ij} = \left. \frac{b_i}{a_j} \right|_{a_k=0}, \quad \forall k \neq j .$$

In a specific *biport* configuration, four  $S$ -parameters can be defined

$$S_{11} = \left. \frac{b_1}{a_1} \right|_{a_2=0} \quad S_{22} = \left. \frac{b_2}{a_2} \right|_{a_1=0} \quad (\text{reflection coefficients})$$

$$S_{12} = \left. \frac{b_1}{a_2} \right|_{a_1=0} \quad S_{21} = \left. \frac{b_2}{a_1} \right|_{a_2=0} \quad (\text{transmission coefficients})$$

and they respectively represent “the ratios of incident wave amplitude to the amplitude of the resultant wave reflected back to the incident port” and “the ratios of the incident wave amplitude at one port to the amplitude of the resultant wave transmitted to the opposite port”. In this situation VNA uses a single RF source, that is switched between port 1 and 2, to create the incident wave  $a$ , which then becomes the reference signal in the determination of the  $S$ -parameters.

In this work we have used the S5048 VNA (Fig.) developed by Copper Mountain Technologies, which is a two-ports instrument designed for operating with a PC.



Fig.51: *Biport S5048 VNA.*

The instrument presents the following specifications:

- Frequency range: 20 kHz – 4.8 GHz
- Measured  $s$ -parameters:  $S_{11}, S_{12}, S_{21}, S_{22}$
- Sweep types: linear frequency, log frequency, segment, power sweep
- Dynamic range: 120 dB (10 Hz)
- Measurement speed: 250  $\mu$ s per point at 85 dB dynamic range
- Output power adjustment range: -50 dBm to +5 dBm
- Up to 200,001 measurement points per sweep.

By connecting the VNA to the laboratory computer, we can measure the complex valued (amplitude and phase)  $S$ -parameters for a chosen frequency range with the own manufacturer software. The parameters can also be obtained in the form of gain values

$$G = 20\log_{10}(S_{ij}) .$$

In the current experience, only the term  $S_{11}$  is measured by the antenna, and it characterizes the measured reflected wave by the scattering source. Measurement of the  $S$ -parameter is thus performed at different positions and frequencies, building up the previously introduced signal matrix  $\mathbf{S}(\omega)$ , which is then exploited in order to reconstruct the pseudospectrum image.

## 4.2 Operational Conditions

When acquiring synthetic data, a consistent amount of time (days, in our case) is usually necessary before accessing to them, due to the complexity and computational effort of the FEM simulations which, after calculations, provide very accurate information on the response of the examined system.

During a real laboratory experimental activity in microwave imaging, instead, much of the effort is usually done before actual data acquisition: the acquisition chain needs to be prepared accordingly, respect to the particular problem under exam, and the model must be at first designed carefully and then assembled in order to describe the particular situation. After preparing it all, the data-acquisition phase is much faster respect to the simulation case, especially if a fully-automated system is available, as in our case, and the amount of collected data is incomparably superior as well.

The piloted VNA-antenna system is used to acquire the signal  $S_{11}$  for all the frequencies in the 100MHz – 4 GHz range with a step of nearly 10MHz, thus collecting approximately 400 frequencies per antenna position. The main problem associated to this huge amount of data is how to effectively select signal data, in terms of precise frequency: multifrequency analysis can be indeed performed but, in a 3D-reconstruction scenario, one cannot generally afford reconstructing pseudospectrum at *all* available frequencies, both in terms of computational time and for obtaining significative measures from each 3D-image per frequency, which should further be analyzed.

Another actual problem is given by the fact that the antenna is in a fixed position and cannot be vertically traslated: the stepper motor doesn't actually move the antenna around the phantom but instead rotates the breast cylinder around its axis. This way, since we aim at reconstructing a 3D-scene by means of a multi-elevation acquisition method, we're practically forced to immerse the tumor-insert inside the breast at different depths and then calculate the equivalent height assumed by the antenna in that configuration. While this is not hard to calculate, in practice it limits the precision of the measure since we must bind the insert to a nylon string and then immerse it in the phantom by discrete steps; by picking an excess or defect step of immersion estimate we both rescale the actual elevation-grid of the antenna and also shift the acquisition planes position, thus giving place to a definite increase in delocalization (along the vertical) way before the start of reconstruction.

Another real issue which has to be mentioned is given by the motion of the insert, hanging to the nylon string, during breast phantom rotation. It was set a waiting time of 20 seconds between the instant of motor-stopping and the start of acquisition in order to let the tumor position stabilize; this problem should however become of minor importance when insert is immersed in a viscous fluid (e.g. seed oil) but could give rise to a noticeable displacement along the horizontal directions in other cases.

Finally, we remark that it has not been possible to perform a fine-grid imaging as it could be achieved during virtual simulations, due to the general lack of precision for the



instruments used in vertical descent estimation (we employed a nylon string connected to a rudimental winch).

### 4.2.1 Frequency Selection Working Interface

By practically addressing the problem of choosing a limited amount of frequencies for reconstruction, we have developed a Matlab interface in order to visualize and select the frequencies associated to highest SMR values in bidimensional pseudospectrum images, which have been calculated in correspondence of each image maximum value. While doing so, we hypothesize that SMR can be a crucial point in the detection of a source, since a strong scatterer is usually assumed to exhibit a particularly high contrast respect to the rest of the imaged scenario. Still, we know that high SMR isn't always connected to the presence of an actual object and can be in fact due to artefacts created during the reconstruction process. This way, we opted for creating a simple working interface which lets the user visualize how the maxima are spatially distributed and, optionally, select to extract information on the wanted region by drawing a rectangular shape in the clustering map: one can choose whether to completely discard signal-data resulting from a particular acquisition, if it seems to mostly provide sparse, noisy maxima, or otherwise perform data-extraction on a clustered region<sup>1</sup>.

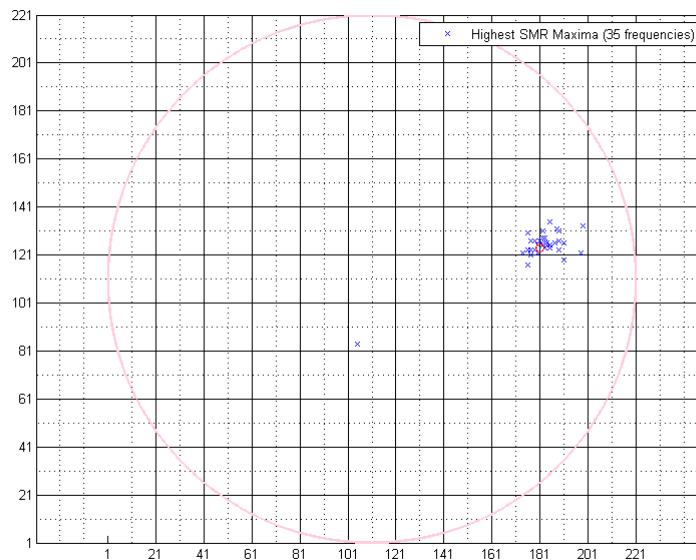


Fig.52: *Frequency selection interface in the (2.5 - 3.0)GHz range. Blue crosses represent the locations of maximal pseudospectrum values derived at different frequencies, while red circle represents the clustering center of the maxima. Axis values are in image-pixel coordinates.*

<sup>1</sup>The choice is not trivial since also clutter regions tend to cluster and have high SMR.

At first we use the signal vector  $\mathbf{S}(\omega)$  provided by VNA-antenna system to reconstruct 2D pseudospectrum images for all the frequencies at which the breast is irradiated. In a second phase, a 2D-reconstruction algorithm automatically evaluates the metrics for each image by choosing a ROI of fixed dimensions on the image maximum value, and the algorithm finally returns in output the calculated values along with the location of each maximum and the corresponding frequency. Finally, we visually display the locations of the maxima at a particular depth and in a pre-selected frequency range with the developed working interface, which as a tool can be used in order to select a ROI in the clustering map and return the present frequencies in order of highest SMR.

This way, we selectively choose to work with the few frequencies which have proven to have a high associated SMR and that compare in noticeably clustered environment. The algorithm also calculates and displays the single-clustering centroid, which is calculated with the center-of-mass method (respect to maxima coordinates and relative SMR) and can thus help in visually evaluating the strength of a single clustering region when more sub-clusters are present.

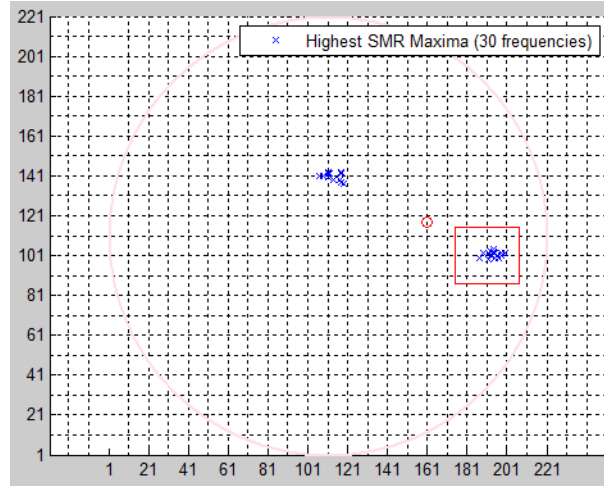


Fig.53: *Frequency selection interface in the (2.0 - 2.5)GHz range. The cluster in the upper part is associated to the presence of an extended heterogeneous region, while the rectangle-selected cluster of maxima is associated to the insert.*

Of course, the tool utility is highly focused on the scope of this particular activity since, in practice, we can drastically limit our search by already knowing the actual tumor location and, thus, is not meant to be a definitive solution for the posed problem: implementation of more complex methods need to be addressed when tailoring choice automation and clutter-rejection methods in a real tumor detection scenario. Still, in practice it's always a good idea to let the user have a role in the choice of such important features, since the entire reconstruction heavily relies on the particular frequencies exploited.

As a last note, we want to point out that the observed resolution  $R_z$  of 2D-methods does,

in this case, come to a concrete advantage in providing clustering information also when the insert is not actually present at a particular height: out-of-plane vision ensures that lesser information can also be retrieved at relative distances of the order of the vertical resolution, for clustering maxima gradually tend to spread when moving away from the actual tumor-plane, and, when in plane with the object, 2D grants noticeable contrast information.

### 4.3 Homogeneous Breast Phantom Reconstruction

During the first imaging experience, we have adopted GLASSBURGER insert ( $\epsilon_r^G = 5$ ) for the homogeneous phantom, which has been entirely filled with oil seed ( $\epsilon_r^{(b)} = 2.5$ ): the glass-ball is immersed at a total of five different depths in corresponde of the external hole of the aluminium cap which closes the breast phantom on the upper side, and is located at radial distance  $r_{ext}^h = 40\text{mm}$  respect to the breast center. The external hole diameter is as large as 16mm and the insert has been attached to the upper border of the hole when is located in the east position, by which we estimate the scatterer to be located at  $\mathbf{r}^{(G)} = [40, 8, 0]\text{mm}$  in the breast phantom coordinate system.

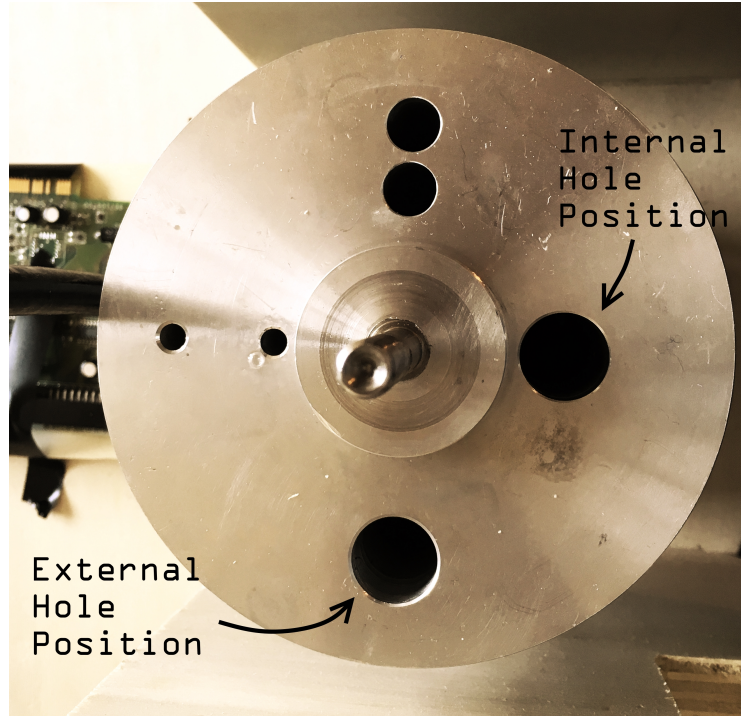


Fig.54: *Picture of the aluminium cap closing the phantom. Hole positions can be used to embed tumor inserts of proper size.*

The depth immersions have been estimated at  $h_0^{(t)} = -50\text{mm}$ ,  $h_1^{(t)} = -25\text{mm}$ ,  $h_2^{(t)} = 0\text{mm}$ ,  $h_3^{(t)} = 25\text{mm}$  and  $h_4^{(t)} = 50\text{mm}$  respect to antenna plane, so the imaging-grid has a spacing of 25mm between adjacent elevations. Measures of the different segments on the nylon string have been performed with a standard ruler, so the error on each estimate is of the order of 1mm.

In order to reconstruct the full volume in the range  $z \in [-50, 50]\text{mm}$  we have utilized the frequency working interface to obtain the signal value for each height: the frequencies that have been chosen are the ones providing the best SMR value in correspondence of the scatterer-plane. We exploited a total of four frequencies during reconstruction:

$$\mathbf{f} = [2.1, 2.3, 2.5, 3.0]\text{GHz} .$$

In this treatise, the frequency values were by us reported with the precision of the decimal of GHz, but the actual frequency values are given by VNA with a precision of the ten thousandth of GHz; we have exploited the *exact* frequency value during reconstruction for every corresponding height.

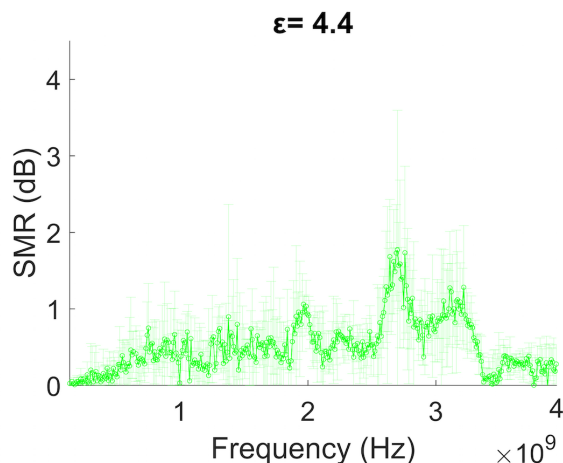
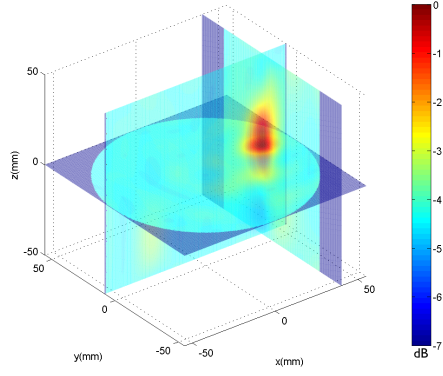


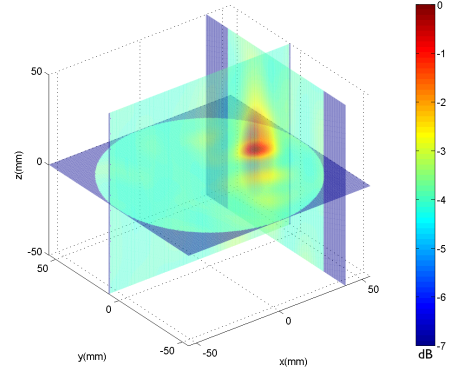
Fig.55: Graph with mean SMR values in function of frequency for a material with  $\epsilon_r = 4.4$ .

The frequency investigation interval has been limited to the range between 2.0GHz and 3.5GHz: statistical analysis performed by Nanetti[80] on the frequency-dependance of the SMR for a material with  $\epsilon_r$  value similar to the one employed for the present case (Fig.54) shows that better imaging results, in terms of contrast offered by the item, are more probably present in this range of frequencies, even if the uncertainty values associated to SMR are substantially high at all frequencies.

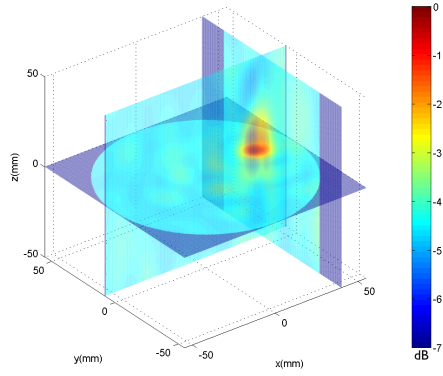
Volumetric reconstruction has thus been accomplished for both the tomographic-superposition (previously introduced as an interpolation-based technique) and multi-elevation method over the entire vertical range covered by the antenna planes at the chosen frequencies.



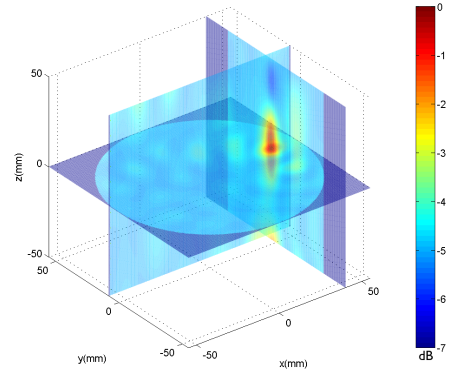
$f = 2.1\text{GHz}$



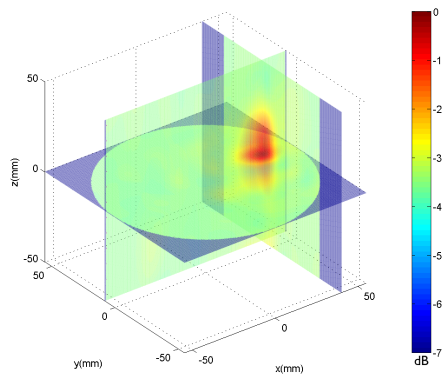
$f = 2.3\text{GHz}$



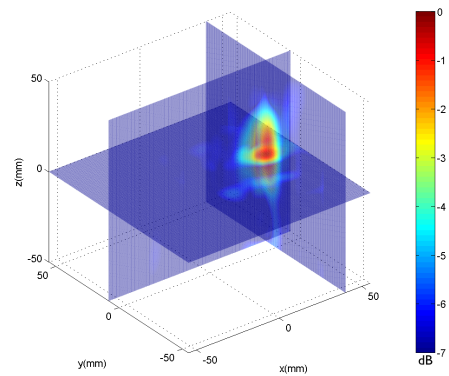
$f = 2.5\text{GHz}$



$f = 3.0\text{GHz}$

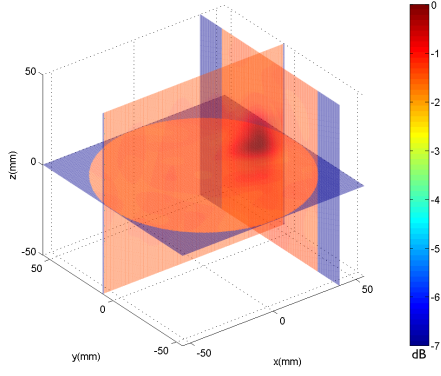


WB-MUSIC

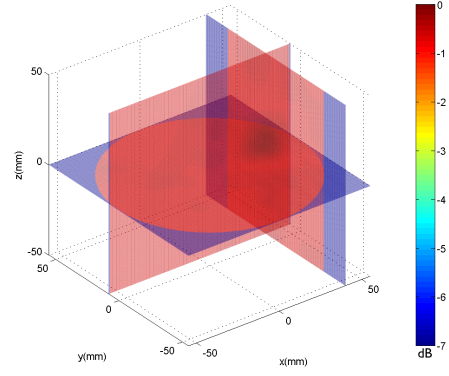


I-MUSIC

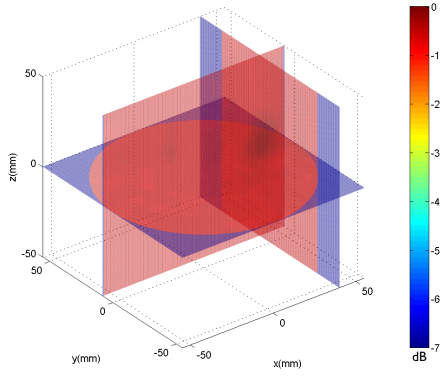
Fig.56: *Orthogonal-plane view of the tomographic-superposition reconstruction method in the homogeneous breast-phantom with “Glassburger” insert: slices have been taken in the estimated source position  $[40, 8, 0]\text{mm}$ .*



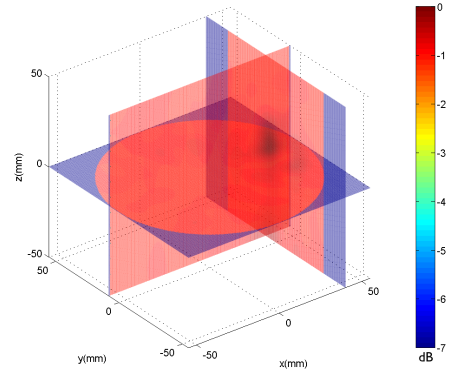
$f = 2.1\text{GHz}$



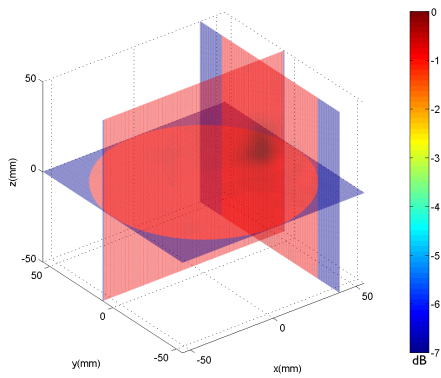
$f = 2.3\text{GHz}$



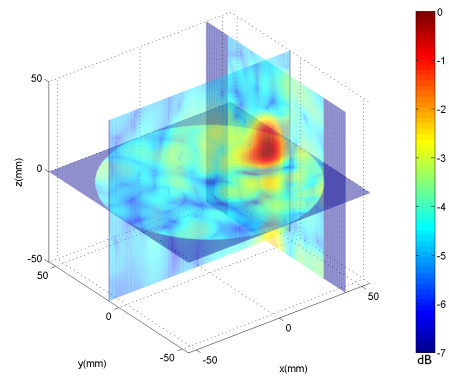
$f = 2.5\text{GHz}$



$f = 3.0\text{GHz}$



WB-MUSIC



I-MUSIC

Fig.57: *Orthogonal-plane view of the multi-elevation reconstruction method in the homogeneous breast-phantom with “Glassburger” insert: slices have been taken in the estimated source position  $[40, 8, 0]\text{mm}$ .*

	Image Type	Spatial Metrics(mm)					Contrast Metrics(dB)		p-val
		Rx	Ry	Rz	AD	AR	SCR	SMR	
TS	2.1GHz	14,7±1,2	11,8±1,6	38,3±5,2	3,6±1,1	21,1±2,7	2,1±1,3	1,6±1,0	0,86
	2.3GHz	12,8±4,6	10,2±1,7	35,9±12,8	6,7±2,0	20,1±6,3	2,2±0,9	1,6±0,7	0,87
	2.5GHz	14,0±6,3	11,8±2,4	29,1±13,1	4,9±1,5	17,1±7,2	2,6±0,9	1,9±0,7	0,84
	3.0GHz	11,7±6,3	7,9±2,6	30,1±16,2	4,0±1,0	16,1±8,4	2,9±1,3	2,1±1,0	0,84
	WB	13,4±1,8	10,1±1,6	32,4±5,0	3,4±1,0	19,0±2,8	2,0±0,1	1,4±0,1	0,85
	I	24,0±4,6	18,4±0,9	45,1±8,7	3,4±1,4	29,8±4,7	5,1±1,3	2,2±0,6	0,86
ME	2.1GHz	25,5±2,1	19,2±2,6	15,5±2,1	1,4±0,4	20,0±2,3	0,7±0,4	0,6±0,4	0,84
	2.3GHz	21,4±7,6	15,2±2,5	20,4±7,2	4,0±1,2	18,8±5,8	0,3±0,1	0,2±0,1	0,84
	2.5GHz	25,9±11,6	20,3±4,1	20,6±9,2	6,9±2,1	22,2±8,3	0,2±0,1	0,2±0,1	0,85
	3.0GHz	15,4±8,3	11,3±3,7	23,9±12,9	3,4±1,0	16,7±8,3	0,5±0,3	0,4±0,2	0,85
	WB	20,4±2,8	13,7±2,1	21,9±3,4	2,7±0,8	18,7±2,8	0,4±0,1	0,3±0,1	0,84
	I	53,6±10,3	34,5±1,7	30,5±5,9	6,4±2,6	40,3±5,9	2,8±0,7	0,7±0,2	0,83

**Tab.7:** *Reconstruction results of the homogeneous breast model with glass insert for tomographic-superposition (TS) and multi-elevation(ME) algorithms.*

Visual and numerical results show that, even in presence of very low dielectric contrast offered by the object and large imaging-planes spacing ( $\sim 25\text{mm}$ ), multi-elevation algorithm is able to properly reconstruct the object and maintain vertical resolution capability at all frequencies; observed contrast performance is much lower than the tomographic superposition method and, also, vertical resolution becomes quite comparable to tomographic method at higher frequencies due to the presence of large uncertainties (Fig.57). The resolution performance relative to horizontal directions are substantially higher for TS, even if also in this case a partial superposition occurs at high frequencies, and as a result the average resolution values at different frequencies are fully comparable for the different methods; it's particularly noticeable the loss in horizontal resolution for the I-MUSIC recombination method in the multi-elevation case.

Obtained results are in accordance with the ones derived for the simulated homogeneous breast model, although we observe a net difference between contrast metrics resulting values for tomographic superposition and multi-elevation algorithms in presence of low  $\epsilon_r$  insert. In particular, the contrast metrics values obtained trend can be judiciously compared to the one previously obtained for the tumor in internal position (case II) for the homogeneous virtual breast-model, where the multi-elevation performance were at most equal to the tomographic superposition one, but with a way more accentuated distance between relative values for the different methods.

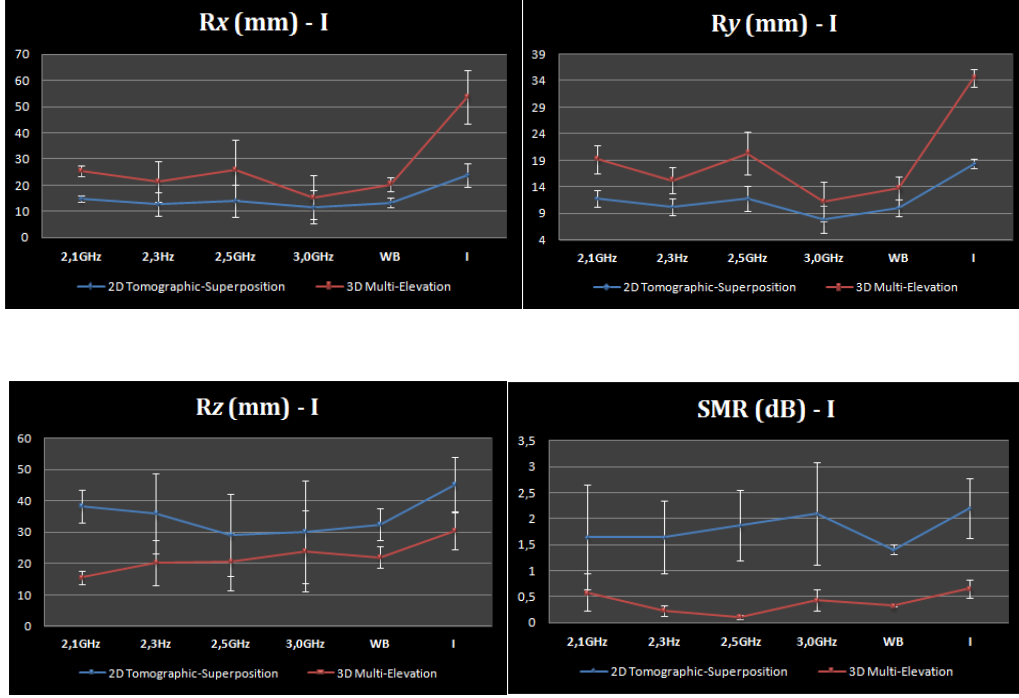


Fig.58: Comparative line graphs of contrast resulting metrics for tomographic-superposition and multi-elevation reconstruction methods in the homogeneous breast phantom reconstruction with glass insert.

## 4.4 Heterogeneous Breast Phantom Reconstruction

During the second experience we have utilized a lesser eccentric cylinder filled with an an emulsion of oil and acetone ( $\epsilon_r^F = 5$ ) to recreate a localized, extended region of different permittivity inside the phantom and thus simulate the presence of a fibroglandular region inside the homogeneous breast-phantom ( $\epsilon_r^B = 2.5$ ).

The fibroglandular region presents a radius of  $\epsilon_r^F = 25\text{mm}$  and is centered at a distance of 20mm from the breast-phantom center.

We have exploited the previously presented PATROCLO insert ( $\epsilon_r^P = 47$ ) to realize two different image reconstructions: in the first one the insert is put outside the fibroglandular region, at a radial distance of 40mm respect to the breast center, and in the second one insert is completely enclosed by the heterogeneous region at a radial distance of 30mm.



#### 4.4.1 Insert in the External Position

For this part, we have exploited a particular grid-configuration where the resulting reconstructed image is not symmetric respect to tumor plane. Imaging planes are localized in a vertical range  $z \in [-15, 45]$ mm, where the tumor occupies the plane in  $z = 0$ , and we have obtained signal in this imaging range with a vertical spacing of 15mm, for a total of 5 heights; the estimated location of the insert is  $\mathbf{r}_{external}^P = [40, 0, 0]$ mm.

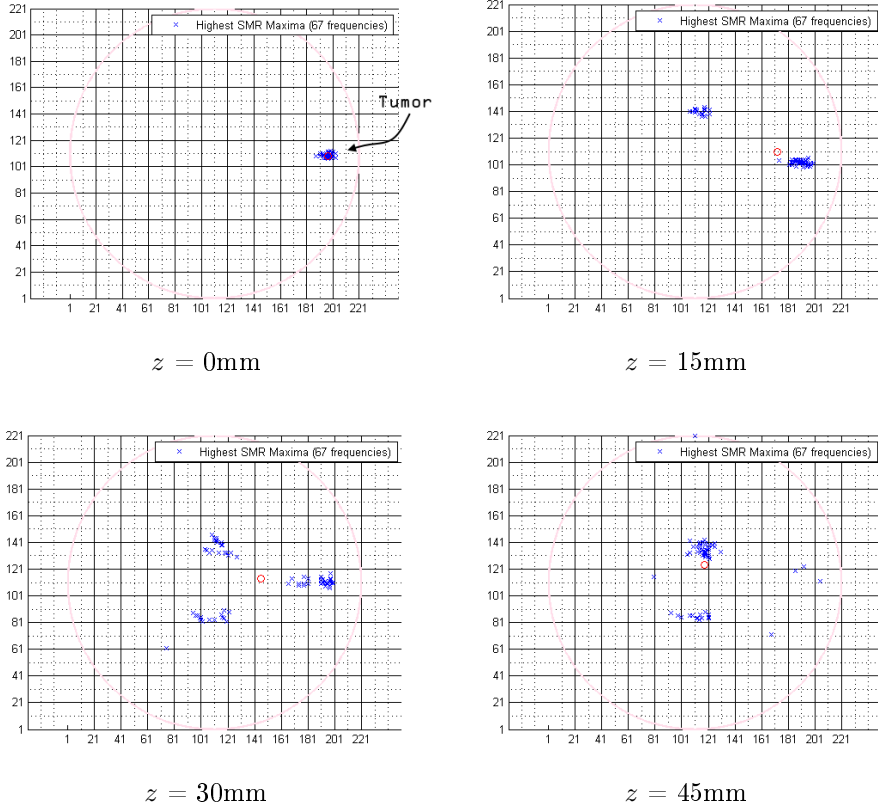


Fig.59: *Clustering maps of the imaging scenario for the insert in external position at different heights in the frequency working range  $[2.0, 3.0]$ GHz. Coordinates are in image pixels.*

Clustering maps (Fig.59) in the  $(2.0 - 3.0)$ GHz range show that the tumor, which can be located in the right part of the imaging domain, is well visible when antenna is positioned on its plane ( $z = 0$ mm) and the pseudospectrum peaks at different frequencies tend to cluster near its actual position for all the frequencies in the working range; by increasingly going farther from tumor plane, the relative cluster spreads gradually and,

when the antenna elevation is too distant, major clustering is associated to the fibroglandular region.

We have exploited the frequencies with maximum SMR values, associated to the clustering of maxima on tumor plane, in the frequency working range [2.0, 3.0]GHz, from all the available data sets (3 for each height are collected):

$$\mathbf{f} = [2.0, 2.1, 2.2, 2.6, 2.7]\text{GHz} .$$

By means of the multi-elevation and tomographic-superposition methods we have derived the following reconstruction results for the external insert.

	Image Type	Spatial Metrics(mm)					Contrast Metrics(dB)		p-val
		Rx	Ry	Rz	AD	AR	SCR	SMR	
TS	2,0GHz	13,4±0,7	12,5±0,1	36,9±2,0	7,5±2,3	20,5±0,9	2,8±0,2	2,8±0,2	0,71
	2,1GHz	15,1±0,5	12,0±0,1	41,8±1,2	5,2±1,6	21,8±0,6	2,2±0,4	2,3±0,4	0,76
	2,2GHz	14,0±0,2	11,4±0,5	70,4±1,4	5,9±1,8	31,7±0,7	1,9±0,1	1,7±0,1	0,81
	2,6GHz	13,9±4,8	10,4±0,4	52,0±18,1	3,8±1,1	24,8±5,9	2,4±0,1	2,1±0,1	0,79
	2,7GHz	18,4±9,7	10,3±0,4	48,9±25,7	3,5±1,1	25,2±9,4	2,1±0,5	1,6±0,4	0,80
	WB	15,4±0,2	10,8±0,1	40,9±0,5	5,1±1,5	21,3±0,3	2,4±0,1	2,0±0,1	0,78
	I	24,9±0,3	20,4±0,6	62,4±1,3	4±1,6	35,8±0,7	4,3±0,2	2,7±0,1	0,87
ME	2,0GHz	17,0±1,0	13,7±0,1	25,5±0,1	7,7±2,3	18,1±0,4	1,8±0,2	1,6±0,1	0,79
	2,1GHz	17,3±0,5	13,3±0,1	28,9±0,9	5,6±1,7	19,0±0,5	1,4±0,3	1,3±0,2	0,83
	2,2GHz	18,1±0,2	13,8±0,6	37,3±1,5	5,3±1,6	22,0±0,8	0,7±0,1	0,7±0,1	0,79
	2,6GHz	17,9±6,2	10,5±0,4	27,5±9,6	3,7±1,1	18,4±5,4	1,8±0,1	1,7±0,1	0,80
	2,7GHz	22,6±11,9	11,0±0,5	24,8±13,0	3,7±1,1	20,2±8,4	0,7±0,2	0,8±0,2	0,80
	WB	19,4±0,3	12,7±0,1	29,6±0,4	4,9±1,5	20,0±0,3	1,2±0,1	1,1±0,1	0,84
	I	46,0±0,3	22,1±0,7	33,3±1,5	1,6±0,6	32,9±0,8	3,4±0,1	2,4±0,1	0,84

**Tab.8:** *Reconstruction results of the inhomogeneous breast model with the insert outside fibroglandular region for tomographic-superposition (TS) and multi-elevation(ME) algorithms.*

In this case, the vertical resolution performance of the the multi-elevation algorithm appears in an evident way respect to the tomographic-superposition one, because the signal obtained at increasingly distant planes from tumor location is mainly due to fibroglandular region scattering, which contributes to the creation of sparse, vertical artefacts; the formation of clutter areas due to heterogeneity strongly depends on working frequency, so these artefacts can be moderately corrected by employing multi-frequency recombination methods.

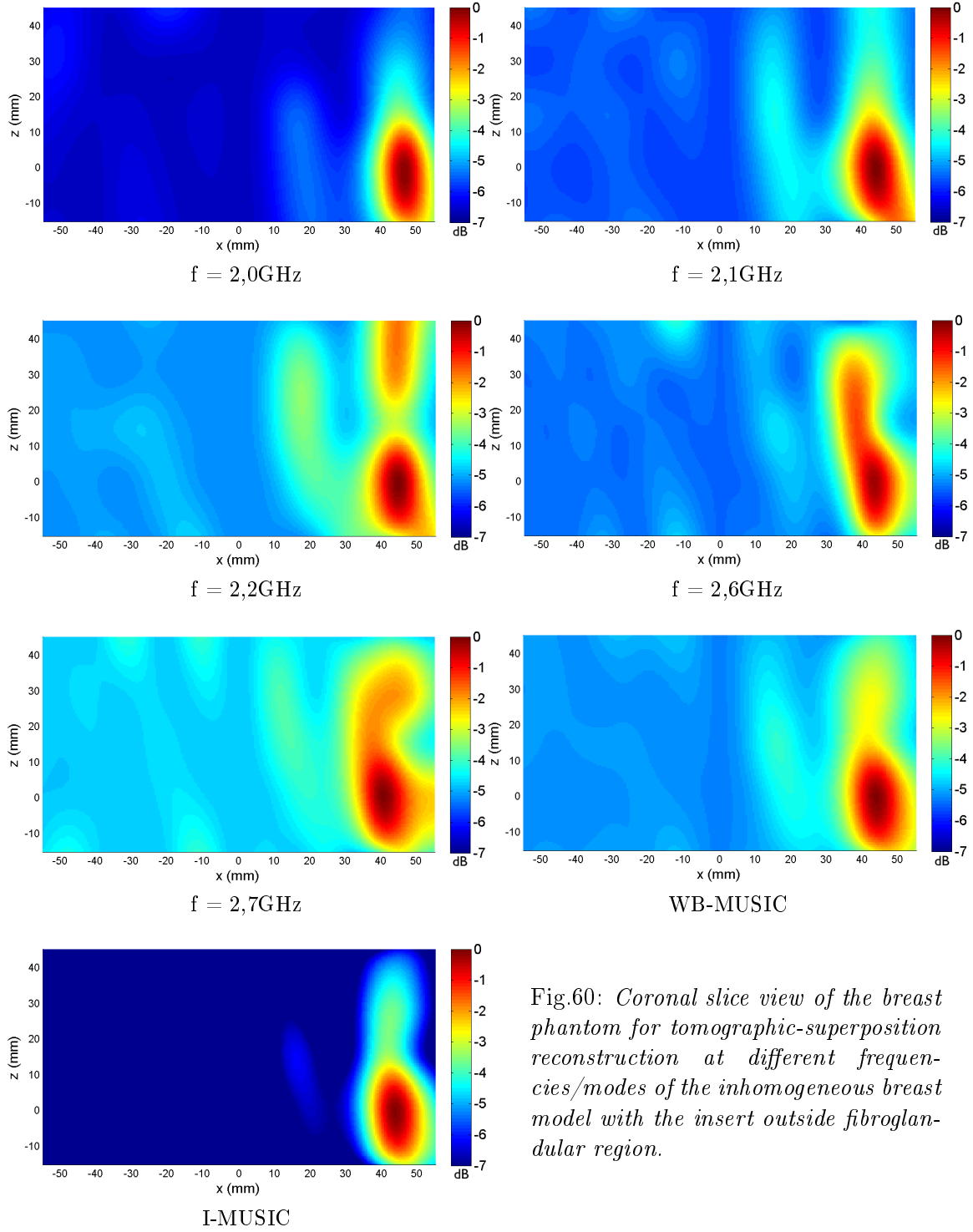


Fig.60: *Coronal slice view of the breast phantom for tomographic-superposition reconstruction at different frequencies/modes of the inhomogeneous breast model with the insert outside fibroglandular region.*

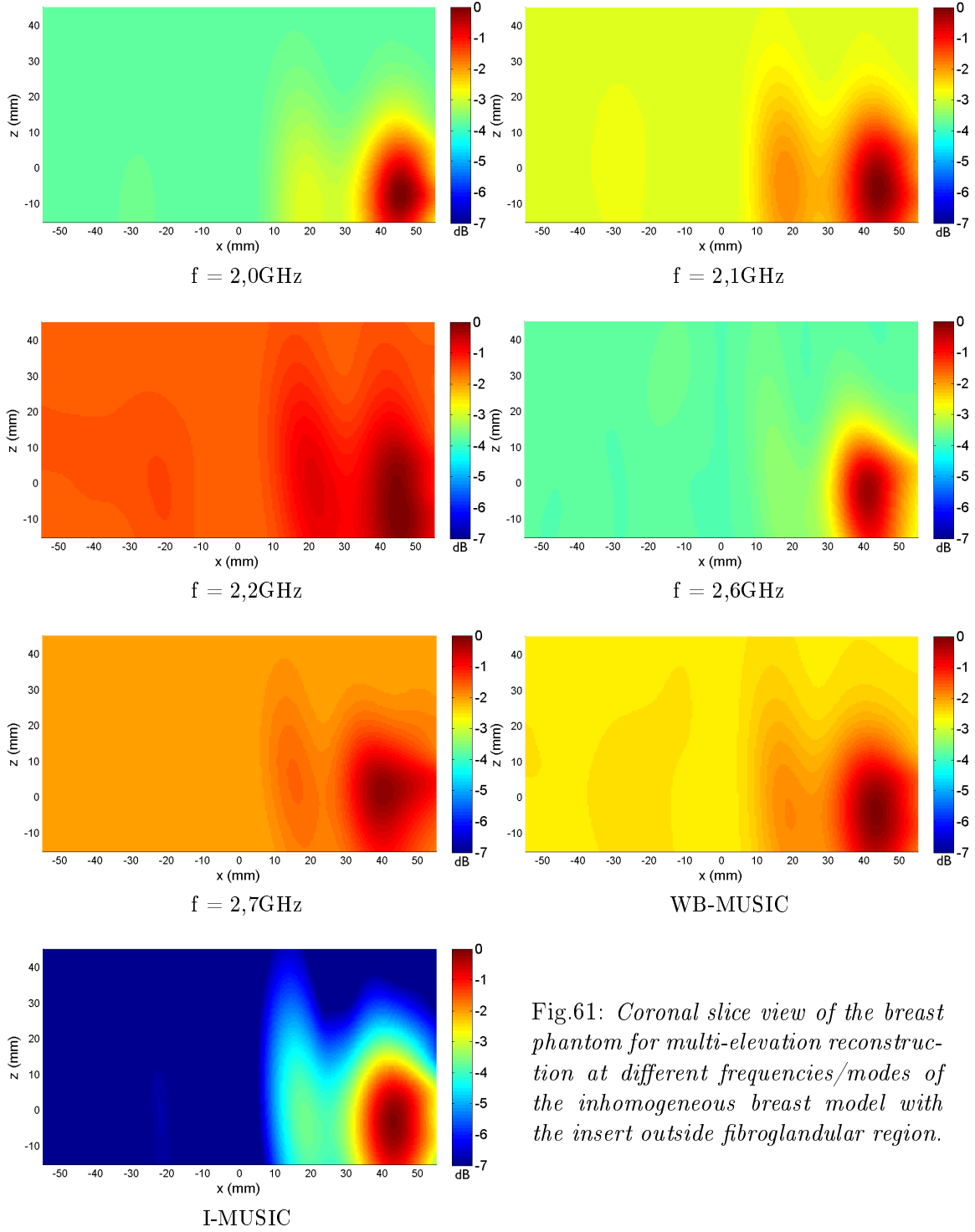


Fig.61: *Coronal slice view of the breast phantom for multi-elevation reconstruction at different frequencies/modes of the inhomogeneous breast model with the insert outside fibroglandular region.*



Fig.62: *Comparative line graphs of contrast resulting metrics for tomographic-superposition and multi-elevation reconstruction methods in the inhomogeneous breast phantom reconstruction with external insert.*

As for the experimental homogeneous case, we observe an overall inferior contrast performance by the multi-elevation algorithm respect to the tomographic-superposition one, though in this case the difference between SMR trends are far less accentuated due to the presence of a stronger scatterer ( $\varepsilon_r^P = 47$ ) respect to the glass one ( $\varepsilon_r^G = 5$ ) previously employed. Resolution performance is this time way more consistent with results obtained during simulations, and we see that horizontal resolution values become in some cases fully comparable between different methods, while vertical resolution is superior in the multi-elevation case.

#### 4.4.2 Insert in the Internal Position

In the final part of experience, the insert has been located inside the fibroglandular region by the aluminium cap internal hole positioned in  $\mathbf{r}_{internal}^P = [30, 0, 0]\text{mm}$ . This time, we exploited a symmetrical vertical-grid disposition in the range  $z \in [-30, 30]\text{mm}$  and with a step of 15mm, for a total of 5 acquisition planes. Differently from the external

insert case, it was more difficult to locate the actual tumor position with the frequency selection working interface (Fig.63), mainly because in this case the principal clustering is always seen in correspondence of the fibroglandular region (also in  $z = 0$ ). We also found that the tumor location is shifted respect to the  $x$ -axis by a noticeable amount, possibly due to the not entirely controllable direction of the string when immersed, but the radial distance respect to phantom-center is approximately correct.

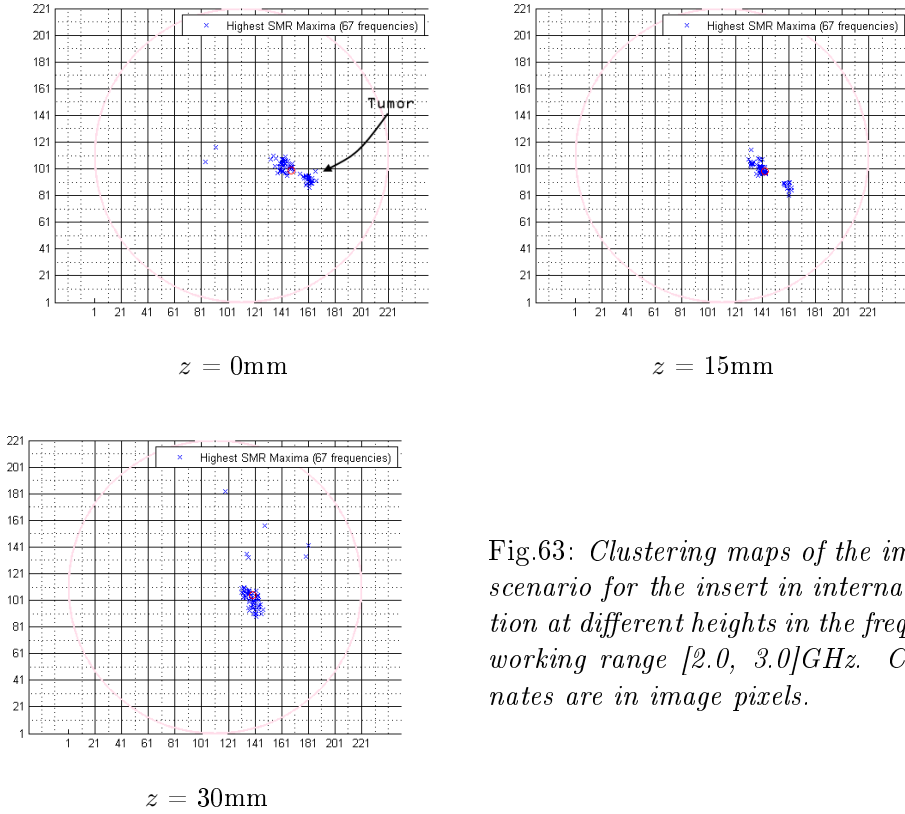


Fig.63: *Clustering maps of the imaging scenario for the insert in internal position at different heights in the frequency working range  $[2.0, 3.0]\text{GHz}$ . Coordinates are in image pixels.*

This time we found that the insert could be well-seen from 2D-reconstructions with a consistent SMR value only in a very limited range of frequencies close to 3.0GHz, so we have reconstructed the imaging volume with just two of the highest-SMR frequencies associated to the tumor cluster:

$$\mathbf{f} = [2.9, 3.0]\text{GHz}.$$

In the following, we report reconstruction results with ME and TS algorithms for the single-frequency cases.

	Image Type	Spatial Metrics(mm)					Contrast Metrics(dB)		p-val
		Rx	Ry	Rz	AD	AR	SCR	SMR	
TS	2.9GHz	13 $\pm$ 1,4	9,5 $\pm$ 0,5	30,0 $\pm$ 3,2	12,9 $\pm$ 3,9	16,7 $\pm$ 1,7	2,1 $\pm$ 0,4	1,7 $\pm$ 0,3	0,66
	3.0GHz	12,3 $\pm$ 1,3	9,6 $\pm$ 0,3	35,9 $\pm$ 3,8	11,5 $\pm$ 3,3	18,2 $\pm$ 1,8	2,3 $\pm$ 0,6	1,9 $\pm$ 0,5	0,66
ME	2.9GHz	37,9 $\pm$ 4,0	19,6 $\pm$ 1,0	27,6 $\pm$ 2,9	14,0 $\pm$ 4,2	26,8 $\pm$ 2,3	0,5 $\pm$ 0,1	0,2 $\pm$ 0,1	0,66
	3.0GHz	15,4 $\pm$ 1,6	10,8 $\pm$ 0,4	29,4 $\pm$ 3,1	19,8 $\pm$ 5,7	17,3 $\pm$ 1,6	0,7 $\pm$ 0,2	0,6 $\pm$ 0,2	0,65

**Tab.9:** Reconstruction results of the inhomogeneous breast model with the insert embedded in the fibroglandular region for tomographic-superposition (TS) and multi-elevation(ME) algorithms.

It can be seen that the vertical resolution improvement offered by ME is, in case, almost negligible, at the cost of a noticeably worse SMR and reduced horizontal resolution capability respect to TS method.

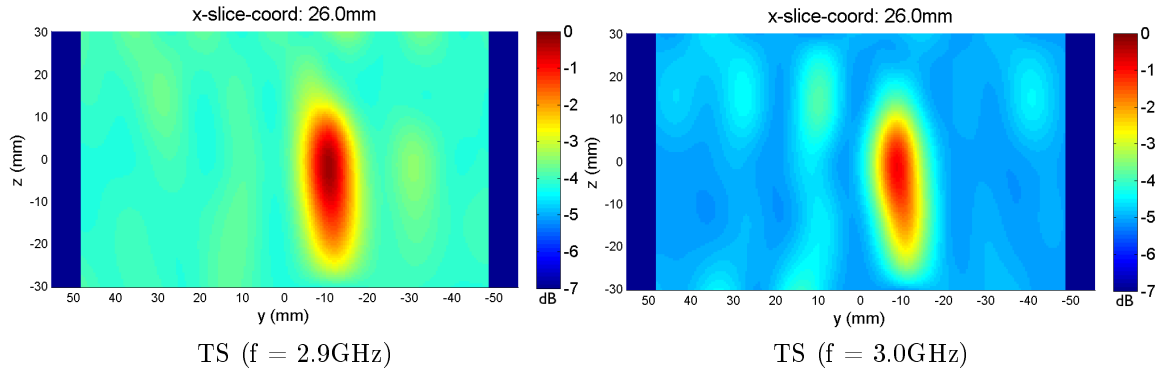
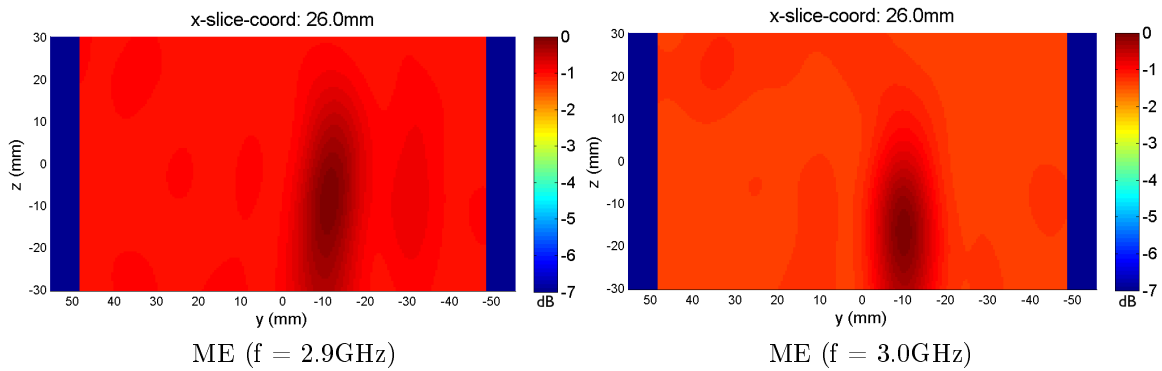


Fig.65: Sagittal slice view for TS and ME reconstruction methods for the inhomogeneous breast model with the insert inside fibroglandular region. Slice has been taken in  $x = 26\text{mm}$ .



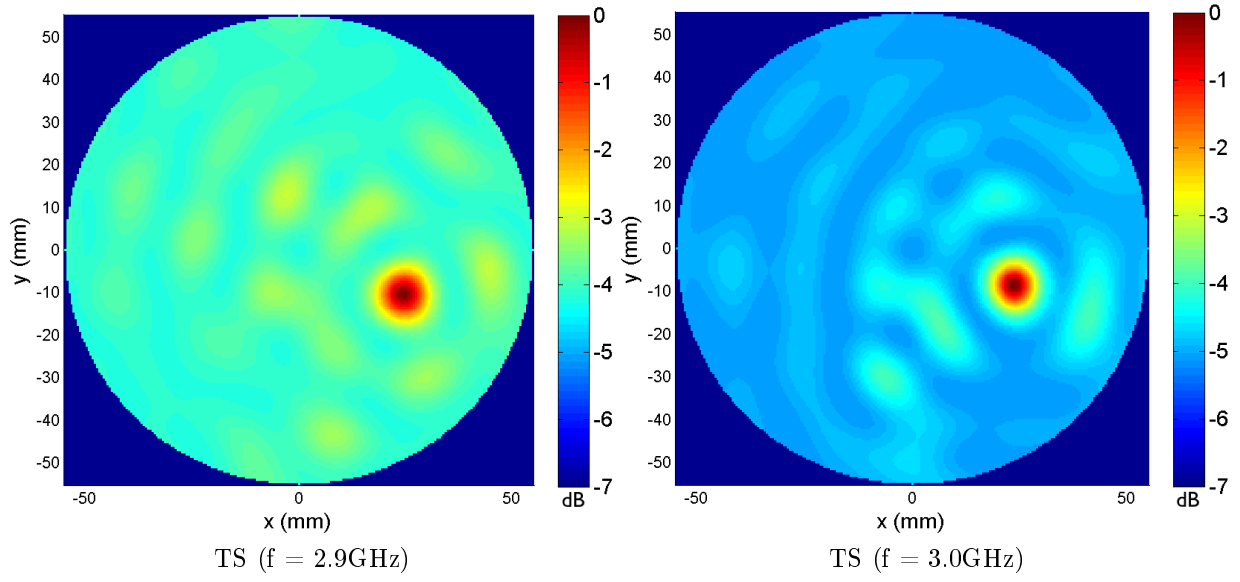
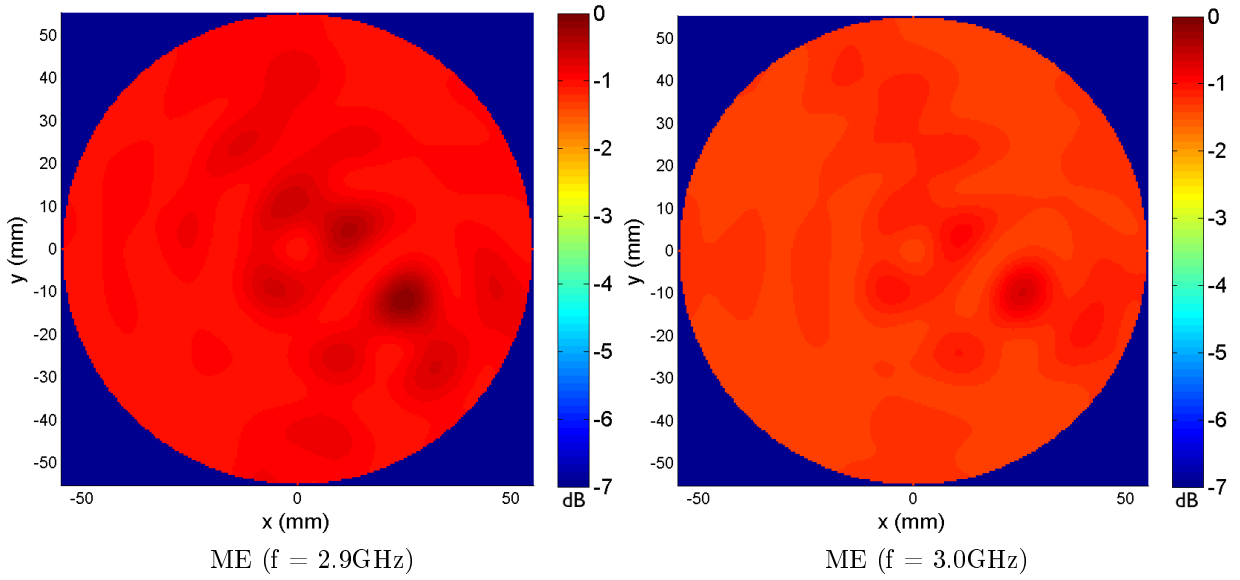


Fig.64: *Transverse slice view for TS and ME reconstruction methods for the inhomogeneous breast model with the insert inside fibroglandular region.*





# Chapter 5

## Conclusions

While addressing the problem of breast imaging by means of microwave radiation, it was developed a tomographic 3D-reconstruction algorithm belonging to the class of the linear inversion methods. This multi-elevation technique reconstructs the image-pseudospectrum by computing the correlation term for the measured signal vector, obtainable for an arbitrary number of antenna positions and elevations outside imaging domain, and the monostatic response vector which, in this case, was obtained by utilizing the 3D-Green's propagator function for the Hertzian dipole in scalar approximation. The implemented method has been preliminarily tested in a virtually simulated environment; performance results for investigated cases, which include the imaging of a scattering source located inside a homogeneous and inhomogeneous breast model, have shown interesting results, especially from the point of view of vertical resolution capability. While performing tests on simulated data, in fact, multi-elevation algorithm has been compared against a tomographic-superposition reconstruction technique, which performs volumetric reconstruction by means of interpolation methods, and the obtained results have shown that the proposed method outperforms tomographic-superposition in terms of vertical object resolution. This characteristic has been tested and verified for different scenario conditions which include, among the others, the utilization of an increased spacing for the antenna imaging grid in multi-elevation. Experimental results on simulated data-sets also show that the horizontal resolution and contrast performance of multi-elevation method is, in general, slightly inferior or at most comparable to the tomographic-superposition case.

We have ultimately verified the reconstruction performance outcome of proposed algorithm for real-data acquired at the microwave imaging laboratory; tests have been again performed for various scenario conditions, which mainly included the ones already encountered during simulations.

Algorithm has generally shown to preserve the characteristic vertical resolution capability for all the experimental tests. However, due to the noticeable increase in the level of uncertainty typical of experimental conditions, values become in some cases not distant

from the ones obtained with tomographic-superposition method; we also noticed how the expected contrast performance of multi-elevation algorithm is critically reduced during the tests involving real-data reconstruction, thus introducing an actual, important tradeoff between the achievable contrast and vertical resolution capability.

Due to the computational effort required in order to perform volumetric reconstruction, we chose to focus our analysis on specific cases for a limited number of frequencies. Future works should address the possibility of testing 3D-reconstruction on a broader frequency range and in more complex scenario conditions.

Finally, proper extension of the method to multistatic antenna configuration, in concomitance with the implementation of multi-channel filtering techniques, can possibly give place to an overall improved imaging technique.

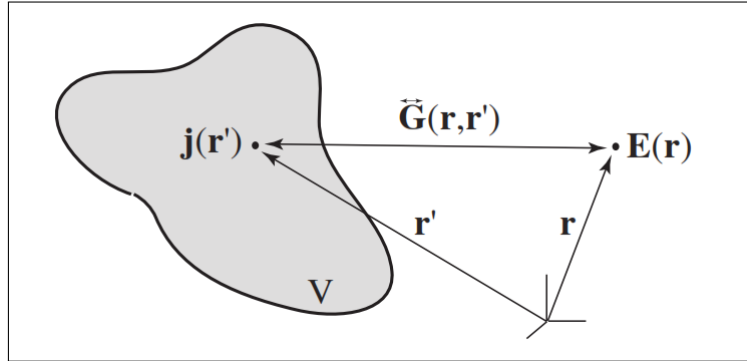
# Appendices

## A) Green's Functions

In field theory, Green's functions can be defined as the fields due to a point source. In electromagnetic theory, we use dyadic Green's function, which is defined by the electric field  $\mathbf{E}$  at the fieldpoint  $\mathbf{r}$  generated by a radiating electric dipole  $\mathbf{p}$  located at the source point  $\mathbf{r}'$  :

$$\mathbf{E}(\mathbf{r}) = \omega^2 \mu_0 \mu \vec{\mathbf{G}}(\mathbf{r}, \mathbf{r}') \mathbf{p}(\mathbf{r}') ,$$

where  $\vec{\mathbf{G}}$  is the dyadic Green's function.



*Scheme of electric field generated by a point source.*

The Green's function renders the electric field  $\mathbf{E}$  at the field point  $\mathbf{r}$  due to a single point source  $\mathbf{j}$  located at  $\mathbf{r}'$ . The Green's tensor  $\vec{\mathbf{G}}$  accounts for all the possible orientations of  $\mathbf{j}$  respect to  $\mathbf{r}$ .

## Mathematical basis of Green's functions

Consider the general, inhomogeneous equation

$$\mathcal{L} \mathbf{A}(\mathbf{r}) = \mathbf{B}(\mathbf{r}) ,$$

where  $\mathcal{L}$  is a linear operator acting on vectorfield  $\mathbf{A}$ , which represents the unknown response of the physical system, and  $\mathbf{B}$  is the vector field associated to the known source

function and makes the differential equation inhomogeneous. The corresponding general solution is equal to the sum of the complete homogeneous solution ( $\mathbf{B} = 0$ ) and a particular, inhomogeneous solution; we assume that the homogeneous solution ( $\mathbf{A}_0$ ) is known.

To solve for the particular solution, we consider the special inhomogeneity  $\delta(\mathbf{r} - \mathbf{r}')$ , which is zero everywhere except for  $\mathbf{r} = \mathbf{r}'$ . We rewrite the previous linear equation as

$$\mathcal{L} \mathbf{G}_i(\mathbf{r}, \mathbf{r}') = \mathbf{n}_i \delta(\mathbf{r} - \mathbf{r}') \quad (i = x, y, z) ,$$

where  $\mathbf{n}_i$  denotes an arbitrary constant unit vector. These three equations can further be expressed in the following closed form:

$$\mathcal{L} \overset{\leftrightarrow}{\mathbf{G}}(\mathbf{r}, \mathbf{r}') = \overset{\leftrightarrow}{\mathbf{I}} \delta(\mathbf{r} - \mathbf{r}') .$$

Here,  $\overset{\leftrightarrow}{\mathbf{G}}$  is the dyadic Green's function and  $\overset{\leftrightarrow}{\mathbf{I}}$  is the unit dyad. If we solve the previous closed form equation, so that  $\overset{\leftrightarrow}{\mathbf{G}}$  is known, we can find the solution to the initial inhomogeneous equation by first multiplying the closed form equation with  $\mathbf{B}(\mathbf{r}')$  on both sides and integrating over the volume  $V$  where  $\mathbf{B} \neq 0$  :

$$\int_V \mathcal{L} \overset{\leftrightarrow}{\mathbf{G}}(\mathbf{r}, \mathbf{r}') \mathbf{B}(\mathbf{r}') dV' = \int_V \mathbf{B}(\mathbf{r}') \delta(\mathbf{r} - \mathbf{r}') dV' .$$

Then, we notice that the right hand side of equation reduces to  $\mathbf{B}(\mathbf{r})$  and, since we have initially defined  $[\mathcal{L} \mathbf{A}(\mathbf{r}) = \mathbf{B}(\mathbf{r})]$ , we obtain

$$\mathcal{L} \mathbf{A}(\mathbf{r}) = \int_V \mathcal{L} \overset{\leftrightarrow}{\mathbf{G}}(\mathbf{r}, \mathbf{r}') \mathbf{B}(\mathbf{r}') dV' = \mathcal{L} \int_V \overset{\leftrightarrow}{\mathbf{G}}(\mathbf{r}, \mathbf{r}') \mathbf{B}(\mathbf{r}') dV' .$$

In the very last step, the linear operator is taken out of the integral sign: the assumption that the operators  $\mathcal{L}$  and  $\int dV'$  can be interchanged is not strictly valid and special care must be applied if the integrand is not well behaved. For example, if  $\overset{\leftrightarrow}{\mathbf{G}}(\mathbf{r}, \mathbf{r}')$  is singular at  $\mathbf{r} = \mathbf{r}'$  we have to introduce an infinitesimal exclusion volume surrounding the singularity.

Supposing we can legitimately perform this latest operator extraction from integral sign, the solution of the general inhomogeneous equation can be expressed as

$$\mathbf{A}(\mathbf{r}) = \int_V \overset{\leftrightarrow}{\mathbf{G}}(\mathbf{r}, \mathbf{r}') \mathbf{B}(\mathbf{r}') dV' ,$$

so it can be finally found by integrating the product of the dyadic Green's function and the inhomogeneity  $\mathbf{B}$  over the source volume  $V$ .

## Green's function derivation for the electric field

We start by expressing the electric field  $\mathbf{E}$  and the magnetic field  $\mathbf{H}$  as functions of the time-harmonic vector potential  $\mathbf{A}$  and the scalar potential  $\phi$  in an infinite and homogeneous space characterized by the constants  $\varepsilon$  and  $\mu$ :

$$\mathbf{E}(\mathbf{r}) = i\omega\mathbf{A}(\mathbf{r}) - \nabla\phi(\mathbf{r})$$

$$\mathbf{H}(\mathbf{r}) = \frac{1}{\mu_0\mu}\nabla \times \mathbf{A}(\mathbf{r}) .$$

In differential form and SI units, the macroscopic Maxwell's equations read as

$$\left. \begin{aligned} \nabla \times \mathbf{E}(\mathbf{r}, t) &= -\frac{\partial \mathbf{B}(\mathbf{r}, t)}{\partial t} \\ \nabla \times \mathbf{H}(\mathbf{r}, t) &= \frac{\partial \mathbf{D}(\mathbf{r}, t)}{\partial t} + \mathbf{j}(\mathbf{r}, t) \\ \nabla \cdot \mathbf{D}(\mathbf{r}, t) &= \rho(\mathbf{r}, t) \\ \nabla \cdot \mathbf{B}(\mathbf{r}, t) &= 0 . \end{aligned} \right\} \quad \text{Maxwell's Equations in Matter}$$

Here,  $\mathbf{D}$  denotes the electric displacement vector,  $\mathbf{B}$  the magnetic induction vector,  $\mathbf{j}$  the current density and  $\rho$  the charge density.

By making use of the constitutive relation for electric displacement

$$\mathbf{D} = \varepsilon_0\varepsilon\mathbf{E} ,$$

we can insert the expressions for time-harmonic vector and scalar potentials into the second Maxwell equation, obtaining

$$\nabla \times \nabla \times \mathbf{A}(\mathbf{r}) = \mu_0\mu\mathbf{j}(\mathbf{r}) - i\omega\mu_0\mu\varepsilon_0\varepsilon[i\omega\mathbf{A}(\mathbf{r}) - \nabla\phi(\mathbf{r})] .$$

Now, by choosing the Lorenz gauge

$$\nabla \cdot \mathbf{A}(\mathbf{r}) = i\omega\mu_0\mu\varepsilon_0\varepsilon \phi(\mathbf{r})$$

and by applying the mathematical identity ' $\nabla \times \nabla = -\nabla^2 + \nabla \nabla \cdot$ ' together with the gauge condition, we can finally rewrite the second Maxwell equation into the inhomogeneous Helmholtz equation,

$$[\nabla^2 + k^2]\mathbf{A}(\mathbf{r}) = -\mu_0\mu\mathbf{j}(\mathbf{r}) ,$$

where  $k = (\omega/c)\sqrt{\mu\varepsilon}$  is the wavenumber. The equation holds independently for each component  $A_i$  of  $\mathbf{A}$ .

We can find a similar equation for the time-harmonic scalar potential,

$$[\nabla^2 + k^2]\phi(\mathbf{r}) = -\frac{\rho(\mathbf{r})}{\varepsilon_0\varepsilon} .$$

Thus, we have a set of four scalar Helmholtz equations whose general form is

$$[\nabla^2 + k^2]f(\mathbf{r}) = -g(\mathbf{r}) .$$

If we have the source term  $g(\mathbf{r})$  replaced by a single point source  $\delta(\mathbf{r} - \mathbf{r}')$ , we obtain the *scalar Green's function* ( $G_0$ ) for the Helmholtz equation,

$$[\nabla^2 + k^2]G_0(\mathbf{r}) = -\delta(\mathbf{r} - \mathbf{r}') ,$$

where the vector  $\mathbf{r}$  denotes the location at which we are evaluating the fields, and  $\mathbf{r}'$  indicates the position of the point-source.

After having determined  $G_0$ , we can solve the integral equations for scalar and vector potentials:

$$\begin{aligned} \mathbf{A}(\mathbf{r}) &= \mu_0\mu \int_V \mathbf{j}(\mathbf{r}')G_0(\mathbf{r}, \mathbf{r}') dV' \\ \phi(\mathbf{r}) &= \frac{1}{\varepsilon_0\varepsilon} \int_V \rho(\mathbf{r}')G_0(\mathbf{r}, \mathbf{r}') dV' . \end{aligned}$$

The free-space, scalar Green's function, applicable in case we consider a homogeneous three-dimensional space, has the form

$$G_0(\mathbf{r}, \mathbf{r}') = \frac{e^{\pm ik|\mathbf{r}-\mathbf{r}'|}}{4\pi|\mathbf{r} - \mathbf{r}'|} . \quad (1)$$

The solution with plus sign denotes a spherical wave travelling outwards from the origin, while minus sign is for a wave propagating inwards to the origin.

While in the case of potentials  $\mathbf{A}$  and  $\phi$  it is possible to reduce Green's functions treatment to scalar equations, since these field components depends strictly from their corresponding source component, in the case of electric and magnetic fields  $\mathbf{E}, \mathbf{H}$  each source component is related to *every* component of the field thus we shall work with a *dyadic Green's function*, which is a tensor.

By substituting the linear constitutive equations

$$\mathbf{D} = \varepsilon_0\varepsilon\mathbf{E} , \quad \mathbf{B} = \mu_0\mu\mathbf{H}$$

into the Maxwell's curl equations for the time-harmonic fields

$$\left. \begin{aligned} \nabla \times \mathbf{E}(\mathbf{r}) &= i\omega \mathbf{B}(\mathbf{r}) \\ \nabla \times \mathbf{H}(\mathbf{r}) &= -i\omega \mathbf{D}(\mathbf{r}) + \mathbf{j}(\mathbf{r}) \\ \nabla \cdot \mathbf{D}(\mathbf{r}) &= \rho(\mathbf{r}) \\ \nabla \cdot \mathbf{B}(\mathbf{r}) &= 0 \end{aligned} \right\} \quad \text{Time-Harmonic Maxwell's Equations}$$

we obtain the *vector wave equations* for the complex fields  $\mathbf{E}(\mathbf{r})$ ,  $\mathbf{H}(\mathbf{r})$  in homogeneous space:

$$\begin{aligned} \nabla \times \nabla \times \mathbf{E}(\mathbf{r}) - k^2 \mathbf{E}(\mathbf{r}) &= i\omega\mu_0\mu \mathbf{j}(\mathbf{r}) \\ \nabla \times \nabla \times \mathbf{H}(\mathbf{r}) - k^2 \mathbf{H}(\mathbf{r}) &= \nabla \times \mathbf{j}(\mathbf{r}) . \end{aligned}$$

These can also be rewritten as the inhomogeneous vector Helmholtz equations<sup>1</sup>:

$$\begin{aligned} (\nabla^2 + k^2)\mathbf{E}(\mathbf{r}) &= -i\omega\mu_0\mu \mathbf{j}(\mathbf{r}) + \frac{\nabla\rho(\mathbf{r})}{\varepsilon_0\varepsilon} \\ (\nabla^2 + k^2)\mathbf{H}(\mathbf{r}) &= -\nabla \times \mathbf{j}(\mathbf{r}) . \end{aligned}$$

Now, considering the wave-equation for the electric field, we want to write a general definition of the dyadic Green's function such that, for every component of the source current  $\mathbf{j}$ , exists a Green's vector which describes how that source component radiation propagates in three-dimensional space. Thus, we define three different Green's vector functions for  $j_x, j_y, j_z$  :

$$\begin{aligned} \nabla \times \nabla \times \mathbf{G}_x(\mathbf{r}, \mathbf{r}') - k^2 \mathbf{G}_x(\mathbf{r}, \mathbf{r}') &= \delta(\mathbf{r} - \mathbf{r}') \mathbf{n}_x \\ \nabla \times \nabla \times \mathbf{G}_y(\mathbf{r}, \mathbf{r}') - k^2 \mathbf{G}_y(\mathbf{r}, \mathbf{r}') &= \delta(\mathbf{r} - \mathbf{r}') \mathbf{n}_y \\ \nabla \times \nabla \times \mathbf{G}_z(\mathbf{r}, \mathbf{r}') - k^2 \mathbf{G}_z(\mathbf{r}, \mathbf{r}') &= \delta(\mathbf{r} - \mathbf{r}') \mathbf{n}_z . \end{aligned}$$

Here, the unit vectors  $\mathbf{n}_x, \mathbf{n}_y, \mathbf{n}_z$  are referred to a point-source in the  $x, y, z$  direction respectively.

In order to account for all orientations, we rewrite the previous equations into a compact notation for the three vectorial Green's functions,

$$\nabla \times \nabla \times \vec{\mathbf{G}}(\mathbf{r}, \mathbf{r}') - k^2 \vec{\mathbf{G}}(\mathbf{r}, \mathbf{r}') = \vec{\mathbf{I}} \delta(\mathbf{r} - \mathbf{r}') ,$$

---

<sup>1</sup>Notice the identity ' $\nabla \times \nabla = -\nabla^2 + \nabla \nabla \cdot$ ' was applied.

where  $\vec{\mathbf{I}}$  is the unit tensor or unit dyad,  $\vec{\mathbf{G}}$  is the dyadic Green's function and each of its columns represents the field due to a point source in the direction specified by the column index.

If we now let the current distribution  $\mathbf{j}$  be a superposition of all the point currents present in the radiating volume, by knowing the dyadic Green's function it is possible to state a *particular* solution for the electric field wave equation as

$$\mathbf{E}(\mathbf{r}) = i\omega\mu_0\mu \int_V \vec{\mathbf{G}}(\mathbf{r}, \mathbf{r}') \mathbf{j}(\mathbf{r}') dV' .$$

A similar equation for the particular solution can be derived for magnetic field  $\mathbf{H}$ , starting from its corresponding wave equation.

Now, the *general* solution of a wave equation is given by the sum of the *homogeneous* solution ( $\mathbf{E}_0, \mathbf{B}_0$ ), which is the field in the absence of current, and the particular solution. The electromagnetic field generated in an unbounded region (free-space radiation) by the impressed source  $\mathbf{j}$ , which satisfies the vector wave equations along with the radiation conditions

$$\left. \begin{aligned} \hat{\mathbf{r}} \times \mathbf{E}(\mathbf{r}) &= \eta \mathbf{H}(\mathbf{r}) + o\left(\frac{1}{|\mathbf{r}|}\right) \\ \mathbf{H}(\mathbf{r}) \times \hat{\mathbf{r}} &= \frac{1}{\eta} \mathbf{E}(\mathbf{r}) + o\left(\frac{1}{|\mathbf{r}|}\right) \end{aligned} \right\} \quad \text{Silver-Müller Radiation Conditions}$$

where  $\hat{\mathbf{r}} = \mathbf{r}/|\mathbf{r}|$  is the unit radial vector and  $\eta = \sqrt{\frac{\mu_0\mu}{\epsilon_0\epsilon}}$  is the intrinsic impedance of the medium, can be expressed in integral form via the following *volume integral equations*:

$$\mathbf{E}(\mathbf{r}) = \mathbf{E}_0(\mathbf{r}) + i\omega\mu_0\mu \int_V \vec{\mathbf{G}}(\mathbf{r}, \mathbf{r}') \mathbf{j}(\mathbf{r}') dV' \quad (\mathbf{r} \notin V)$$

$$\mathbf{H}(\mathbf{r}) = \mathbf{H}_0(\mathbf{r}) + \int_V \left[ \nabla \times \vec{\mathbf{G}}(\mathbf{r}, \mathbf{r}') \right] \mathbf{j}(\mathbf{r}') dV' \quad (\mathbf{r} \notin V) .$$

The validity of the integral equations is limited to the space outside the source volume  $V$ , in order to avoid the singularities of the free-space Green's tensor.

In order to solve the volume integral equations for a given distribution of currents we have to determine the value of the Green's tensor. We can find a general form of the dyadic function by substituting the scalar potential<sup>2</sup>

$$\phi(\mathbf{r}) = -i \frac{\nabla \cdot \mathbf{A}(\mathbf{r})}{\omega\mu_0\mu\epsilon_0\epsilon} ,$$

into the field equation

$$\mathbf{E}(\mathbf{r}) = i\omega\mathbf{A}(\mathbf{r}) - \nabla\phi(\mathbf{r}) ,$$

---

<sup>2</sup>It has been derived from the Lorenz gauge expression:  $\nabla \cdot \mathbf{A}(\mathbf{r}) = i\omega\mu_0\mu\epsilon_0\epsilon \phi(\mathbf{r})$ .



which gives

$$\mathbf{E}(\mathbf{r}) = i\omega \left[ 1 + \frac{1}{k^2} \nabla \nabla \cdot \right] \mathbf{A}(\mathbf{r}) .$$

Now, for how we defined DGF respect to wave equation, such that its column vectors  $\mathbf{G}_x$ ,  $\mathbf{G}_y$ ,  $\mathbf{G}_z$  represent electric field due to a point source current  $\mathbf{j} = (i\omega\mu_0\mu)^{-1} \delta(\mathbf{r} - \mathbf{r}') \mathbf{n}_{(x,y,z)}$  located at  $\mathbf{r}'$  (of corresponding orientation  $\mathbf{n}_x$ ,  $\mathbf{n}_y$ ,  $\mathbf{n}_z$ ), we can write the particular solution of the vector potential  $\mathbf{A}$  as

$$\mathbf{A}(\mathbf{r}) = (i\omega)^{-1} G_0(\mathbf{r}, \mathbf{r}') \mathbf{n}_{(x,y,z)} .$$

By substituting this result in the field equation, we obtain a set of three equations for the vector Green functions,

$$\begin{aligned} \mathbf{G}_x(\mathbf{r}, \mathbf{r}') &= \left[ 1 + \frac{1}{k^2} \nabla \nabla \cdot \right] G_0(\mathbf{r}, \mathbf{r}') \mathbf{n}_x \\ \mathbf{G}_y(\mathbf{r}, \mathbf{r}') &= \left[ 1 + \frac{1}{k^2} \nabla \nabla \cdot \right] G_0(\mathbf{r}, \mathbf{r}') \mathbf{n}_y \\ \mathbf{G}_z(\mathbf{r}, \mathbf{r}') &= \left[ 1 + \frac{1}{k^2} \nabla \nabla \cdot \right] G_0(\mathbf{r}, \mathbf{r}') \mathbf{n}_z , \end{aligned}$$

which can be translated in a single, compact equation for the dyadic Green's function<sup>3</sup>:

$$\vec{\vec{\mathbf{G}}}(\mathbf{r}, \mathbf{r}') = \left[ \vec{\vec{\mathbf{I}}} + \frac{1}{k^2} \nabla \nabla \right] G_0(\mathbf{r}, \mathbf{r}') .$$

## Explicit form of the dyadic Green's tensor

The compact form of the dyadic Green's function can be written in matrix form in the following manner<sup>4</sup>:

$$\vec{\vec{\mathbf{G}}}(\mathbf{r}, \mathbf{r}') = \begin{pmatrix} k^2 + \frac{\partial^2}{\partial x^2} & \frac{\partial^2}{\partial x \partial y} & \frac{\partial^2}{\partial x \partial z} \\ \frac{\partial^2}{\partial y \partial x} & k^2 + \frac{\partial^2}{\partial y^2} & \frac{\partial^2}{\partial y \partial z} \\ \frac{\partial^2}{\partial z \partial x} & \frac{\partial^2}{\partial z \partial y} & k^2 + \frac{\partial^2}{\partial z^2} \end{pmatrix} \frac{e^{\pm i k |\mathbf{r} - \mathbf{r}'|}}{4\pi k^2 |\mathbf{r} - \mathbf{r}'|} = \begin{bmatrix} G_{xx} & G_{xy} & G_{xz} \\ G_{xy} & G_{yy} & G_{yz} \\ G_{xz} & G_{yz} & G_{zz} \end{bmatrix} . \quad (2)$$

From this expression, we notice that the DFG is a symmetric tensor, such that

$$\vec{\vec{\mathbf{G}}}(\mathbf{r}, \mathbf{r}') = \left[ \vec{\vec{\mathbf{G}}}(\mathbf{r}, \mathbf{r}') \right]^T .$$

---

<sup>3</sup>The identity  $\nabla \cdot (G_0 \vec{\vec{\mathbf{I}}}) = \nabla G_0$  was applied.

<sup>4</sup>We have adopted Cartesian coordinates so that  $\nabla = \left( \frac{\partial}{\partial x} \hat{x} + \frac{\partial}{\partial y} \hat{y} + \frac{\partial}{\partial z} \hat{z} \right)$ .

Explicit calculus for the outgoing wave gives

$$\vec{\vec{\mathbf{G}}}(\mathbf{r}, \mathbf{r}') = \frac{e^{ikR}}{4\pi R} \left[ \left( 1 + \frac{ikR - 1}{k^2 R^2} \right) \vec{\vec{\mathbf{I}}} + \frac{3 - 3ikR - k^2 R^2}{k^2 R^2} \frac{\mathbf{R}\mathbf{R}}{R^2} \right] .$$

where  $R = |\mathbf{r} - \mathbf{r}'|$  and  $\mathbf{R}\mathbf{R}$  is the outer product of  $\mathbf{R}$  with itself.

By noting that this last expression depends on the terms  $(kR)^{-1}$ ,  $(kR)^{-2}$ ,  $(kR)^{-3}$ , it is possible to split the dyadic Green's function into three parts, each corresponding to a different term:

$$\vec{\vec{\mathbf{G}}} = \vec{\vec{\mathbf{G}}}_{NF} + \vec{\vec{\mathbf{G}}}_{IF} + \vec{\vec{\mathbf{G}}}_{FF} .$$

In the *far-field*, for which  $R \gg \lambda$ , only the terms with  $(kR)^{-1}$  survive; in a similar manner, the terms  $(kR)^{-3}$  are the dominant ones in the *near-field* approximation ( $R \ll \lambda$ ), and the  $(kR)^{-2}$  characterize the *intermediate-field* region at  $R \approx \lambda$ .

The single contributes can be written as

$$\begin{aligned} \vec{\vec{\mathbf{G}}}_{NF} &= \frac{1}{k^2 R^2} \left[ -\vec{\vec{\mathbf{I}}} + 3\mathbf{R}\mathbf{R}/R^2 \right] \frac{e^{ikR}}{4\pi R} \\ \vec{\vec{\mathbf{G}}}_{IF} &= \frac{i}{kR} \left[ \vec{\vec{\mathbf{I}}} - 3\mathbf{R}\mathbf{R}/R^2 \right] \frac{e^{ikR}}{4\pi R} \\ \vec{\vec{\mathbf{G}}}_{FF} &= \left[ \vec{\vec{\mathbf{I}}} - \mathbf{R}\mathbf{R}/R^2 \right] \frac{e^{ikR}}{4\pi R} . \end{aligned}$$

## Electric dipole fields in a homogeneous space

The current density associated to a time-harmonic oscillating dipole, with origin at the center of the charge distribution  $\mathbf{r}_0$ , has the form

$$\mathbf{j}(\mathbf{r}) = -i\omega \mathbf{p} \delta(\mathbf{r} - \mathbf{r}_0) ,$$

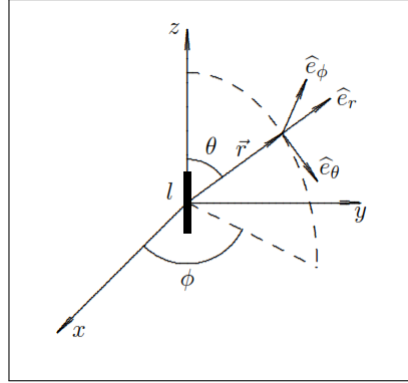
where  $\mathbf{p} = q \, d\mathbf{s}$  is the dipole moment given by the charge  $q$  oscillating respect to the infinitesimal vector  $d\mathbf{s}$  in a homogeneous, linear and isotropic space. By substituting this expression into the volume integral equations, we can write the fields originating from the dipole as

$$\mathbf{E}(\mathbf{r}) = \omega^2 \mu_0 \mu \vec{\vec{\mathbf{G}}}(\mathbf{r}, \mathbf{r}_0) \mathbf{p}$$

$$\mathbf{H}(\mathbf{r}) = -i\omega \left[ \nabla \times \vec{\vec{\mathbf{G}}}(\mathbf{r}, \mathbf{r}_0) \right] \mathbf{p} .$$

## B) Hertzian Dipole

The Hertzian dipole antenna configuration is given by a linear wire of infinitesimal length ( $l \ll \lambda$ ) positioned symmetrically at the origin of the coordinate system and oriented along the vertical axis  $z$ .



*Hertzian dipole.*

The wire must also be very thin ( $a \ll \lambda$ ), so that the spatial variation of the current is assumed to be constant. Dipole current is given by

$$\mathbf{I}(z') = \hat{\mathbf{a}}_z I_0 ,$$

where  $I_0$  is a constant value.

### Infinitesimal dipole radiation fields

By applying the integral equation of the vector potential  $\mathbf{A}$

$$\mathbf{A}(\mathbf{r}) = \mu_0 \mu \int_V \mathbf{j}(\mathbf{r}') G_0(\mathbf{r}, \mathbf{r}') dV' = \frac{\mu_0 \mu}{4\pi} \int_V \mathbf{j}(\mathbf{r}') \frac{e^{\pm ik|\mathbf{r}-\mathbf{r}'|}}{|\mathbf{r}-\mathbf{r}'|} dV'$$

to the infinitesimal line-source, we can express the radiated field as it's given from a linear superposition of point-sources

$$\mathbf{A}(\mathbf{r}) = \frac{\mu_0 \mu}{4\pi} \int_C \mathbf{I}_e(\mathbf{r}') \frac{e^{\pm ik|\mathbf{r}-\mathbf{r}'|}}{|\mathbf{r}-\mathbf{r}'|} dl' ,$$

so that the volume integral reduces to a line integral on a curve.

Now, for the definition of Hertzian dipole, we know that the electric current  $\mathbf{I}_e$  has the form

$$\mathbf{I}_e(\mathbf{r}') = \mathbf{I}_e(z') = \hat{\mathbf{a}}_z I_0 ,$$

and

$$|\mathbf{r}'| = r' = 0 \iff x' = y' = z' = 0 ,$$

thus gives

$$|\mathbf{r} - \mathbf{r}'| = \sqrt{(x - x')^2 + (y - y')^2 + (z - z')^2} = \sqrt{x^2 + y^2 + z^2} = r ,$$

so that the integral equation reduces to the form

$$\mathbf{A}(\mathbf{r}) = \hat{\mathbf{a}}_z \frac{\mu_0 \mu I_0}{4\pi r} e^{\pm ikr} \int_{-l/2}^{l/2} dz' = \hat{\mathbf{a}}_z \frac{\mu_0 \mu I_0 l}{4\pi r} e^{\pm ikr} .$$

We may now express the field components in spherical components by applying the matrix transformations

$$\begin{bmatrix} A_r \\ A_\theta \\ A_\phi \end{bmatrix} = \begin{bmatrix} \sin \theta \cos \phi & \sin \theta \sin \phi & \cos \theta \\ \cos \theta \cos \phi & \cos \theta \sin \phi & -\sin \theta \\ -\sin \phi & \cos \phi & 0 \end{bmatrix} \begin{bmatrix} A_x \\ A_y \\ A_z \end{bmatrix} ,$$

and, since for this problem  $A_x = A_y = 0$ , the system reduces to

$$\begin{cases} A_r = A_z \cos \theta = \frac{\mu_0 \mu I_0 e^{\pm ikr}}{4\pi r} \cos \theta \\ A_\theta = -A_z \sin \theta = -\frac{\mu_0 \mu I_0 e^{\pm ikr}}{4\pi r} \sin \theta \\ A_\phi = 0 . \end{cases}$$

By applying the Lorenz gauge condition on the vector and scalar potential equations, we can derive the expressions for the fields  $\mathbf{E}$ ,  $\mathbf{H}$ :

$$\begin{aligned} \mathbf{H}(\mathbf{r}) &= \frac{1}{\mu_0 \mu} \nabla \times \mathbf{A}(\mathbf{r}) \\ \mathbf{E}(\mathbf{r}) &= -\nabla \phi(\mathbf{r}) - i\omega \mathbf{A}(\mathbf{r}) \\ &= -i\omega \mathbf{A}(\mathbf{r}) - i \frac{1}{\omega \mu_0 \mu \varepsilon_0 \varepsilon} \nabla (\nabla \cdot \mathbf{A}(\mathbf{r})) \\ &= \frac{1}{i\omega \varepsilon_0 \varepsilon} \nabla \times \mathbf{H}(\mathbf{r}) . \end{aligned}$$

Finally, the expansion in spherical coordinates for  $\mathbf{H}^5$ ,

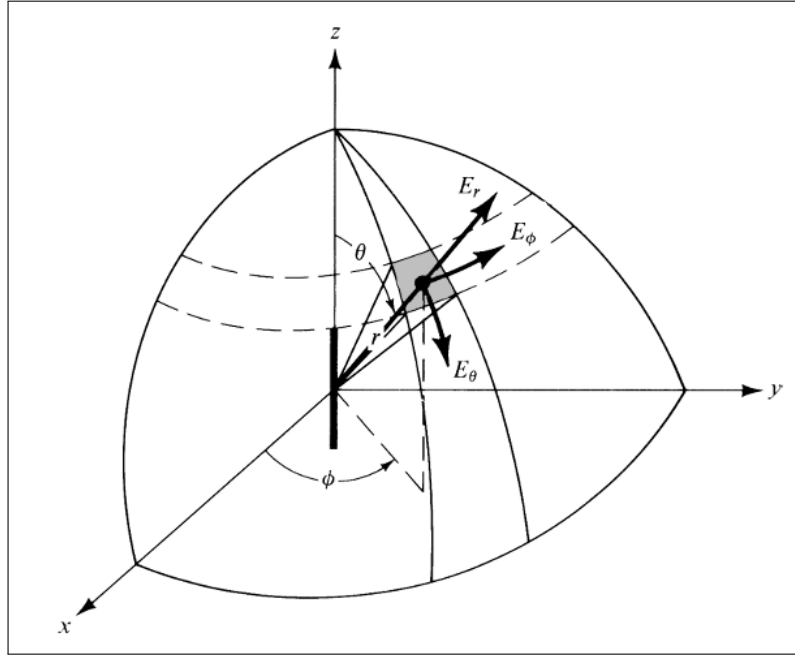
$$\mathbf{H} = \hat{\mathbf{a}}_\phi \frac{1}{\mu_0 \mu r} \left[ \frac{\partial}{\partial r} (r A_\theta) - \frac{\partial A_r}{\partial \theta} \right] ,$$

---

<sup>5</sup>The symmetry of the problem with respect to  $\phi$  was exploited.

gives us the desired field components:

$$\begin{cases} H_\phi = i \frac{k I_0 l \sin \theta}{4\pi r} \left[ 1 + \frac{1}{ikr} \right] e^{\pm ikr} \\ H_r = H_\theta = 0 \\ E_r = \eta \frac{I_0 l \cos \theta}{2\pi r^2} \left[ 1 + \frac{1}{ikr} \right] e^{\pm ikr} \\ E_\theta = i\eta \frac{k I_0 l \sin \theta}{4\pi r} \left[ 1 + \frac{1}{ikr} - \frac{1}{(kr)^2} \right] e^{\pm ikr} \\ E_\phi = 0 . \end{cases}$$



*Electric field components in spherical coordinates.*

The  $\mathbf{E}$ ,  $\mathbf{H}$  fields components we just derived are valid everywhere, except on the source itself.

The total electric field is given by

$$\mathbf{E} = \hat{\mathbf{a}}_r E_r + \hat{\mathbf{a}}_\theta E_\theta ,$$

whose corresponding magnitude is

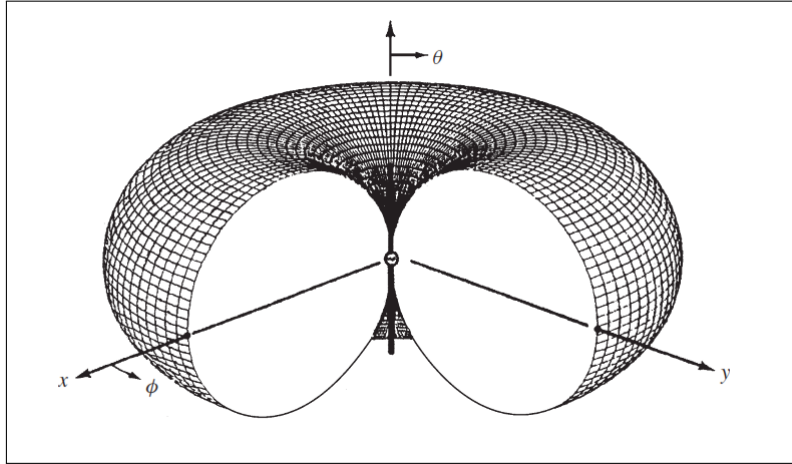
$$|\mathbf{E}| = \sqrt{|E_r|^2 + |E_\theta|^2} .$$

## Field components approximations

The expressions we have derived for the spherical components of the fields can be rearranged into a compact, analytical form:

$$\begin{aligned}
 \mathbf{H} &= \frac{kI_0 l e^{\pm ikr}}{4\pi r} \left( i + \frac{1}{kr} \right) \sin \theta \, \hat{\phi} \\
 \mathbf{E} &= -\frac{i\eta I_0 l e^{\pm ikr}}{2\pi k} \left( \frac{ik}{r^2} + \frac{1}{r^3} \right) \cos \theta \, \hat{\mathbf{r}} - \frac{i\eta I_0 l e^{\pm ikr}}{4\pi k} \left( -\frac{k^2}{r} + \frac{ik}{r^2} + \frac{1}{r^3} \right) \sin \theta \, \hat{\boldsymbol{\theta}} = \\
 &= k\eta I_0 l \left[ 2 \left( \frac{1}{kr} - \frac{i}{(kr)^2} \right) \cos \theta \, \hat{\mathbf{r}} + \left( i + \frac{1}{kr} - \frac{i}{(kr)^2} \right) \sin \theta \, \hat{\boldsymbol{\theta}} \right] \frac{e^{\pm ikr}}{4\pi r} = \\
 &= k\eta I_0 l \left[ 2 \left( \frac{1}{kr} - \frac{i}{(kr)^2} \right) \cos \theta \, \hat{\mathbf{r}} + \left( i + \frac{1}{kr} - \frac{i}{(kr)^2} \right) \sin \theta \, \hat{\boldsymbol{\theta}} \right] G_0(\mathbf{r}) , \quad (3)
 \end{aligned}$$

where  $\eta = \sqrt{\frac{\mu_0 \mu}{\epsilon_0 \epsilon}}$  is the wave impedance. It's customary to define the  $(1/r^2)$  and the  $(1/r^3)$  field terms as *inductive terms* and  $(1/r)$  field terms as *radiative terms*.



*Hertzian dipole radiation pattern.*

The induction fields decay very rapidly with antenna distance  $r$  and provide energy that is stored near the antenna; radiation fields, by decaying less rapidly, propagate farther away thus providing energy propagation away from the antenna position.

We can rewrite the field components in a simplified form for the near-field ( $kr \ll 1$ ), intermediate-field ( $kr > 1$ ) and far-field ( $kr \gg 1$ ) regions.

Near-field approximation:

$$\left. \begin{aligned} E_r &\simeq -i\eta \frac{I_0 l e^{\pm ikr}}{2\pi k r^3} \cos \theta \\ E_\theta &\simeq -i\eta \frac{I_0 l e^{\pm ikr}}{4\pi k r^3} \sin \theta \\ H_\phi &\simeq \frac{I_0 l e^{\pm ikr}}{4\pi r^2} \sin \theta \\ E_\phi = H_r = H_\theta &= 0 \end{aligned} \right\} \quad (kr \ll 1)$$

Intermediate-field approximation:

$$\left. \begin{aligned} E_r &\simeq \eta \frac{I_0 l e^{\pm ikr}}{2\pi r^2} \cos \theta \\ E_\theta &\simeq i\eta \frac{k I_0 l e^{\pm ikr}}{4\pi r} \sin \theta \\ H_\phi &\simeq i \frac{k I_0 l e^{\pm ikr}}{4\pi r} \sin \theta \\ E_\phi = H_r = H_\theta &= 0 \end{aligned} \right\} \quad (kr > 1)$$

Far-field approximation:

$$\left. \begin{aligned} E_\theta &\simeq i\eta \frac{k I_0 l e^{\pm ikr}}{4\pi r} \sin \theta \\ H_\phi &\simeq i \frac{k I_0 l e^{\pm ikr}}{4\pi r} \sin \theta \\ E_r \simeq E_\phi = H_r = H_\theta &= 0 \end{aligned} \right\} \quad (kr \gg 1)$$

# Bibliography

- [1] Ferlay J, Soerjomataram I, Ervik M, Dikshit R, Eser S, Mathers C, Rebelo M, Parkin DM, Forman D, Bray, F. GLOBOCAN 2012 v1.0, Cancer Incidence and Mortality Worldwide: IARC CancerBase No. 11 [Internet]. Lyon, France: International Agency for Research on Cancer; 2013. Available from: <http://globocan.iarc.fr>, accessed on 2/2/2016.
- [2] K McPherson, C M Steel, J M Dixon, “Breast cancer—epidemiology, risk factors, and genetics.”, *BMJ*. 2000 September 9; 321(7261): 624–628.
- [3] Balazs I Bodai, Phillip Tusó, “Breast Cancer Survivorship: A Comprehensive Review of Long-Term Medical Issues and Lifestyle Recommendations.”, *Perm J*. 2015 Spring; 19(2): 48–79. doi: 10.7812/TPP/14-241.
- [4] Cancer Research UK. Breast cancer survival statistics. 2015.
- [5] Tabár, L. and Dean, P. B. (2010), “A New Era in the Diagnosis and Treatment of Breast Cancer.”, *The Breast Journal*, 16: S2–S4. doi: 10.1111/j.1524-4741.2010.00992.x.
- [6] Samuel K. Moore, “Better Breast Cancer Detection,” *IEEE Spectrum*, May 2011, p. 50–54.
- [7] D. B. Kopans, “Breast Imaging.”, Lippincott Williams & Wilkins, 2007.
- [8] Elmore JG, Armstrong K, Lehman CD, Fletcher SW. “Screening for Breast Cancer.” *JAMA*. 2005;293(10):1245–1256. doi:10.1001/jama.293.10.1245.
- [9] Saslow, Debbie and Hannan, Judy and Osuch, Janet and Alciati, Marianne H. and Baines, Cornelia and Barton, Mary and Bobo, Janet Kay and Coleman, Cathy and Dolan, Mary and Gaumer, Ginny and Kopans, Daniel and Kutner, Susan and Lane, Dorothy S. and Lawson, Herschel and Meissner, Helen and Moorman, Candace and Pennypacker, Henry and Pierce, Peggy and Sciandra, Eva and Smith, Robert and Coates, Ralph, “Clinical Breast Examination: Practical Recommendations for Optimizing Performance and Reporting”, *CA: A Cancer Journal for Clinicians*, Volume 54, Issue 6, pages 327–344, November/December 2004. John Wiley & Sons, Ltd.



- [10] Peter Herzog, Christina T. Rieger, “Risk of cancer from diagnostic X-rays.”, *Lancet*. 2004 January 31; 363(9406): 340–341. doi: 10.1016/S0140-6736(04)15470-6.
- [11] P T Huynh, A M Jarolimek, S Daye, “The false-negative mammogram.”, *Radiographics*, Sep 1998, Vol. 18:1137–1154, 10.1148/radiographics.18.5.9747612.
- [12] Clark DJ, Chambers IR, Faulkner K, Rayson J, Hacking PM, Milton J. , “Pressure measurements during automatic breast compression in mammography.”, *J Biomed Eng*. 1990 Sep;12(5):444-6. PubMed PMID: 2214734.
- [13] Saslow, D., Boetes, C., Burke, W., Harms, S., Leach, M. O., Lehman, C. D., Morris, E., Pisano, E., Schnall, M., Sener, S., Smith, R. A., Warner, E., Yaffe, M., Andrews, K. S., Russell, C. A. and for the American Cancer Society Breast Cancer Advisory Group (2007), “American Cancer Society Guidelines for Breast Screening with MRI as an Adjunct to Mammography.”, *CA: A Cancer Journal for Clinicians*, 57: 75–89. doi: 10.3322/canjclin.57.2.75
- [14] Wendie A. Berg and Lorena Gutierrez and Moriel S. NessAiver and W. Bradford Carter and Mythreyi Bhargavan and Rebecca S. Lewis and Olga B. Ioffe, “Diagnostic Accuracy of Mammography, Clinical Examination, US, and MR Imaging in Preoperative Assessment of Breast Cancer”, *Radiology* 2004 233:3, 830-849.
- [15] Sprague BL, Stout NK, Schechter C, van Ravesteyn NT, Cevik M, Alagoz O, et al. , “Benefits, Harms, and Cost-Effectiveness of Supplemental Ultrasonography Screening for Women With Dense Breasts.”, *Ann Intern Med*. 2015;162:157-166. doi:10.7326/M14-0692.
- [16] Wendie A. Berg, Jeffrey D. Blume, Amanda M. Adams, Roberta A. Jong, Richard G. Barr, Daniel E. Lehrer, Etta D. Pisano, W. Phil Evans, III, Mary C. Mahoney, Linda Hovanessian Larsen, Glenna J. Gabrielli, and Ellen B. Mendelson, “Reasons Women at Elevated Risk of Breast Cancer Refuse Breast MR Imaging Screening: ACRIN 6666”, *Radiology* 2010 254:1, 79-87.
- [17] Fear, E.C.; Meaney, P.M.; Stuchly, M.A., “Microwaves for breast cancer detection?”, in *Potentials*, IEEE , vol.22, no.1, pp.12-18, Feb/Mar 2003 doi: 10.1109/MP.2003.1180933.
- [18] E. Y. K. Ng , W. K. Ng , U. Rajendra Acharya, “Biofield potential simulation as a novel adjunct modality for continuous monitoring of breast lesions: a 3D numerical model”, *Journal of Medical Engineering & Technology*, Vol. 32, Iss. 1, 2008.
- [19] Martins, Mónica Vieira. “Positron Emission Mammography.”, (2015).

- [20] Yun, W. and Wang, Y. , “X-ray mammography”, US Patent 7,412,024. Google Patents.
- [21] Pace LE, Keating NL. “A Systematic Assessment of Benefits and Risks to Guide Breast Cancer Screening Decisions.”, JAMA. 2014;311(13):1327-1335. doi:10.1001/jama.2014.1398.
- [22] “Screening Mammography Benefits and Harms in Spotlight Again.”, Medscape. Apr 02, 2009.
- [23] Canadian Task Force on Preventive Health Care, Tonelli M, Connor Gorber S, Joffres M, Dickinson J, Singh H, Lewin G, Birtwhistle R, Fitzpatrick-Lewis D, Hodgson N, Ciliska D, Gaudl M, Liu YY., “Recommendations on screening for breast cancer in average-risk women aged 40-74 years.”, CMAJ. 2011 Nov 22;183(17):1991-2001. doi: 10.1503/cmaj.110334.
- [24] Gøtzsche PC, Nielsen M (2011). “Screening for breast cancer with mammography”, Cochrane Database Syst Rev (1): CD001877. doi:10.1002/14651858.CD001877.pub4
- [25] Welch H, Frankel BA. “Likelihood That a Woman With Screen-Detected Breast Cancer Has Had Her Life Saved by That Screening.”, Arch Intern Med. 2011;171(22):2043-2046. doi:10.1001/archinternmed.2011.476.
- [26] Joann G. Elmore, M.D., M.P.H., Mary B. Barton, M.D., M.P.P., Victoria M. Mocerri, Ph.C., Sarah Polk, B.A., Philip J. Arena, M.D., and Suzanne W. Fletcher, M.D., “Ten-Year Risk of False Positive Screening Mammograms and Clinical Breast Examinations”, N Engl J Med 1998; 338:1089-1096| April 16, 1998|DOI: 10.1056/NEJM199804163381601.
- [27] Mushlin AI, Kouides RW, Shapiro DE, “Estimating the accuracy of screening mammography: a meta-analysis.”, Am J Prev Med. 1998 ;14(2):143-53.
- [28] Independent UK Panel on Breast Cancer Screening, “The benefits and harms of breast cancer screening: an independent review”, The Lancet, Volume 380, Issue 9855, 17–23 November 2012, Pages 1778-1786, ISSN 0140-6736, [http://dx.doi.org/10.1016/S0140-6736\(12\)61611-0](http://dx.doi.org/10.1016/S0140-6736(12)61611-0).
- [29] Kuusisto, Finn; Dutra, Ines; Nassif, Houssam; Wu, Yirong; Klein, Molly E; Neuman, Heather B; Shavlik, Jude; Burnside, Elizabeth S (2013). “Using Machine Learning to Identify Benign Cases with Non-Definitive Biopsy”, IEEE International Conference on E-Health Networking, Application & Services (HealthCom’13): 283–285.
- [30] Heywang-Kobrunner SH, Bick U, Bradley WG, Jr, et al. , “International investigation of breast MRI: results of a multicentre study (11 sites) concerning diagnostic

- parameters for contrast-enhanced MRI based on 519 histopathologically correlated lesions.”, *Eur Radiol* 2001; 11:531–546.
- [31] Kriege M, Brekelmans CT, Boetes C, et al. “Efficacy of MRI and mammography for breast-cancer screening in women with a familial or genetic predisposition.”, *N Engl J Med* 2004; 351:427–437.
  - [32] Saslow, D., Boetes, C., Burke, W., Harms, S., Leach, M. O., Lehman, C. D., Morris, E., Pisano, E., Schnall, M., Sener, S., Smith, R. A., Warner, E., Yaffe, M., Andrews, K. S., Russell, C. A. and for the American Cancer Society Breast Cancer Advisory Group (2007), “American Cancer Society Guidelines for Breast Screening with MRI as an Adjunct to Mammography.”, *CA: A Cancer Journal for Clinicians*, 57: 75–89. doi: 10.3322/canjclin.57.2.75
  - [33] W Teh, A.R.M Wilson, “The role of ultrasound in breast cancer screening. A consensus statement by the European Group for breast cancer screening”, *European Journal of Cancer*, Volume 34, Issue 4, March 1998, Pages 449-450, ISSN 0959-8049, [http://dx.doi.org/10.1016/S0959-8049\(97\)10066-1](http://dx.doi.org/10.1016/S0959-8049(97)10066-1).
  - [34] Wendie A. Berg, Andriy I. Bandos, Ellen B. Mendelson, Daniel Lehrer, Roberta A. Jong, and Etta D. Pisano, “Ultrasound as the Primary Screening Test for Breast Cancer: Analysis From ACRIN 6666”, *JNCI J Natl Cancer Inst* (2016) 108 (4): djv367 doi:10.1093/jnci/djv367 First published online December 28, 2015 (8 pages).
  - [35] Schwan, H. P. “Electrical properties of tissues and cell suspensions: mechanisms and models.” Engineering in Medicine and Biology Society, 1994. Engineering Advances: New Opportunities for Biomedical Engineers. Proceedings of the 16th Annual International Conference of the IEEE. IEEE, 1994.
  - [36] A. De Lorenzo, A. Andreoli, J. Matthie, P. Withers, “Predicting body cell mass with bioimpedance by using theoretical methods: a technological review”, *Journal of Applied Physiology* May 1997, 82 (5) 1542-1558.
  - [37] Kuang, W., and S. O. Nelson. “LOW-FREQUENCY DIELECTRIC PROPERTIES OF BIOLOGICAL TISSUES: A REVIEW WITH SOME NEW INSIGHTS.” *Transactions of the ASAE* 41.1 (1998): 173.
  - [38] Gabriel, Camelia. *Compilation of the Dielectric Properties of Body Tissues at RF and Microwave Frequencies*. KING’S COLL LONDON (UNITED KINGDOM) DEPT OF PHYSICS, 1996.
  - [39] Gabriel C, Gabriel S, Corthout E, “The dielectric properties of biological tissues: I. Literature survey.”, *Phys Med Biol*. 1996 Nov;41(11):2231-49.

- [40] Gabriel, S., R. W. Lau, and Camelia Gabriel. "The dielectric properties of biological tissues: II. Measurements in the frequency range 10 Hz to 20 GHz." *Physics in medicine and biology* 41.11 (1996): 2251.
- [41] Gabriel, Sami, R. W. Lau, and Camelia Gabriel. "The dielectric properties of biological tissues: III. Parametric models for the dielectric spectrum of tissues." *Physics in medicine and biology* 41.11 (1996): 2271.
- [42] Surowiec, Andrzej J., et al. "Dielectric properties of breast carcinoma and the surrounding tissues." *Biomedical Engineering, IEEE Transactions on* 35.4 (1988): 257-263.
- [43] Gabriel, Camelia, "Dielectric properties of biological tissue: Variation with age", *Bioelectromagnetics* Volume 26, Issue S7, pages S12–S18, 2005.
- [44] Li, Xu, and Susan C. Hagness. "A confocal microwave imaging algorithm for breast cancer detection." *Microwave and Wireless Components Letters, IEEE* 11.3 (2001): 130-132.
- [45] Fear, E.C.; Li, Xu; Hagness, S.C.; Stuchly, M.A., "Confocal microwave imaging for breast cancer detection: localization of tumors in three dimensions," in *Biomedical Engineering, IEEE Transactions on* , vol.49, no.8, pp.812-822, Aug. 2002, doi: 10.1109/TBME.2002.800759
- [46] Hurt, W.D., "Multiterm Debye Dispersion Relations for Permittivity of Muscle," in *Biomedical Engineering, IEEE Transactions on* , vol.BME-32, no.1, pp.60-64, Jan. 1985, doi: 10.1109/TBME.1985.325629
- [47] Lazebnik, Mariya, et al. "A large-scale study of the ultrawideband microwave dielectric properties of normal breast tissue obtained from reduction surgeries." *Physics in medicine and biology* 52.10 (2007): 2637.
- [48] Lazebnik, Mariya, et al. "A large-scale study of the ultrawideband microwave dielectric properties of normal, benign and malignant breast tissues obtained from cancer surgeries." *Physics in Medicine and Biology* 52.20 (2007): 6093.
- [49] Devaney, Anthony J. "Super-resolution Processing of Multi-static Data Using Time Reversal and MUSIC." (2000).
- [50] Engl, Heinz Werner, Martin Hanke, and Andreas Neubauer. *Regularization of inverse problems*. Vol. 375. Springer Science & Business Media, 1996.
- [51] Meaney, Paul M. and Demidenko, Eugene and Yagnamurthy, Navin K. and Li, Dun and Fanning, Margaret W. and Paulsen, Keith D. , "A two-stage microwave

- image reconstruction procedure for improved internal feature extraction.” , *Medical Physics*, 28, 2358-2369 (2001), DOI:<http://dx.doi.org/10.1118/1.1413520>
- [52] Li, Dun; Meaney, P.M.; Paulsen, K.D., “Conformal microwave imaging for breast cancer detection,” in *Microwave Theory and Techniques, IEEE Transactions on* , vol.51, no.4, pp.1179-1186, Apr 2003 doi: 10.1109/TMTT.2003.809624
  - [53] Bozza, G.; Pastorino, M., “An Inexact Newton-Based Approach to Microwave Imaging Within the Contrast Source Formulation,” in *Antennas and Propagation, IEEE Transactions on* , vol.57, no.4, pp.1122-1132, April 2009
  - [54] Giacomo Oliveri, Andrea Randazzo, Matteo Pastorino, and Andrea Massa, “Electromagnetic inversion with the multiscaling inexact Newton method—experimental validation”, *Microwave and Optical Technology Letters* Volume 53, Issue 12, pages 2834–2838, December 2011
  - [55] Giacomo Oliveri, Andrea Randazzo, Matteo Pastorino, and Andrea Massa, “Electromagnetic imaging within the contrast-source formulation by means of the multiscaling inexact Newton method,” *J. Opt. Soc. Am. A* 29, 945-958 (2012)
  - [56] Estatico, Claudio, Matteo Pastorino, and Andrea Randazzo. “Microwave imaging of three-dimensional targets by means of an inexact-Newton-based inversion algorithm.” *International Journal of Antennas and Propagation* 2013 (2013).
  - [57] Winters, D.W.; Shea, J.D.; Kosmas, P.; Van Veen, B.D.; Hagness, S.C., “Three-Dimensional Microwave Breast Imaging: Dispersive Dielectric Properties Estimation Using Patient-Specific Basis Functions,” in *Medical Imaging, IEEE Transactions on* , vol.28, no.7, pp.969-981, July 2009 doi: 10.1109/TMI.2008.2008959
  - [58] Shea, Jacob D., et al. “Three-dimensional microwave imaging of realistic numerical breast phantoms via a multiple-frequency inverse scattering technique.” *Medical physics* 37.8 (2010): 4210-4226.
  - [59] Khalil, Muhammad Hassan, and Xu Jiadong. “Inverse scattering in microwave imaging for detection of malignant tumor inside the human body.” *way* 7.1 (2014).
  - [60] Rubæk, Tonny, et al. “Nonlinear microwave imaging for breast-cancer screening using Gauss–Newton’s method and the CGLS inversion algorithm.” *IEEE Transactions on Antennas and Propagation* 55.8 (2007): 2320-2331.
  - [61] Caorsi, P.; Gragnani, G.L.; Medicina, S.; Pastorino, M.; Zunino, G., “Microwave imaging based on a Markov random field model,” in *Antennas and Propagation, IEEE Transactions on* , vol.42, no.3, pp.293-303, Mar 1994 doi: 10.1109/8.280714

- [62] Klemm, M., et al. "Improved delay-and-sum beamforming algorithm for breast cancer detection." *International Journal of Antennas and Propagation* 2008 (2008).
- [63] M. O'Halloran, M. Glavin, and E. Jones, "Effects of fibroglandular tissue distribution on data-independent beamforming algorithms," *Progress In Electromagnetics Research*, Vol. 97, 141-158, 2009. doi:10.2528/PIER09081701
- [64] Bond, Essex J.; Li, Xu; Hagness, S.C.; Van Veen, B.D., "Microwave imaging via space-time beamforming for early detection of breast cancer," in *Antennas and Propagation, IEEE Transactions on* , vol.51, no.8, pp.1690-1705, Aug. 2003 doi: 10.1109/TAP.2003.815446
- [65] Amineh, Reza K., et al. "Three-dimensional near-field microwave holography using reflected and transmitted signals." *Antennas and Propagation, IEEE Transactions on* 59.12 (2011): 4777-4789.
- [66] Amineh, Reza K., et al. "Three-dimensional near-field microwave holography for tissue imaging." *Journal of Biomedical Imaging* 2012 (2012): 5.
- [67] Kosmas, Panagiotis, and Carey M. Rappaport. "Time reversal with the FDTD method for microwave breast cancer detection." *Microwave Theory and Techniques, IEEE Transactions on* 53.7 (2005): 2317-2323.
- [68] Yavuz, M.E.; Teixeira, F.L., "Ultrawideband Microwave Sensing and Imaging Using Time-Reversal Techniques: A Review.", *Remote Sens.* 2009, 1, 466-495.
- [69] Hossain, M.D.; Mohan, A.S.; Abedin, M.J., "Beamspace Time-Reversal Microwave Imaging for Breast Cancer Detection," in *Antennas and Wireless Propagation Letters, IEEE* , vol.12, no., pp.241-244, 2013 doi: 10.1109/LAWP.2013.2247018
- [70] Solimene, Raffaele, et al. "Detecting point-like sources of unknown frequency spectra." *Progress In Electromagnetics Research B* 50 (2013): 347-364.
- [71] Grandi, Massimiliano, et al. "Breast microwave imaging with monostatic and multistatic approaches: Numerical simulations with MUSIC reconstruction." *Electromagnetics in Advanced Applications (ICEAA), 2015 International Conference on.* IEEE, 2015.
- [72] Moura, José MF, and Yuanwei Jin. "Time reversal imaging by adaptive interference canceling." *Signal Processing, IEEE Transactions on* 56.1 (2008): 233-247.
- [73] Elahi, Muhammad Adnan, et al. "Artifact removal algorithms for microwave imaging of the breast." *Progress In Electromagnetics Research* 141 (2013): 185-200.

- [74] Maklad, B., et al. "Neighborhood-based algorithm to facilitate the reduction of skin reflections in radar-based microwave imaging." *Progress In Electromagnetics Research B* 39 (2012): 115-139.
- [75] Lazaro, Antonio, David Girbau, and Ramon Villarino. "Simulated and experimental investigation of microwave imaging using UWB." *Progress In Electromagnetics Research* 94 (2009): 263-280.
- [76] Winters, David W., et al. "Estimation of the frequency-dependent average dielectric properties of breast tissue using a time-domain inverse scattering technique." *Antennas and Propagation, IEEE Transactions on* 54.11 (2006): 3517-3528.
- [77] E. Zastrow, S.K. Davis, M. Lazebnik, F. Kelcz, B.D. Van Veen, and S.C. Hagness. "Database of 3D Grid-Based Numerical Breast Phantoms for use in Computational Electromagnetics Simulations" (2007).
- [78] G. Ruvio, R. Solimene, A. D'Alterio, M. J. Ammann, and R. Pierri, "RF Breast Cancer Detection Employing a Non-characterized Vivaldi Antenna and a MUSIC-like Algorithm", *International Journal of RF and Microwave Computed-Aided Engineering*, vol. 23, issue 5, pp. 598-609, 09/2013.doi: 10.1002/mmce.20694
- [79] Pareo, Francesco (2015), "Performance analysis of reconstruction algorithms for breast microwave imaging".
- [80] Nanetti F., "Experimental Setup and Characterization of a Prototype for Breast Microwave Imaging".
- [81] M. Pastorino, "Microwave Imaging", John Wiley & Sons.
- [82] S. Barbarino, "Appunti di Campi elettromagnetici", Cap. 11.
- [83] Constantine A. Balanis, "Modern Antenna Handbook", John Wiley & Sons.
- [84] Constantine A. Balanis, "Antenna Theory: Analysis And Design", John Wiley & Sons.
- [85] J.A.Kong, "Electromagnetic Wave Theory", John Wiley & Sons.
- [86] L. Novotny, "Physical Optics II - Electrodynamic Field Theory", Class Notes 02, 04, 09. Nanophotonics Laboratory, Department of Information Technology and Electrical Engineering, ETH Zurich.
- [87] S. J. Orfanidis, "Electromagnetic Waves and Antennas".